高エネルギー粒子線照射下でのオーステナイト系ステンレス鋼の損傷組織と強度の相関に関する研究

Microstructure-Strength Correlation in Austenitic Stainless Steels under High Energy Particle Irradiation

Hiroshi Oka†

Division of Materials Science and Engineering, Graduate School of Engineering ‡ ,
Hokkaido University, Japan

February, 2014

† e-mail: hiroshi_oka@eng.hokudai.ac.jp
‡ N-13, W-8, Kita-ku, Sapporo 0608628, Japan

Microstructure-Strength Correlation in Austenitic Stainless Steels under High Energy Particle Irradiation

Hiroshi Oka

Division of Materials Science and Engineering, Graduate School of Engineering, Hokkaido University, Japan

CONTENTS

Chapter 1

Introduction

1.1. Requirement of new generation energy system

In recent years, a spreading awareness of global warming attributed to the emission of greenhouse effect gas has prompted developed countries to rapidly step up environmental preservation efforts. Above all, due to the prevailing point of view where an investment in environmental technologies contributes to the economic boost after the global economic crisis in 2008, the environmental technology would develop much further.

The huge earthquake and the massive tsunami attacking to Tohoku area in March 2011 had cause the severe nuclear disaster at Fukushima Daiichi nuclear power plant. The disaster brought about controversies over the safety of nuclear power plants and led to prolonged shutdown of all nuclear power plants in Japan. While the expectations for renewable energy like solar- and wind-generated power is growing, increasing costs of fossil fuel to compensate for the stop of nuclear power generation is Japan-wide issue. Supply of renewable energies depends strongly on weather conditions in current technology, and also that is not able to cover the whole amounts of energy demand.

These circumstances bring up challenges of reducing reliance on fossil fuels and needs for stable and large sources on worldwide. Such needs motivate the exploration of the quest for advanced fission energy and fusion power. The economics, safety, reliability, and efficiency of both advanced fission and future fusion energy systems will ultimately depend on developing new high-performance structural materials that can provide extended service under extremely hostile conditions [1][2][3].

1.2. Issues of material design for advanced energy systems

Material property change due to irradiation in the structural materials of advanced energy systems such as fusion reactors would exceed the range of the existing data base [3][4] because such materials are used in severe, high dose irradiation environment. Notably 14MeV neutron bombardment is a remarkable environment for fusion reactor materials. Therefore the evaluation of the material behavior at high doses or under 14MeV neutron irradiation is absolutely required [5][6]. However, it is distant to achieve a high dose irradiation condition in practical irradiation experiments because it requires enormous amount of labor and experimental time. Besides, the experimental environment providing 14MeV neutron irradiation is currently not exist in the world.

1.2.1. Traditional approach

To address this situation, prediction methods of materials behavior which are the combinations of; the simulated irradiation [7]; the heterogeneous irradiation field; the numerical calculation model [8]; have been taken. Phenomenon that occurs under irradiation in the material is a multi-scale phenomenon in energy, time, and space. Thus it has been attempted to understand the nature of the problem with the aid of experimental techniques and theoretical analysis method complementary [9], and to predict the material behavior with high accuracy under irradiation.

1.2.2. Multi–scale structure of the phenomena that occur during irradiation

Fig. 1 shows the multi–scale structure of the phenomena under irradiation. The horizontal axis in Fig. 1 is space scale and time scale. Under irradiation, first atomic displacement occur by the bombardment of incident particle. For some situations, it is usually associated with the production of displacement cascade and/or transmutation gas atoms. This phase is undetectable by any experimental method because it is atomic scale phenomena and its time range is picosecond revel. The numerical calculation method

would be strong and only way here. Following that, the produced point defects diffuse in the system and some of them recombine each other or disappear at the grain boundary and dislocation. But some percentages of point defects survive as defect clusters in the matrix. These defect clusters continue to grow due to the absorption of an individual point defect and/or the mutual combination of defect clusters under irradiation, and eventually they become black dot, dislocation loop, cavity, and void. Occasionally the segregation of constituent elements of the system occur, so called radiation induced segregation (RIS). Phenomenon in this phase occur on a time scale of seconds to minutes–hours, and it is detectable in experimental method such as transmission electron microscopy (TEM), atom probe tomography (APT), and positron annihilation spectroscopy (PAS). These defect clusters lead to material property change such as irradiation hardening, irradiation embrittlement, swelling, and irradiation-assisted stress corrosion cracking (IASCC). Now these property changes have days–years time scale. In engineering aspect, these property changes are the most critical issue.

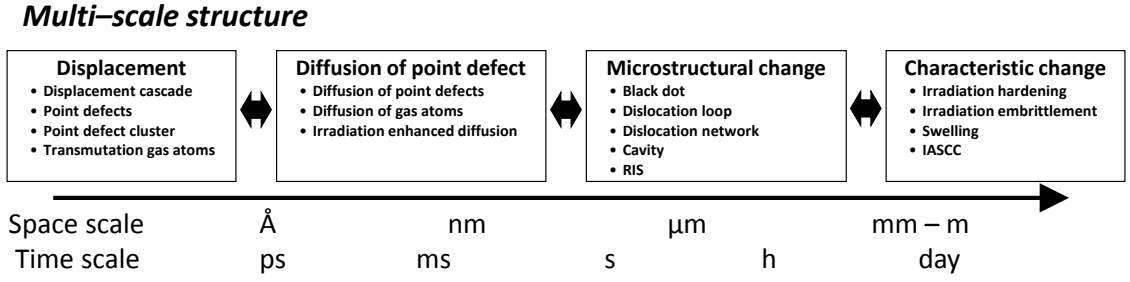

Fig. 1 Multi–scale structure of the phenomena that occur during irradiation.

1.3. Objective of this study

In previous studies, the understandings of individual phenomenon and corresponding analytical method are developed, however, the comprehensive approach that is able to connect individual method, e.g. connecting the technique and another method by an equation, etc., have been undeveloped [10] [11]. In other words, with respect to the irradiation behavior which have a wide range of temporal and spatial scale, understandings of each individual technique within its own scale have only been made in the current situation.

In this study, the correlations between each individual phenomenon are revealed to be able to predict the material properties under irradiation. Several experimental method which have different space scale is taken particular note.

1.4. Philosophy of this study

1.4.1. Spurious correlation in the past study

In the past study, sometimes the change of material property have been summarized in the dependence of irradiation dose. The example is shown in Fig. 2 [12]. The dose dependence of irradiation hardening is described as [13] [14]

$$\Delta\sigma_y = \Delta\sigma_{ys}\,[1 - \exp(-dpa/dpa_0)]^p + \Delta\sigma_0 \qquad (1)$$

where $\Delta\sigma_{ys}$ is a saturation hardening, dpa_0 specifies the dose transient prior to saturation, p is an effective dispersed-barrier hardening exponent, and $\Delta\sigma_0$ is the constant hardening increment. Or another equation [15] [16] [17] which is also describe the dose dependence of irradiation hardening as

$$\Delta\sigma_y = A\,[1 - \exp(-B\times dpa)]^{0.5} \qquad (2).$$

These equations have suggested that the change in yield strength under irradiation is a function of irradiation dose. But this correlation does not describe the essence of issue under irradiation. Because it is clear that the mechanical property changes under irradiation are affected by not only irradiation dose but also irradiation temperature and neutron spectra.

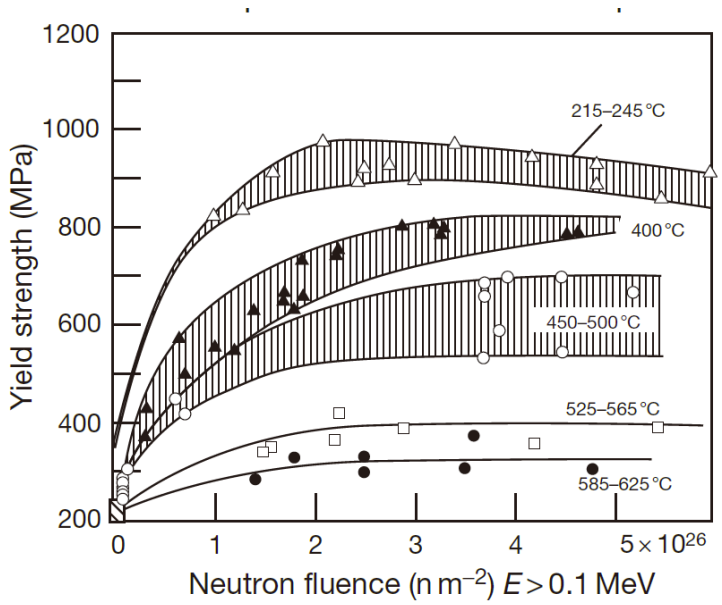

Fig. 2 Neutron-induced changes in tensile properties of annealed 1.4988 stainless steel irradiated in the DFR fast reactor. Reproduced from Ehrlich, K. J. Nucl. Mater. 1985, 133–134, 119–126 [12].

Fig. 3 shows the philosophy toward the behavior under irradiation in this study. As shown in Fig. 3, microstructural evolution under irradiation is a function of dose. But the dose dependency in microstructural evolution should separate from the evolution of mechanical property under irradiation. The mechanical property changes should directly correlate with the “resultant microstructure”, but not with the “history” of microstructural evolution. The attempt to correlate the mechanical property changes to irradiation dose results in a spurious correlation. This study attempt to correlate the mechanical property changes and the resultant microstructure thorough the “mechanism-based correlation”.

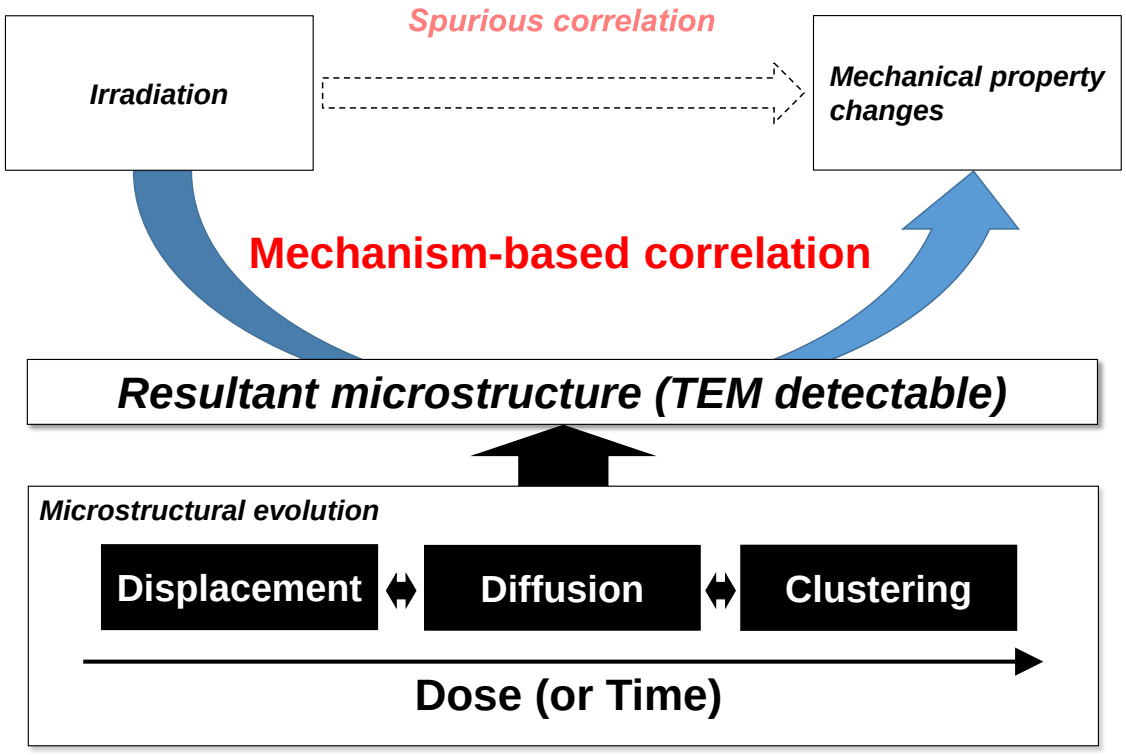

Fig. 3 Attitude toward the behavior under irradiation in this study.

1.4.2. Correlation in this study

- ***Microstructure–mechanical properties correlations:***

Yield stress σ_y (or $\sigma_{0.2}$) is a basic parameter used in engineering assessment. Proper determination of σ_y is an important task for design of fission or fusion reactors. Basically σ_y is determined in the interaction between moving dislocation and obstacles during deformation. To connect microstructure and mechanical properties under irradiation, following equation is usually used in the past studies [18] [19] [20] [21],

$$\Delta\sigma_y = M\alpha\mu b(Nd)^{1/2} \quad (3)$$

where M, α, μ, b, N, and d are the Taylor factor, the barrier strength of obstacles, the shear modulus of the matrix, the Burger's vector of moving dislocation, the number density of obstacles, and the diameter of obstacles, respectively.

In the eq. (3), the barrier strength of obstacles, α, is one of the critical parameter to determine yield stress. However, the parameter α is used as an empirical factor without specific theory. Sometimes α is just a function which adjust the difference between experimental strength and microstructurally–evaluated strength.

Each type of obstacles is considered to have their own barrier strength, α. In this study, through the examination of the barrier strength, microstructure–mechanical properties correlation are discussed. The conceivable obstacles, corresponding symbols, and relevant chapters are listed below.

Table 1
Type of obstacles conceivable in the irradiated material.

Obstacle	Symbol	Relevant chapter
Black dots	$\alpha_{\text{black dot}}$	Chapter 4
Dislocation loops	α_{loop}	Chapter 4
Dislocation lines	α_{d}	Chapter 2 and 3
Precipitates	α_{p}	Chapter 2
Voids	α_{v}	Chapter 2
Oxide particles	α_{oxide}	Chapter 5

- ***Property–property correlations (scale bridging):***

It is not always possible to determine σ_{y} on highly irradiated material using uniaxial tensile tests. The difficulties are following;

1. in the case when there are large levels of induced radioactivity;

2. in the case when the material volume is too small to produce a tensile sample.

One approach to overcome such difficulties is to establish property–property correlations using appropriate correlation relations with nano-hardness [22] and Vickers-hardness [23]. If the appropriate correlation is established, sample size could be small to assess its mechanical properties. This leads to reduce radioactivity of the sample so the research work toward designing materials for advanced energy system is expected to be

further accelerated. Notably nano-indentation technique is the only way to evaluate the mechanical properties of the simulated-irradiation sample involving ion-irradiated sample because damaged region in such sample is limited to in its near surface, a few micro meter depth. Thus nano-hardness to Vickers-hardness correlation is also important in this study. Fig. 4 shows the concept of scale bridging in this study.

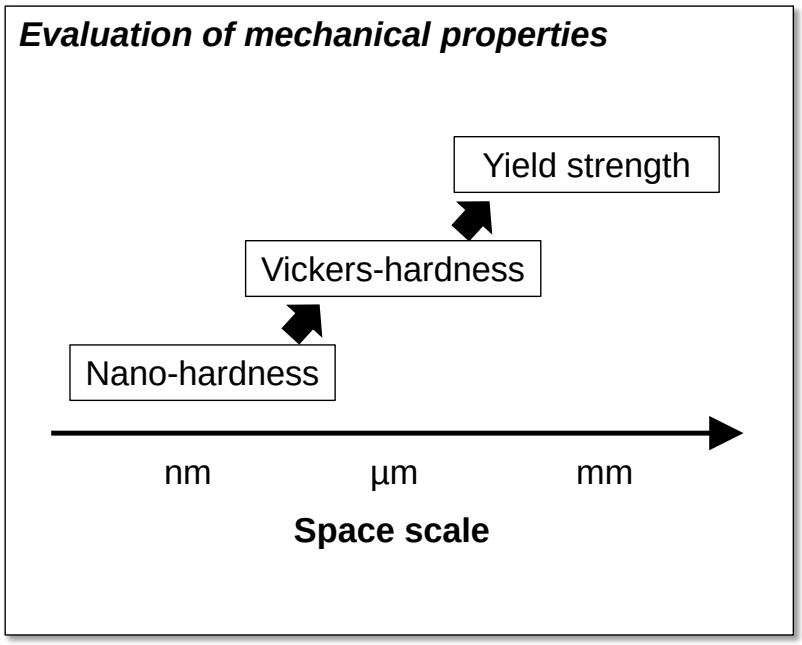

Fig. 4 Concept of scale bridging in this study.

- ***Integrative model:***

Finally, the property changes under particle irradiation is summarizing into the comprehensive model, in chapter 6.

References

[1] G.S. Was, J. Nucl. Mater. 367-370 (2007) 11.

[2] G. Odette, M. Alinger, B. Wirth, Annu. Rev. Mater. Res. 38 (2008) 471.

[3] L.. Mansur, A.. Rowcliffe, R.. Nanstad, S.. Zinkle, W.. Corwin, R.. Stoller, J. Nucl. Mater. 329-333 (2004) 166.

[4] S.J. Zinkle, Fusion Eng. Des. 74 (2005) 31.

[5] T. Muroga, M. Gasparotto, S.. Zinkle, Fusion Eng. Des. 61-62 (2002) 13.

[6] E.E. Bloom, J.T. Busby, C.E. Duty, P.J. Maziasz, T.E. McGreevy, B.E. Nelson, B.A. Pint, P.F. Tortorelli, S.J. Zinkle, J. Nucl. Mater. 367-370 (2007) 1.

[7] I. Kim, J. Hunn, N. Hashimoto, D.. Larson, P.. Maziasz, K. Miyahara, E.. Lee, J. Nucl. Mater. 280 (2000) 264.

[8] H. Abe, N. Sekimura, T. Tadokoro, Mater. Trans. 46 (2005) 433.

[9] A. Sagara, N. Sekimura, H. Hashizume, S. FUKADA, K. Morishita, T. Tanaka, J. Plasma Fusion Res. 85 (2009) 276.

[10] Y. Katoh, R.E. Stoller, Y. Kohno, A. Kohyama, J. Nucl. Mater. 210 (1994) 290.

[11] Y. Katoh, M. Ando, A. Kohyama, J. Nucl. Mater. 323 (2003) 251.

[12] K. Ehrlich, J. Nucl. Mater. 133-134 (1985) 119.

[13] T. Yamamoto, G.R. Odette, H. Kishimoto, J.-W. Rensman, P. Miao, J. Nucl. Mater. 356 (2006) 27.

[14] G.R. Odette, T. Yamamoto, D. Klingensmith, Philos. Mag. 85 (2005) 779.

[15] M.J. Makin, A.D. Whapham, F.J. Minter, Philos. Mag. 7 (1962) 285.

[16] M.J. Makin, F.J. Minter, Acta Metall. 8 (1960) 691.

[17] K. Yabuuchi, H. Yano, R. Kasada, H. Kishimoto, A. Kimura, J. Nucl. Mater. 417 (2011) 988.

[18] G. Lucas, J. Nucl. Mater. 206 (1993) 287.

[19] G.D. Johnson, F.A. Garner, H.R. Brager, R.L. Fish, in:, D. Kramer, H.R. Brager, J.S. Perrin (Eds.), Eff. Radiat. Mater. ASTM STP 725, 1981, pp. 393–412.

[20] G.R. Odette, D. Frey, J. Nucl. Mater. 85-86 (1979) 817.

[21] T. Allen, H. Tsai, J. Cole, J. Ohta, K. Dohi, H. Kusanagi, in:, Eff. Radiat. Mater. ASTM STP 1447, 2004, pp. 3–14.

[22] M. Inamura, T. Suzuki, Seisan-Kenkyu 42 (1990) 257.

[23] J. Cahoon, W. Broughton, A. Kutzak, Metall. Trans. 2 (1971) 1979.

Chapter 2

Radiation-induced hardening and softening

2.1 Introduction

The evolution of mechanical property changes subject to neutron irradiation have been studied for a long time to make it clear under fission and fusion reactor conditions. However limited number of data including a high dose condition and/or simulated fusion reactor condition is available so far [1]. In order to estimate irradiation effects such as irradiation hardening or softening in that kind of condition, an appropriate equation describing relationship between microstructure and mechanical properties in an actual length scale is absolutely required.

Austenitic stainless steels have been used extensively in fission reactor applications, so that the most extensive database for nuclear applications would be based on austenitic stainless steels. In this study, modified-SUS316 austenitic stainless steels irradiated in a fast reactor were investigated. Twelve data sets of irradiated 316 including the microstructures and the mechanical properties were carefully examined.

2.2 Objective of this chapter

1. Investigation of irradiation-induced change in mechanical properties
2. Investigation of irradiation-induced change in microstructure
3. Proposal of an equation describing relationship between microstructure and mechanical properties
4. Discussing an accuracy of the proposed equation

2.3 Experimental

A modified-SUS316 stainless steel (PNC316), which has been developed as a cladding tube material with superior high temperature strength and swelling resistance

for a liquid metal cooled fast reactor [2], was examined in this study. The representative chemical composition of PNC316 is Fe–16Cr–14Ni–0.05C–2.5Mo–0.7Si–0.025P–0.004B–0.lTi–0.lNb. The details of chemical composition used in this study are shown in Table 1. It is, in most cases, used in the 20% cold-worked condition.

The alloys were irradiated in the experimental reactor JOYO using the core material irradiation rig (CMIR). The range of irradiation temperature was 502–734 °C. Fast neutron fluencies were in a range from 3.2 to 20.6 × 10^{26} n/m^2 (E > 0.1 MeV), equivalent to displacement damage in a range from 16.0 to 103 dpa. Note that the irradiation time in this study was from about 3,850 to 18,600 h.

Tensile tests were performed for the irradiated cladding tubes at the irradiation temperature. The procedure of tensile tests was in accordance with JIS (Japanese Industrial Standards) G 0567. The cross head speed was changed during tensile test for some samples. Yield strength, σ_y, was determined as 0.2% offset proof stress. Micro Vickers hardness tests were also carried out with a load of 4.9 N at room temperature. Irradiation-induced microstructure was investigated by using an electron microscope (JEM-4000FX) operated at 400 kV.

2.4 Mechanical properties before and after irradiation

Mechanical properties of PNC316 in the as-received condition are summarized in Table 2, and plotted in Figs. 1. Mechanical properties of PNC316 after irradiation are summarized in Table 3. Stress-strain curves of PNC316 after irradiation are shown in Figs. 2.

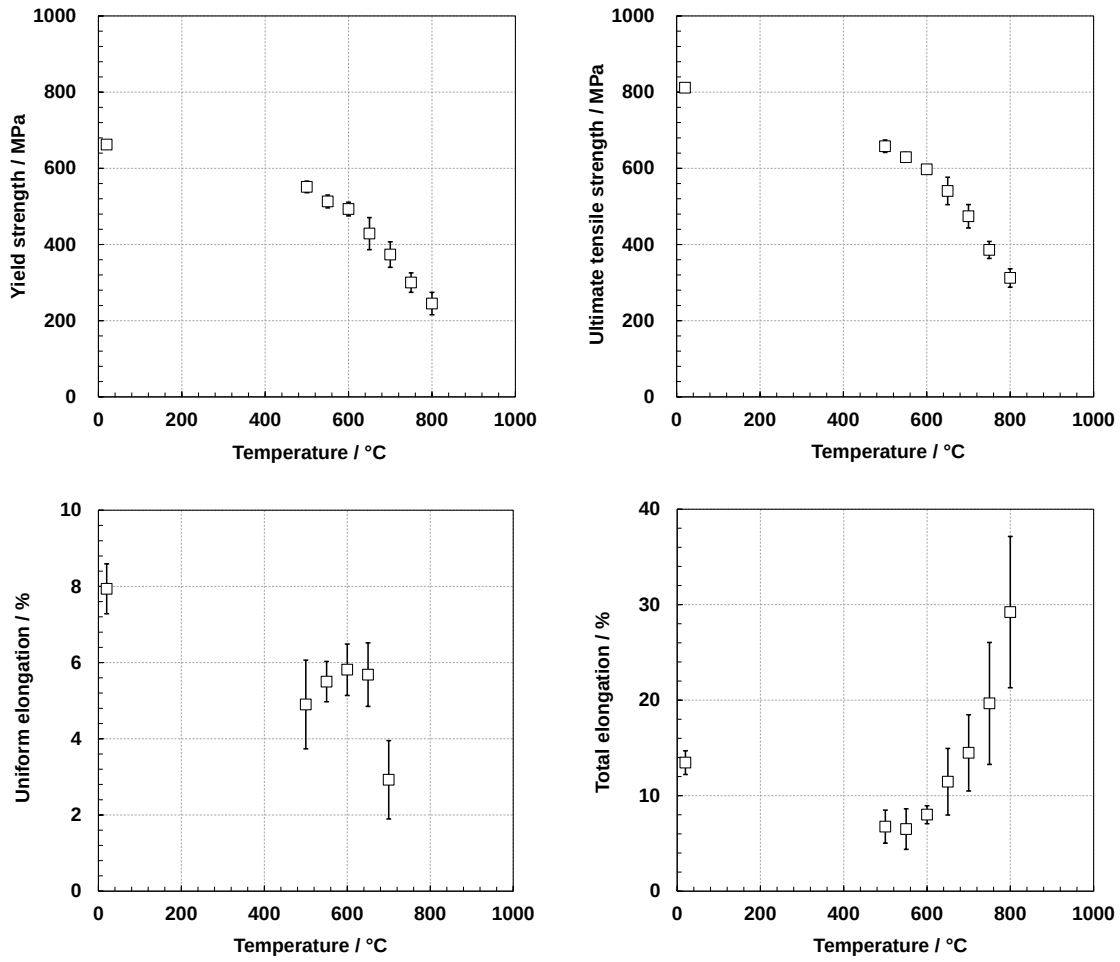

Figs. 1 Mechanical properties of as-received PNC316 as a function of temperature.

Table 1

Chemical compositions (wt%) of PNC316 cladding tube.

Steel grade / Lot		C	Si	Mn	P	S	Cr	Ni	Mo	Co	B	N	Cu	Ti	V	Nb + Ta
PNC316	55MK*	0.052	0.82	1.83	0.028	0.009	16.52	13.84	2.49	0.01	0.0031	0.003	0.01	0.080	0.01	0.079
	60MK**	0.054	0.78	1.72	0.028	0.003	16.22	13.45	2.35	0.01	0.0039	0.009	0.04	0.078	0.01	0.080
	60MS***	0.056	0.80	1.91	0.028	0.002	16.50	13.77	2.59	<0.01	0.0037	0.003	0.03	0.077	<0.01	0.091

*55MK: 1080ºC×2min. + CW20%
**60MK: 1080ºC×2min. + CW18%
***60MS: 1095ºC×1min. + CW20.8%

Table 2

Mechanical properties of PNC316 in the as-received condition.

Hardness				Tensile properties									
		Hardness, *H*v				YS / MPa		UTS / MPa		UE / %		TE / %	
Lot	Test temperature / °C	Average	S.D.*1	Lot	Test temperature / °C	Average	S.D.*1	Average	S.D.*1	Average	S.D.*1	Average	S.D.*1
55MK	20	252	12	55MK	20	662	9.8	812	5.5	7.9	0.7	13.5	1.2
60MK	20	279	7	55MK	500	551	15.2	658	16.4	4.9	1.2	6.8	1.7
60MS	20	270	5	55MK	550	513	17.0	629	12.4	5.5	0.5	6.5	2.1
				55MK	600	493	18.0	597	6.8	5.8	0.7	8.0	0.9
				55MK	650	429	42.1	541	36.0	5.7	0.8	11.5	3.5
				55MK	700	374	33.6	474	30.8	2.9	1.0	14.5	4.0
				55MK	750	300	25.6	386	22.4	–	–	19.7	6.4
				55MK	800	245	29.5	312	24.2	–	–	29.2	7.9

*1 S.D.: Standard deviation

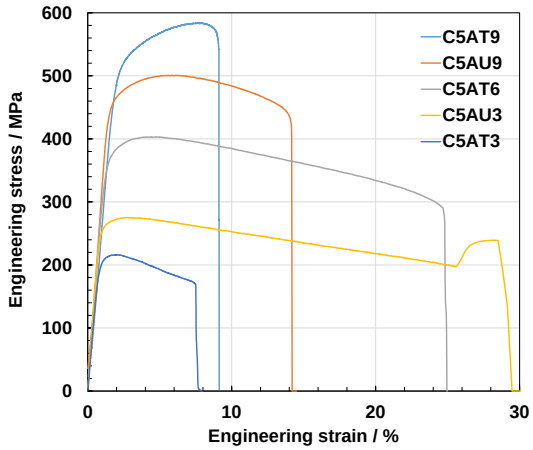

(a) CMIR-1

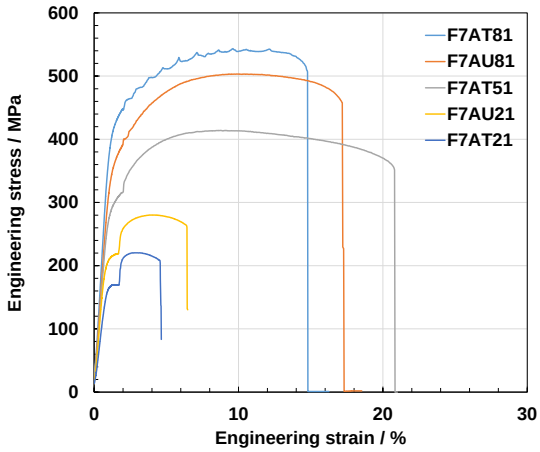

(b) CMIR-3

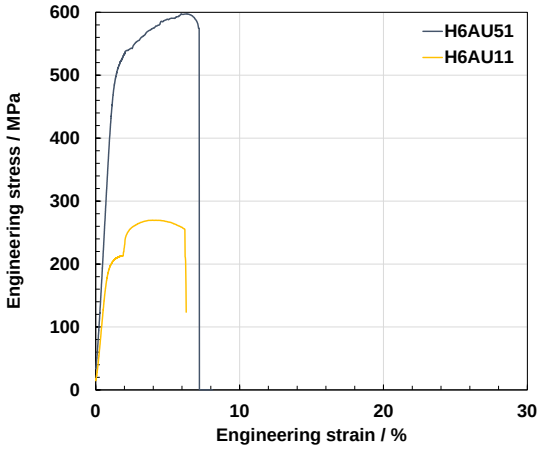

(c) CMIR-4

Figs. 2 Engineering stress-strain curves of PNC316 irradiated in the campaign of (a) CMIR-1, (b) CMIR-3, and (c) CMIR-4.

Table 3

Irradiation conditions, hardness and tensile test results of PNC316 cladding tube.

No.	Rig	Irradiation time / h	Fluence[*1] / 10^{26} n·m^{-2}	Irradiation temperature[*2] / °C	Hardness					Tensile properties						
					Specimen ID	Lot	Test temperature / °C	Hardness[*3], *H*v	S.D.	Specimen ID	Lot	Test temperature / °C	YS / MPa	UTS / MPa	UE / %	TE / %
1	CRIM-1	3852	3.2	502	C5EG51	55MK	20	299	6	—	—	500	—	—	—	—
2		3852	3.9	569	C5EG81	55MK	20	260	7	C5AT9	60MK	550	488	582	5.5	7.1
3		3852	3.9	589	C5EG61	55MK	20	264	9	C5AU9	60MS	600	445	501	4.1	12.9
4		3852	4.0	628	C5EG41	55MK	20	266	3	C5AT6	60MK	650	350	400	3.0	24.2
5		3852	4.0	709	C5EG11	55MK	20	257	7	C5AU3	60MS	700	248	269	1.8	27.7
6		3852	3.8	734	—	—	—	—		C5AT3	60MK	740	199	216	1.2	7.9
7	CMIR-3	14400	15.5	569	F7AT82	60MK	20	251	6	F7AT81	60MK	550	404	544	8.6	14.0
8		14400	14.7	628	F7AT52	60MK	20	262	6	F7AT51	60MK	650	280	414	7.5	19.6
9		14400	14.9	734	F7AT222	60MK	20	204	5	F7AT21	60MK	750	165	220	1.6	3.4
10		14400	15.2	589	F7AU82	60MS	20	264	4	F7AU81	60MS	600	342	503	8.9	15.9
11		14400	15.5	709	F7AU22	60MS	20	218	6	F7AU21	60MS	700	205	279	3.1	5.6
12	CMIR-4	18624	15.9	502	H6AU52	60MS	20	310	10	H6AU51	60MS	500	496	597	4.9	5.9
13		18624	20.6	709	H6AU12	60MS	20	231	3	H6AU11	60MS	700	198	269	2.9	4.8

*1 $E > 0.1$ MeV
*2 CMIR-1 assessed temperature
*3 Hardness measurement was carried out in the thickness-center of the cladding tube.

Yield strength of PNC316 reduced after neutron irradiation throughout the temperature and the dose range in the present study, as seen in Fig 3a. The change of the yield strength ($\Delta\sigma_y$) increased with increasing the irradiation temperature and the irradiation dose. Fig. 3b shows Vickers hardness (*H*v) as a function of irradiation temperature. The hardness decreased with increasing the irradiation temperature. Note that all hardness tests were done in room temperature. From a viewpoint of the change of the hardness (ΔHv), the alloy irradiated at around 500 °C showed hardening, while the one irradiated at around 700 °C showed softening. Just for a reference, mechanical properties after irradiation are plotted as a function of neutron fluence in Fig. 4.

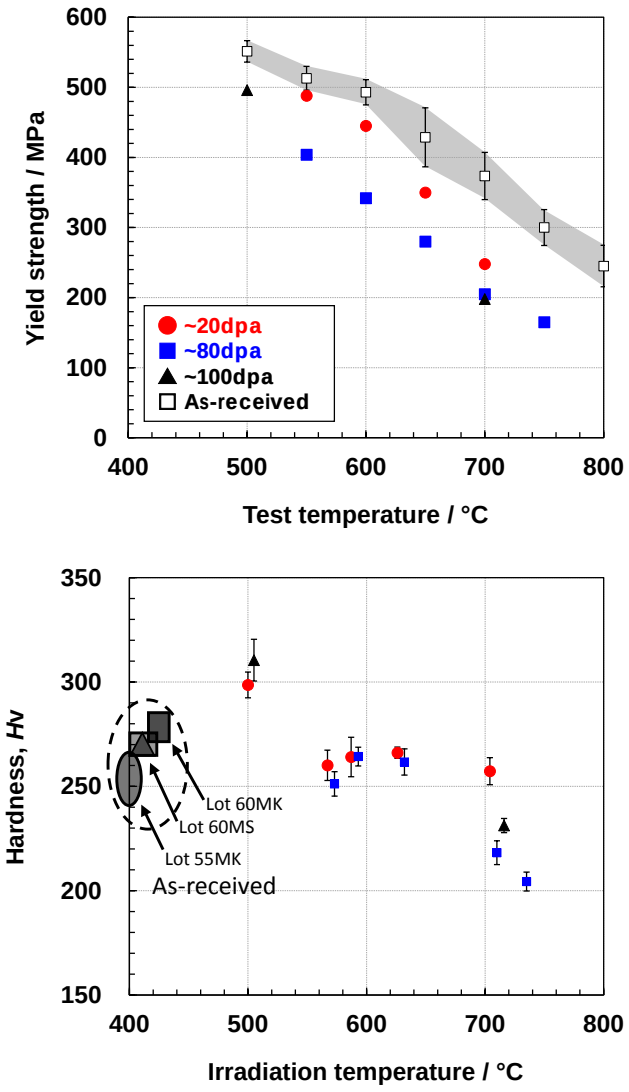

Fig. 3 (a) Yield strength and (b) Vickers hardness of PNC316 before and after irradiation as function of temperature.

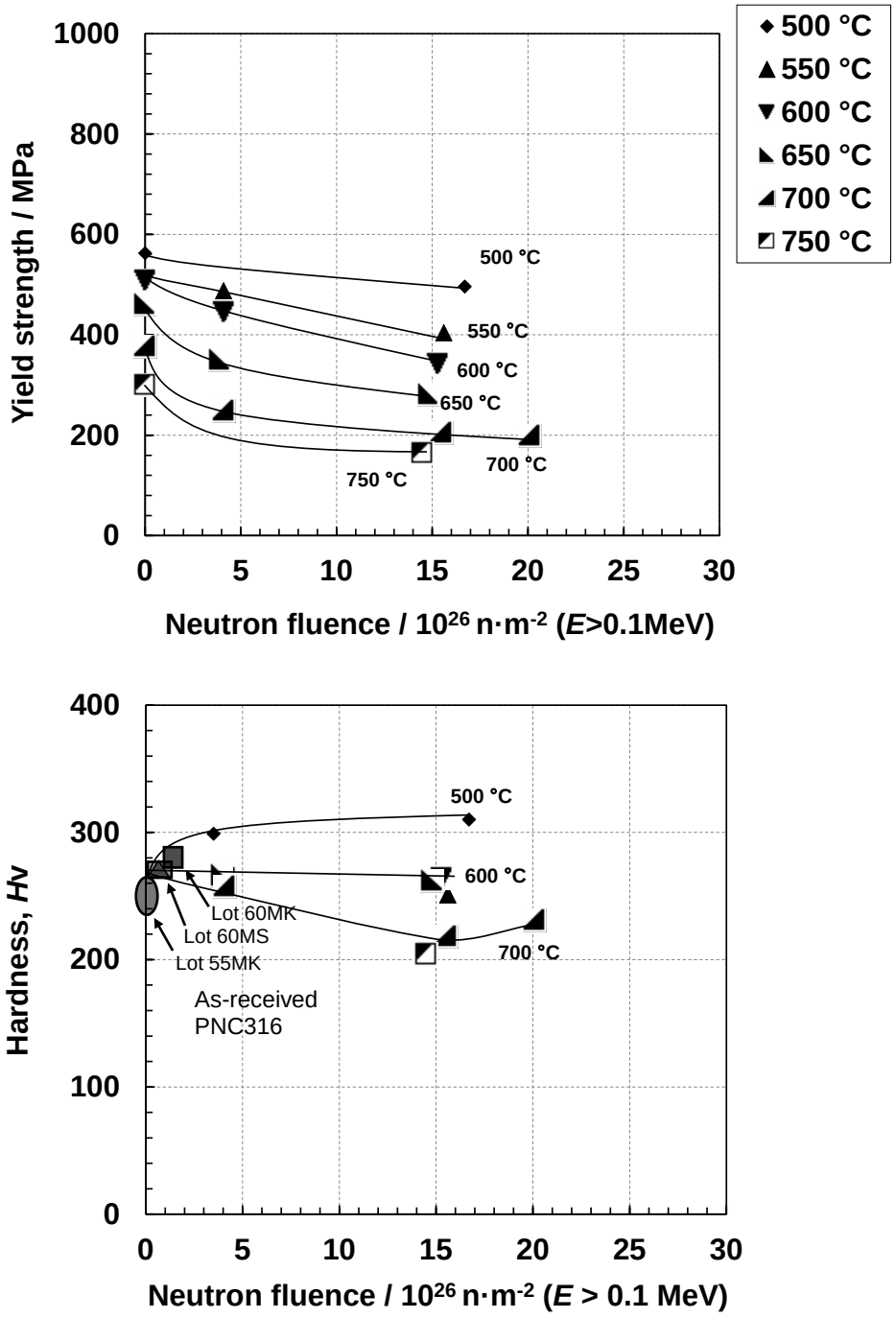

Fig. 4 Mechanical properties of PNC316 after irradiation as a function of irradiation dose. (a) Yield strength and (b) Vickers hardness.

2.5 Microstructure before and after irradiation

The softening and hardening shown in Fig. 3 should result from microstructure changes due to the long term neutron irradiation. To reveal the microstructural change due to irradiation, TEM observation was carried out for the irradiated sample. As a summary, all of the microstructural parameter after irradiation are listed in Table 4. Note that the foil thickness of the sample observed in TEM, which is necessary to the determination of defect densities, was assumed to be around 100 nm.

Fig. 5 shows the typical microstructure of as-received and irradiated PNC316 up to more than 75 dpa at 502, 589 and 709 °C. As seen in Fig. 5a, heavily tangled dislocations and many deformation bands or twins were observed in as-received PNC316. They are due to 20 % cold working in a manufacturing process which gives them a high creep strength and irradiation resistance as a cladding tube. No precipitate formation was found in as-received condition.

In the microstructure irradiated at 502 °C, the tangled dislocation structure almost remained while irradiation dose was up to 79.5 dpa. A small density (10^{19} m^{-3}) of precipitates was observed after neutron irradiation and the density of precipitates increased with increasing dose. Small voids were observed at 79.5 dpa while no voids were observed at 16.0 dpa. Besides, very small number of Frank loop were observed in the sample irradiated at 502 °C up to 16.0 and 79.5dpa. Moreover, the formation of needle shape precipitate, which would be a hexagonal Fe_2P [3], was observed in 79.5dpa sample.

In irradiation at 550–650 °C, tangled dislocation still remained, similar to as-received condition. The dislocation density was around $2–3\times10^{14}$ m^{-2}, while it was decreased to 0.96×10^{14} m^{-2} after irradiation at 628°C up to 73.5dpa. Moreover, relatively large precipitates were observed both within grain and on grain boundary. These precipitates are considered to be Laves phase, M_6C and $M_{23}C_6$ precipitates [4]. Needle shape precipitates were also observed in this temperature range (Fig. 6). A void formation was clearly observed in this temperature range at a dose over 75dpa (Fig. 7).

In irradiation at more than 700 °C, the tangled dislocation mostly recovered to the density of ~ 10^{13} m^{-3} whereas the density in as-received condition was ~ 10^{14} m^{-3}, as seen in Fig. 5d. Precipitates grew significantly and no voids were observed at this temperature range. Needle shape precipitates were not observed.

Grain growth were observed after neutron irradiation. Grain size in as-received condition was 11–13 μm while that after irradiation was around 16–17 μm (table 4). Note that grain size measurement for the sample irradiated at over 700 °C did not work because the resultant surface after etching was not clear so it was inappropriate for measurement of the grain boundary in an optical microscope. An inappropriate etched-surface might be due to a lot of large precipitate formed within grain or on grain boundary which was etched preferentially. A further investigation for grain size measurement such as SEM observation is necessary. For this purpose, the SEM facility which can operate for radioactive sample is definitely necessary.

The schematics showing microstructural evolution of PNC316 under neutron irradiation in several condition are in Fig. 8.

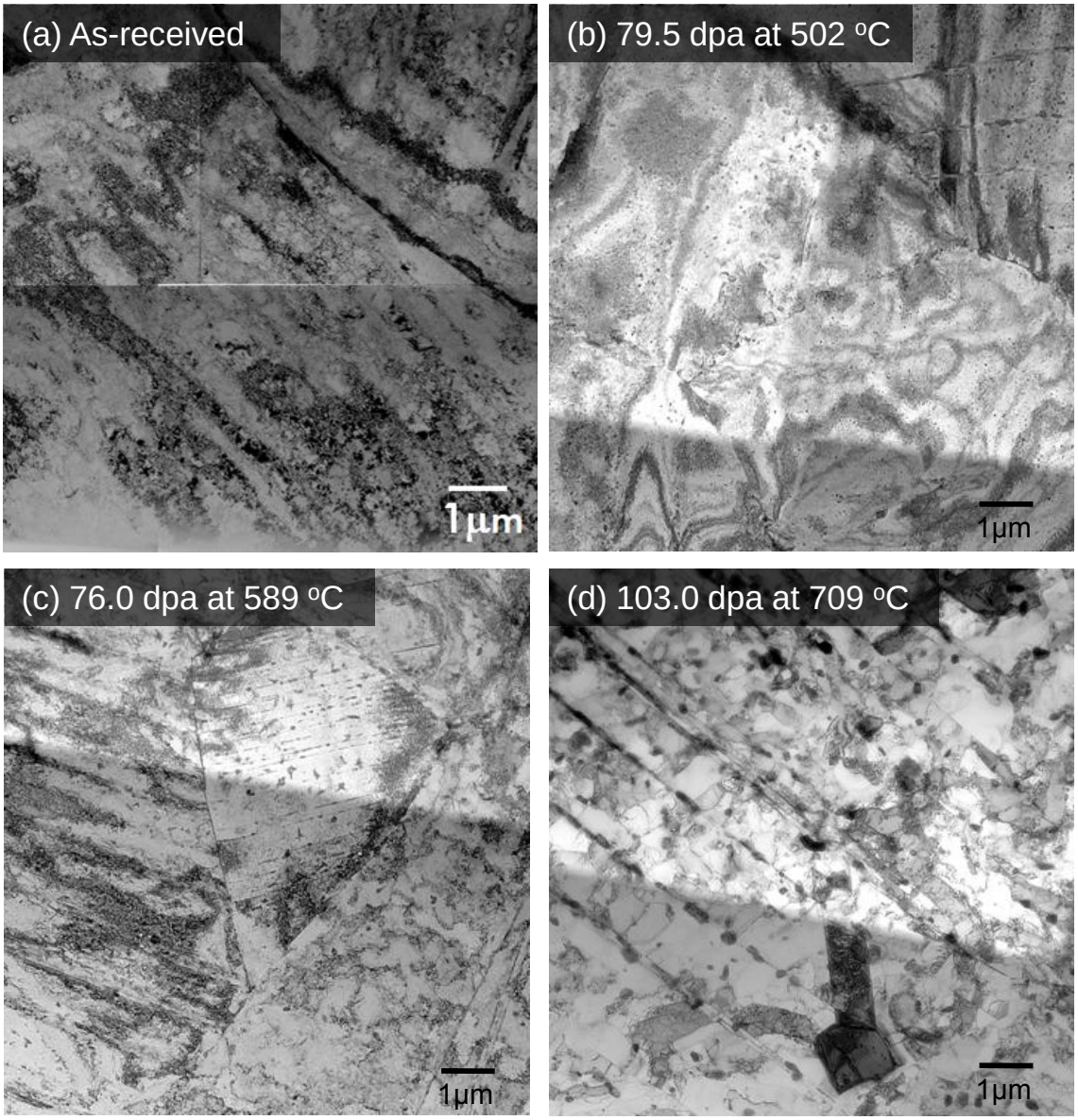

Fig. 5 Typical microstructure in PNC316 before and after irradiation. (a) is an image in the unirradiated specimen, (b) (c) and (d) are in the specimens irradiated up to 79.5 dpa at 502 °C, 76.0 dpa at 589 °C, and 103.0 dpa at 709 °C, respectively.

Table 4

Summary of radiation-induced microstructure characterization of PNC316 cladding tube neutron-irradiated to 100 dpa at 500–750°C.

ID	Lot	Fluence[*1] / 10^{26} n·m^{-2}	Irradiation temperature[*2] / °C	Block shape precipitates		Needle shape precipitates			Voids			Dislocation density / 10^{14} m^{-2}	Grain size / μm
				Number density / 10^{19} m^{-3}	Diameter / nm	Number density / 10^{20} m^{-3}	Diameter (long axis) / nm	Diameter (short axis) / nm	Number density / 10^{19} m^{-3}	Diameter / nm	Void-to-void distance / nm		
55MK as received	55MK											2.23	11.3
60MK as received	60MK											—	13.7
60MS as received	60MS											—	11.8
650°C 6000h													13.7
700°C 6000h													18.2
750°C 6000h													19.4
C5EG51T	55MK	3.2	502	0.6	80.5	—	—	—	—	—	—	2.0	
C5EG81T	55MK	3.9	569	1.2	66	4.0	20.7	4.3	—	—	—	3.2	14.5
C5EG61T	55MK	3.9	589	1	65.5	4.8	30.1	4.5	—	—	—	3.3	14.3
C5EG41T	55MK	4.0	628	2.7	106.2	12.8	22.1	4.2	—	—	—	3.5	14.2
C5EG11T	55MK	4.0	709	3.3	135.3	—	—	—	—	—	—	1.6	
F7AT82T	60MK	15.5	569	2.1	95.5	9.1	34.2	4.4	1.1	74.5	120.5	2.6	16.9
F7AT52T	60MK	14.7	628	3.6	227.5	8.8	42.2	4.0	2.5	108.2	32.7	0.96	
F7AT22T	60MK	14.9	734	1.3	198.7	—	—	—	—	—	—	0.92	
F7AU82T	60MS	15.2	589	3.1	123.3	7.5	34.1	4.5	0.5	45.1	353.6	2.3	17.3
F7AU22T	60MS	15.5	709	1.4	188.9	—	—	—	—	—	—	0.74	
H6AU52T	60MS	15.9	502	5.4	73.2	9.6	24.9	5.3	1.51	21.8	48.8	3.2	15.32
H6AU12T	60MS	20.6	709	1.9	247.6	—	—	—	—	—	—	0.88	

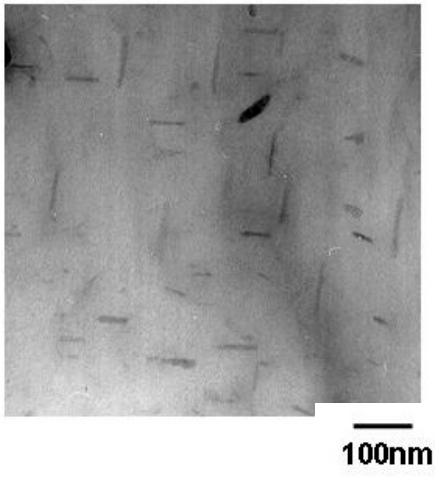

Fig. 6 Needle type precipitate in PNC316 after irradiation at 569°C up to 77.5dpa (CRIM-3, F7AT82T, 60MK)

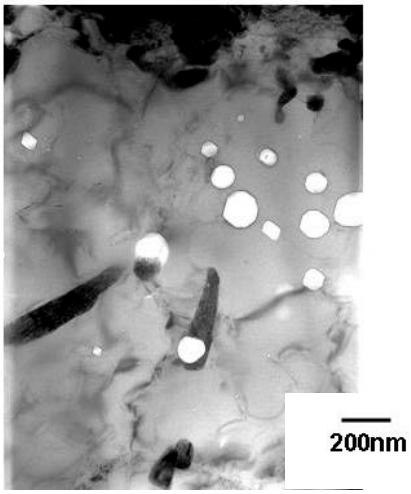

Fig. 7 Voids formed in PNC316 after irradiation at 628°C up to 73.5dpa (CRIM-3, F7AT52T, 60MK)

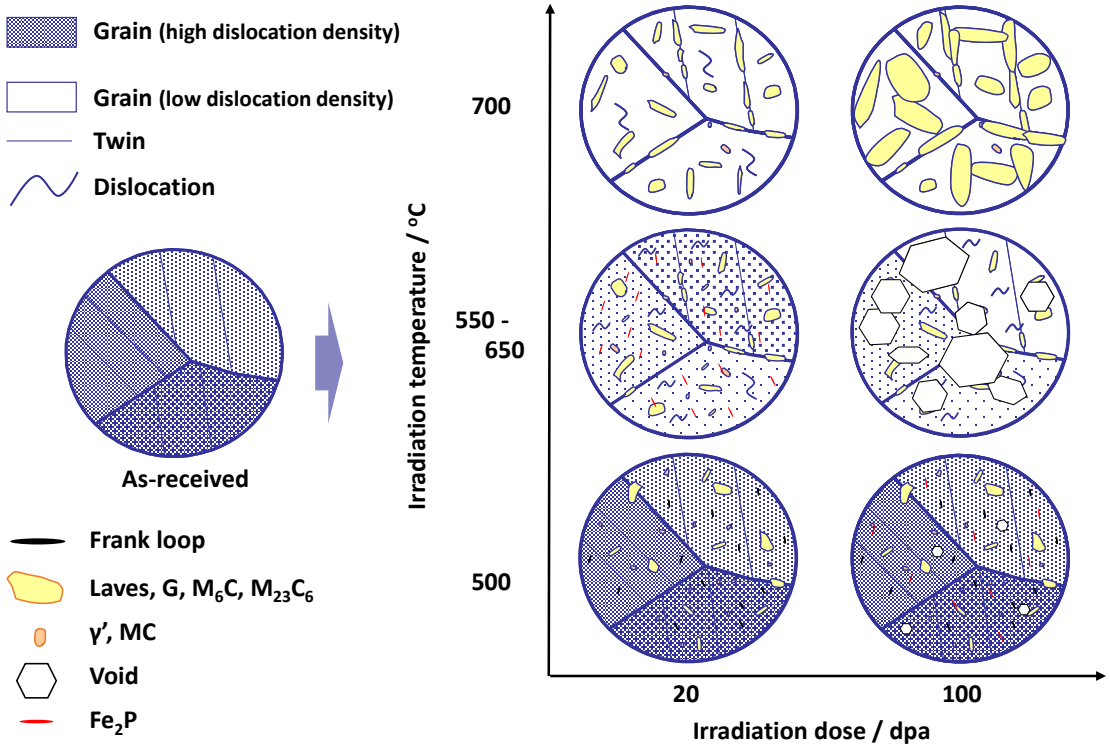

Fig. 8 Schematics showing microstructural evolution of PNC316 under neutron irradiation in several condition.

2.6 Estimation of yield strength by Orowan's equation

2.6.1 Outline of the estimation

Yield strength of PNC316 after irradiation was estimated using Orowan's equation. In this study, obstacles for moving dislocation in irradiated PNC316 are forest dislocations, grain boundary, needle type precipitates, coarse precipitates and voids. Here actual equations for each types of obstacles are described as

Forest dislocation $\Delta\sigma_{y,\,d} = M\alpha_{d2}\mu b(\rho_{d2})^{1/2} - M\alpha_{d1}\mu b(\rho_{d1})^{1/2}$ (1)

Grain boundary $\Delta\sigma_{y,\,D} = k\,(D_2^{-1/2} - D_1^{-1/2})$ (2)

Needle precipitates $\Delta\sigma_{y,\,np} = M\alpha_{np}\mu b(N_{np}d_{np})^{1/2}$ (3)

Laege precipitates $\Delta\sigma_{y,\,lp} = M\alpha_{lp}\mu b(N_{lp}d_{lp})^{1/2}$ (4)

Voids $\Delta\sigma_{y,\,v} = M\alpha_{v}\mu b(N_{v}d_{v})^{1/2}$ (5)

where M, α, μ, b and ρ_d are the Taylor factor, the barrier strength of obstacles, the shear modulus of the matrix, the Burger's vector of moving dislocation and the total density of dislocations, respectively. Here, eq. (2) are also known as Hall–Petch relationship [5][6].

To sum each of these yield strength change, following two types of equation have a potential to be considered.

$$\Delta\sigma_y = \Delta\sigma_{y,\,dy} + \Delta\sigma_{y,\,D} + \Delta\sigma_{y,\,np} + \Delta\sigma_{y,\,lp} + \Delta\sigma_{y,\,v} \quad (6)$$

$$\Delta\sigma_y = \Delta\sigma_{y,\,d} + \Delta\sigma_{y,\,D} + \{(\Delta\sigma_{y,\,np})^2 + (\Delta\sigma_{y,\,lp})^2 + (\Delta\sigma_{y,\,v})^2\}^{1/2} \quad (7)$$

Equation (6) is a simple sum of each term, while equation (7) is a combination of square-root of sum of squares and simple sum. Eq. (7) is based on the concept for short-range obstacles [7][8]. In this work, short-range obstacles could be needle type precipitates, coarse precipitates and voids, while long-range obstacles are forest dislocations and grain boundary.

2.6.2 Strength factor for each types of obstacles

2.6.2.1 Forest dislocation

Here, the strength factor for forest dislocation, $\alpha_{d1} = \alpha_{d2} = 0.24$ was used. This value was experimentally evaluated for solution-annealed PNC316 sample. The details for α value evaluation method will be described in Chapter 3. The obtained relationship between square root of dislocation density and yield strength is shown in Fig. 9. Here, it is well known that the relationship between yield strength and dislocation density is described as

$$\sigma_y = \sigma_0 + M\alpha_d \mu b(\rho_d)^{1/2} \quad (8)$$

where σ_0 is a constant. Eq. (8) is usually known as Bailey-Hirsch relationship [9].

2.6.2.2 Grain boundary

The grain boundary strengthening parameter, *k*, is 10.46 MPa·mm$^{1/2}$ in this study, which is the value based on the work of Varin and Kurzydlowski[10]. They investigated the effect of nitrogen contents, various fractions of coherent twin boundaries per grain and an ultrafine-grained structure on the Hall-Perch relationship in several commercial heats of type 316 steel. Fig. 10 shows the plots derived from parameter σ_0 and *k* listed in table 2 in ref[10].

2.6.2.3 Needle precipitates

The strength factor for needle type precipitates, $\alpha_{np} = 0.33$ was used. This value is for small MC ppts referred from ref [1][11]. The size of needle precipitates which is used for the estimation is the length of short axis.

2.6.3 Other parameter in Orowan's equation

2.6.3.1 Shear modulus

The shear modulus of material depends on temperature. The linear relationship between shear modulus and temperature was found in type s16 stainless steel according to ref. [12] (see Fig. 11). Therefore, an appropriate value of shear modulus is used for each test temperature in the estimation on the basis of following empirical equation;

$$\mu = 74.7 - 3.1\times10^{-2}\,T \qquad (9)$$

where μ and T are the shear modulus of the matrix in GPa and test temperature in °C, respectively. For instance, the shear modulus at room temperature and 700 °C are obtained to be 74 and 53 GPa, respectively.

2.6.3.2 Burger's vector

Burger's vector of the material used in this study, PNC316, was experimentally measured by using XRD. PNC316 powder with 150 μm in diameter produced by argon gas atomization process was used for XRD measurement. Results are shown in Fig. 12, and resultant Burger's vector in F.C.C. PNC316 is to be 2.546 Å.

2.6.3.3 Taylor factor

Taylor factor, *M*, was 3.06 [13][14] in this study. Stoller and Zinkle [14] reviewed variety of radiation effect literature and found that there is some confusion regarding the choice of this conversion factor for polycrystalline specimens. Some authors have used values of 1.73 and 2.0, based on an inappropriate application of the von Mises and Tresca yield criteria, respectively. They recommended as a summary that the value of 3.06 be used to provide a standard basis of comparison when publishing results of microstructure-mechanical property correlations.

Table 5
Comparison of obstacle strengths [1].

Relative strength	Barrier type	System	α	Reference
Strong	Orowan	—	1	
	Voids	Austenitic	~1	[15]
	Voids	Ni	~1	[16]
	Voids	Austenitic	~1	[8]
	Voids	Austenitic	~1	[17]
	Large precipitates	Austenitic	~1	[17]
Intermediate	Frank loops	Austenitic	0.33	[8]
	Frank loops	Austenitic	0.45	[11]
	Frank loops	Austenitic	0.45	[17]
	Small MC ppts	Austenitic	0.33-0.45	[11]
Weak	Small bubbles	Austenitic	0.2	[8]
	Small loops / clusters	Austenitic	0.2	[18]
	Vacancy clusters	—	<0.25	[19]
	Dislocations	—	0.15–0.3	[20]
	Dislocations	Austenitic	~0.11	[8]
	Dislocations	Austenitic	0.2	[17]

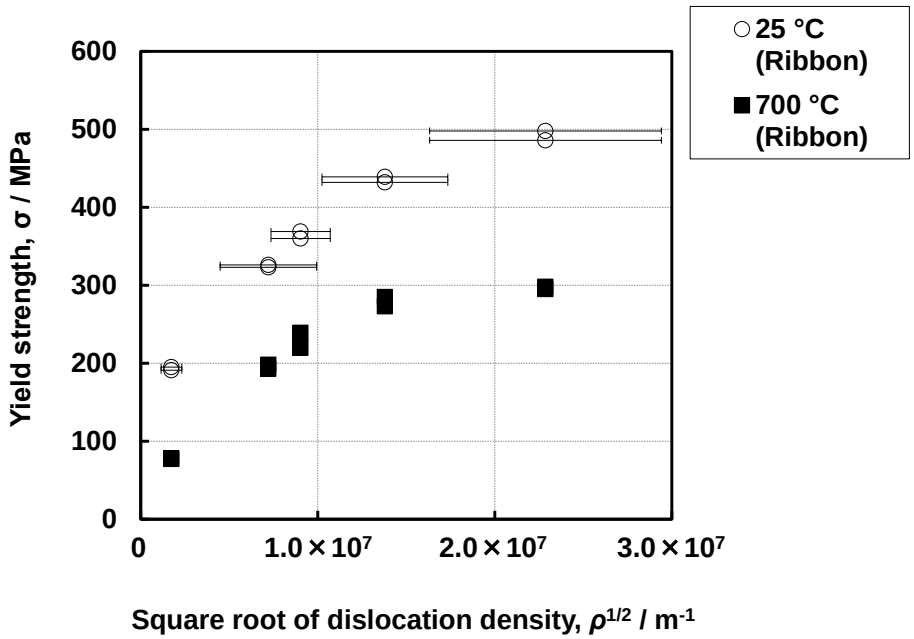

Fig. 9 Yield strength of solution-annealed PNC316 stainless steel as a function of square root of dislocation density tested at 25 and 700°C.

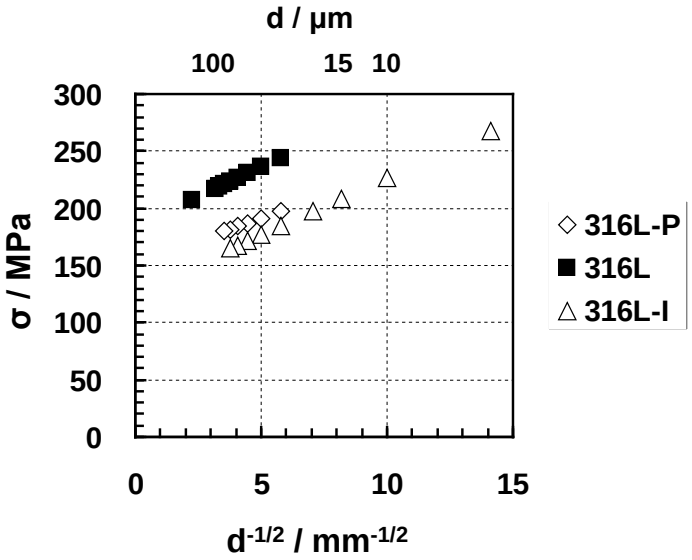

Fig. 10 Yield strength in several commercial heats of type 316 steel as a function of the reciprocal of square root of grain size. The plots is derived from parameter σ_0 and k listed in table 2 in ref[10].

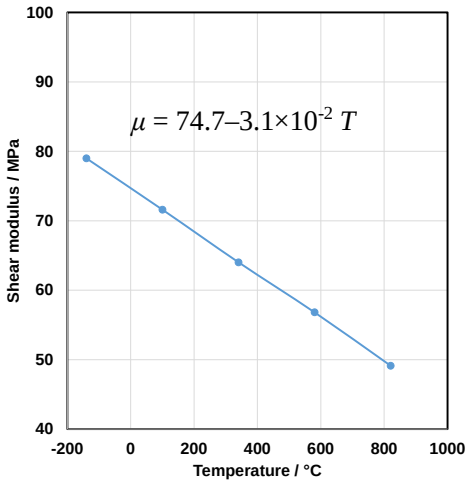

Fig. 11 Temperature dependence of the modules of rigidity in type 304 and type 316 steel [20].

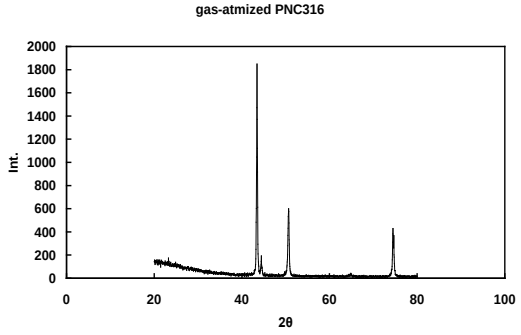

	2θ	d	I / I0	h	k	l	a
1	43.480	2.0796	100	1	1	1	3.6020
2	44.440	2.0369	10				
3	50.680	1.7998	35	2	0	0	3.5996
4	74.480	1.2729	25	2	2	0	3.6003
5	74.680	1.2700	18				
Ave.							3.6006

Fig. 12 X-ray diffraction pattern of argon gas atomized PNC316 powders.

2.7 Results of estimation

2.7.1 Comparison to tensile test results

The results of the estimation of yield strength derived from eq. (1)–(7) are shown in Fig. 13 with error bars. The experimentally-obtained change in yield strength are also shown in Fig. 13. The band in Fig. 13 represents the error for experimental data. In this case, the contribution of coarse precipitates and voids on yield strength are neglected due to its low number density (the order of -10^{19}m^{-3}) shown in Table 4. Thus, eq. (6) become practically the same as eq. (7).

Comparing the estimation of yield strength to tensile test result, it must be noted that tensile tests were performed at irradiation temperature so effect of test temperature should be reflected in the estimation. For this purpose, effect of test temperature is reflected in the term of shear modulus.

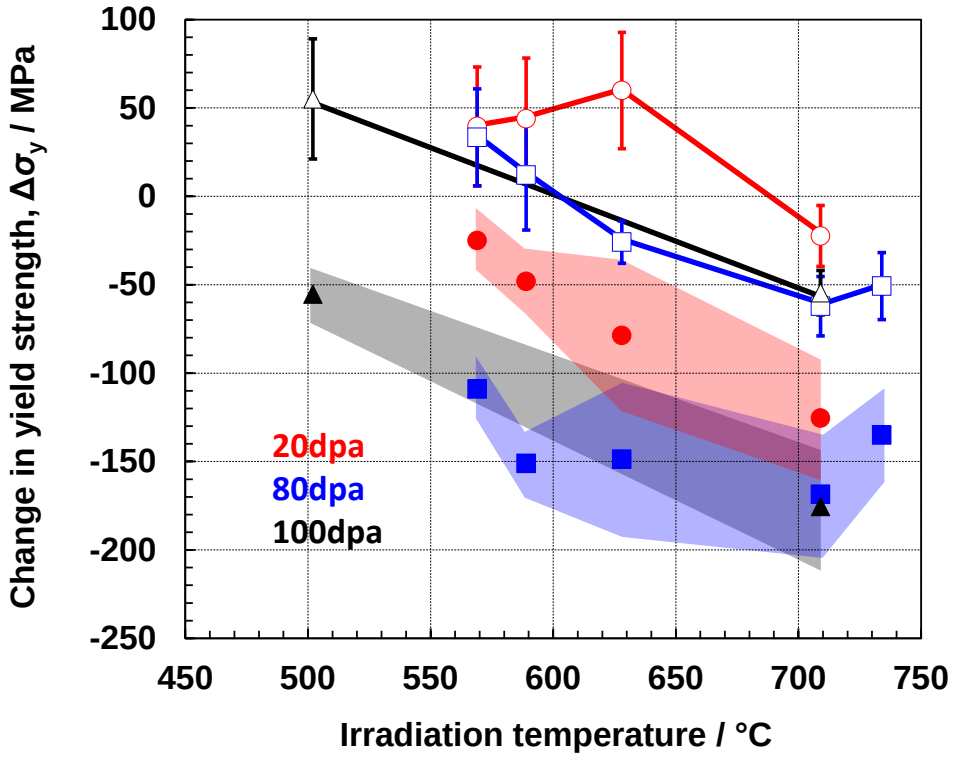

Fig. 13 Estimated change in yield strength derived from eq. (1)–(7) as a function of irradiation temperature. Estimated value are plotted with unfilled symbols and solid line. The change in yield strength in experimental data are also shown with filled symbols and error bands. The strength factor for forest dislocation, $\alpha_{d1} = \alpha_{d2} = 0.24$ was used.

In Fig. 13, there are wide gaps between the estimated yield strength and the experimentally-obtained yield strength over the whole temperature range and the whole dose range of this study. The magnitude of the gaps was almost 100–150 MPa. Comparing their data trend, they correspond with each other as it decrease with increasing irradiation temperature. The results here allow the conclusion that Orowan's equation, whose detailed description are given above, is able to reconstruct the data trend of yield strength change but not its absolute value.

2.7.2 Comparing to hardness test results

The estimation of yield strength are also compared with experimentally-obtained change in hardness, shown in Fig 14. Symbols, error bars, and error bands are used in the same manner as in Fig. 13. The contribution of coarse precipitates and voids are also

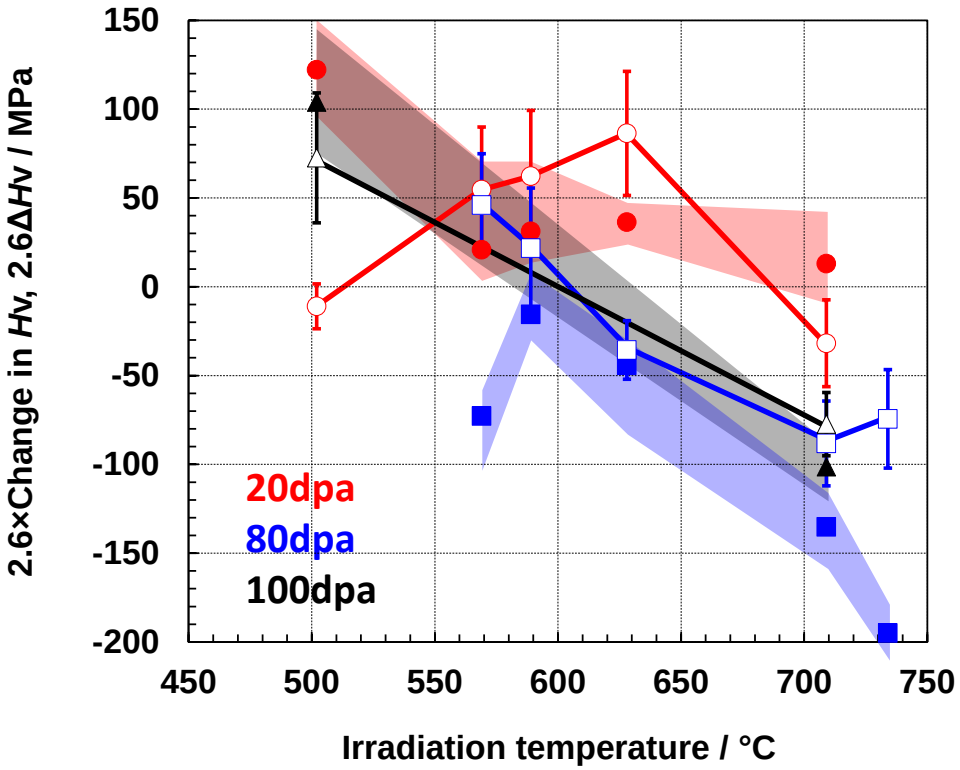

Fig. 14 Comparison between estimated change derived form Orowan's eq.–change in hardness. Estimated value are plotted with unfilled symbols and solid line. Experimentally-obtained change in hardness are shown with filled symbols and error bands. The strength factor for forest dislocation, $\alpha_{d1} = \alpha_{d2} = 0.24$ was used.

neglected here. When comparing to hardness results, the value of shear modulus at room temperature are used in the estimation because hardness test were performed at room temperature.

Here it must be noted that Orowan's eq. can estimate the change in yield strength, while mechanical property change here is hardness. So it is not possible to directly compare these value. Now we need the following equation: the conversion of the change in hardness into the change in yield strength ($\Delta Hv \rightarrow \Delta\sigma_y$),

$$\Delta\sigma_y = 2.6\Delta Hv \qquad (10)$$

with σ_y expressed in MPa and Hv in kg mm^{-2}. This is evaluated from following experiment:

We correlated Vickers hardness testing and uniaxial yield stress using tests on solution-annealed PNC316 samples cold-worked to various levels, resulting in hardness ranging from 150 to 220 kg mm^{-2}. This data is illustrated in Fig. 15. Both hardness and yield stress were measured at room temperature. The resulting correlation was linear in form,

$$\sigma_y = 2.6Hv - 61 \qquad (11),$$

also expressed in Fig. 15 where σ_y is in MPa and Hv is in kg mm^{-2}. This relation is quite similar to that of Bruemmer et al. [21] and Toloczko et al. [22], both in form and in magnitude of the coefficients. A subtle difference of the intercept between eq. (11), (12), and (13) are attributed the difference in materials, heat treatment, and the way of cold working (rolling vs. uniaxial stretching).

Bruemmer et al. [21] $\sigma_y = 2.6Hv - 195$ (12)

Toloczko et al. [22] $\sigma_y = 2.7Hv - 125$ (13)

Note here that eq. (12) is derived by Oka from the data originally shown in Figure 2–5 in Ref. [21].

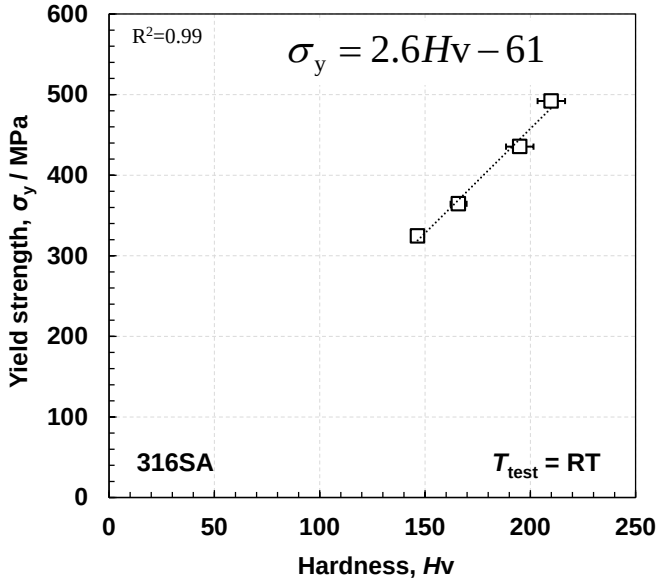

Fig. 15 Correlation between hardness and 0.2% yield strength in solution annealed PNC316 stainless steel. Correlation coefficient, R_2, was 0.99. This relation was used for converting hardness data to yield stress.

In Fig. 14, gaps between the estimated yield strength and experimentally-obtained yield strength derived from hardness change appear to be small compared to that in Fig. 13. Especially, irradiation up to more than 80 dpa, the estimation is in good agreement with experimental data. However the data for irradiation up to 20dpa at 509°C (Red line) and that for irradiation at 569 and 734°C up to 80dpa show big gaps. The results here allow the conclusion that Orowan's equation is able to reconstruct the belief data trend and absolute value of experimentally-evaluated yield strength change derived from hardness change.

2.7.3 Difference in tensile test and hardness test

As mentioned above, the yield strength of PNC316 decreased after long term neutron irradiation. On the other hand, the hardness, measured at room temperature, showed both the softening and the hardening. For instance the alloy irradiated at 502 °C showed the softening in the yield strength whereas that showed the hardening in the hardness (see Fig. 3). Meanwhile, the one irradiated at more than 700 °C showed the softening in the yield strength and hardness. According to TEM observation, the softening at around 700 °C is mainly due to a recovery of tangled dislocation structure as seen in Fig. 16 describing the dislocation density as a function of irradiation temperature.

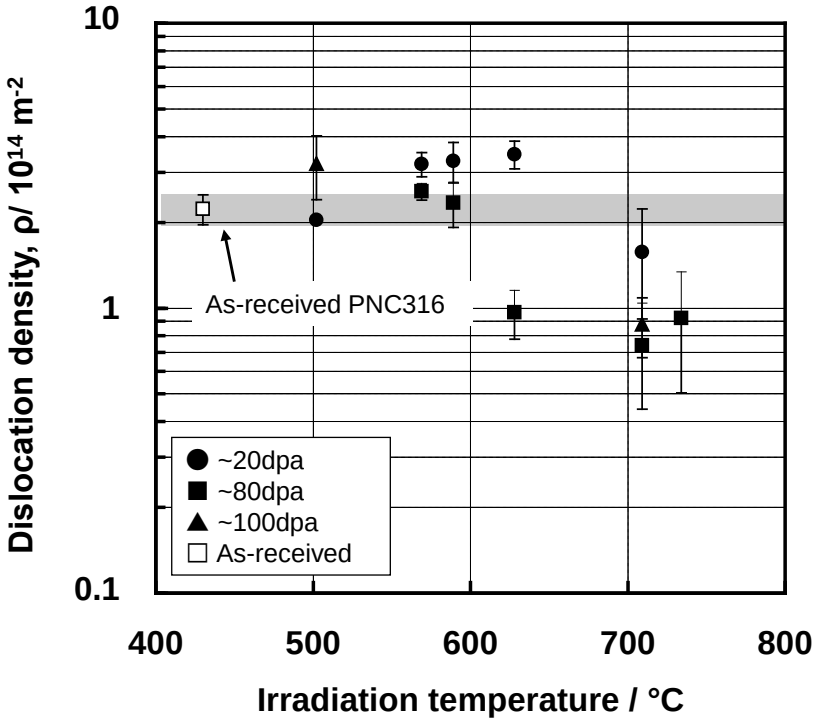

Fig. 16. Dislocation densities in PNC316 before and after irradiation as a function of irradiation temperature.

In the alloy irradiated at 502 °C, it can be pointed out again that, although the dislocation density after irradiation is almost the same level as that before irradiation, it showed the softening in the yield strength whereas that showed the hardening in the hardness. These fact may be reflected in the deferent behavior among change in yield strength and that in hardness, in comparison to the estimated strength.

A difference between the tensile test and the hardness test in the present study is the test temperature. Again, tensile tests for irradiated material were performed at irradiation temperature (Table 2). While hardness test was performed at room temperature for every single sample. Although temperature effect was considered as the shear modulus depends on temperature in the estimation, they still have gaps (Fig. 13 and 14).

One idea to be able to explain this gap is discussing the factor depending on temperature except the shear modulus. Again, Orowan's equations for forest dislocations is described as:

$$\Delta\sigma_{y,\,d} = M\alpha_{d2}\mu b(\rho_{d2})^{1/2} - M\alpha_{d1}\mu b(\rho_{d1})^{1/2} \qquad (1).$$

In the eq. (1), M, b, and ρ cannot depend on temperature. The shear modulus μ depends on temperature, mentioned above. Here, the barrier strength of dislocations, α_d, may have a potential to depend on temperature, but no discussion on this have been done in the past study among metallurgy.

2.7.4 Where are carbon atoms in the material?

Figure. 17 shows the ratio of amount of carbon in precipitates to total amount of carbon in the irradiated PNC316 sample as a function of irradiation temperature. In vertical axis, C_{ppt} denotes the amount of carbon in precipitates, while C_{total} denotes the total amount of carbon in the material. Here, the value of 1 in vertical axis means that all of carbon atoms in the sample exists in the form of precipitates. The amount of carbon in precipitates was assumed from TEM images. The precipitates with aspect ratio of 1–1.5 were counted for the assumption. Precipitates with aspect ratio lager than 1.5 was not counted in the assumption. For the rhombus symbol, all the precipitates were considered to be M_6C type, while for the square symbol all the precipitates were considered to be $M_{23}C_6$ type. Crystallographic data of precipitate phases are summarized in Table 6. As shown in Fig.17, most of the carbon atoms are existing in the form of carbide after neutron irradiation in the dose of 80–100 dpa. It means that the concentration of carbon in matrix might be very low. This fact here allow the conclusion that the effect of the depletion of

carbon atoms from the matrix need to be considered when yield strength is estimated. The depletion of carbon atoms after irradiation would suggest a possible change of the barrier strength of dislocation, α_d, before/after irradiation.

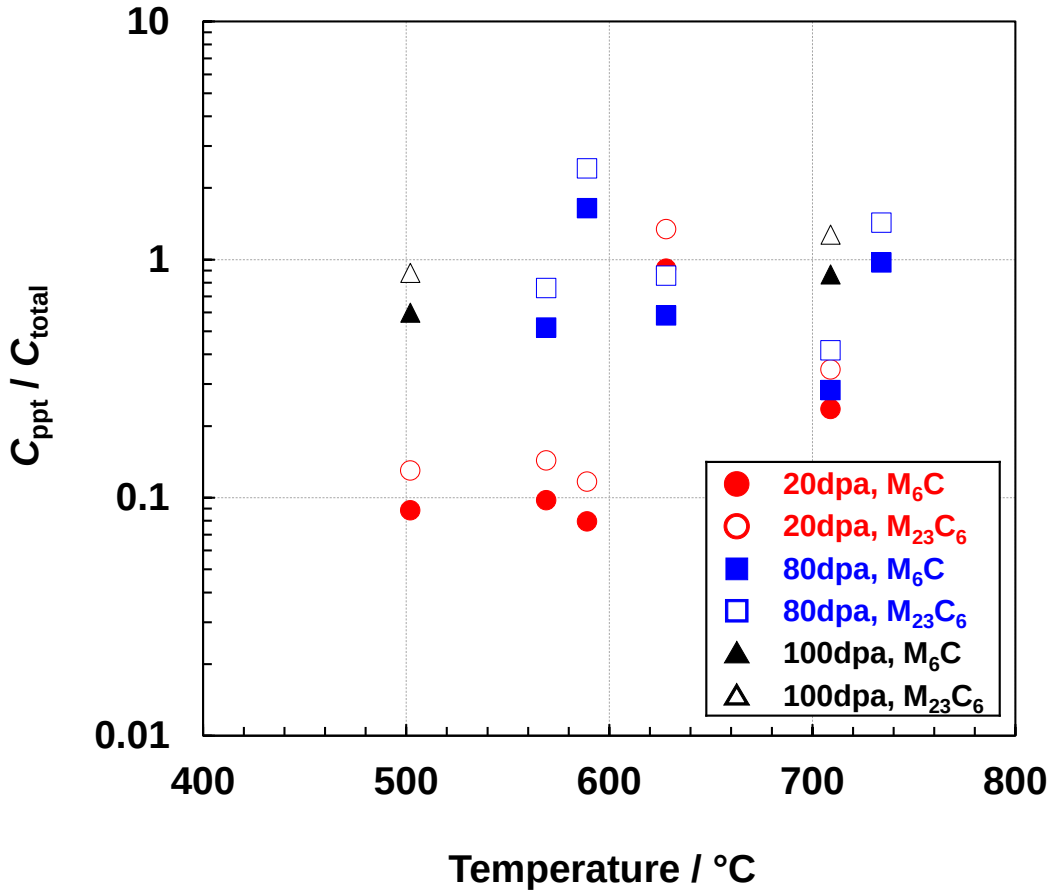

Figure. 17 Amount of carbon atoms in the form of precipitates in PNC316 after irradiation as a function of irradiation temperature. C_{ppt} denotes the amount of carbon in precipitates, while C_{total} denotes the total amount of carbon in the material. The value of 1 in vertical axis means that all of carbon atoms in the sample exists in the form of precipitates.

Table 6
Summary of crystallographic data of precipitate phases [4].

Phases	Crystal Structure	Lattice Parameter / nm	Solute Atoms per Unit Cell	Typical Morphology	Orientation to γ-matrix
γ (gamma)	Cubic, A1, Fm3m	$a_0 = 0.36$	4	Matrix	—
γ' (gamma prime)	Cubic, $L1_2$, Fm3m	$a_0 = 0.35$	4	Small Sphere	Cube-on-Cube
G	Cubic, A1, Fm3m	$a_0 = 1.12$	116	Small Rod	Random
Fe_2P	Hex., C_{22}, P_{321}	$a_0 = 0.604$ $c_0 = 0.36$	6	Thin Lath	$(1\bar{2}10)_{ppt}$ // $(011)_\gamma$ $(0001)_{ppt}$ // $(001)_\gamma$
η (eta)	Cubic, $E9_3$, Fd3m	$a_0 = 1.08$	96	Rhombohedral	Cube-on-Cube or Twin
Laves	Hex., C14, $P6_3/mmc$	$a_0 = 0.47$ $c_0 = 0.77$	12	Faulted Lath	Many Variants
$M_{23}C_6$	Cubic, $D8_4$, Fm3m	$a_0 = 1.06$	92	Rhombohedral Platelet	Cube-on-Cube or Twin
MC	Cubic, B1, Fm3m	$a_0 = 0.433$	4	Small Sphere	Cube-on-Cube
σ (sigma)	Tet., $D8_b$, P4/mnm	$a_0 = 0.88$ $c_0 = 0.46$	30	Various	Many Variants
χ (chi)	Cubic, A12, $I\bar{4}3m$	$a_0 = 0.89$	58	Various	Many Variants

Table 7
The principle phases observed in the neutron irradiated 316 and 316 + Ti alloys may be categorized in terms of the preceding discussion as follows [4]:

(a) **γ' (gamma prime) phase**: radiation-induced, enriched in **Ni, Si**. Reversion of this phase during post-irradiation annealing was demonstrated by Brager and Garner [23].

(b) **G phase**: radiation-induced, enriched in **Ni, Si, Ti**, and **Mn**. Reversion of the G phase produced by Ni ion irradiation of 316+Ti was described in the previous section.

(c) **η (eta) phase**: radiation-enhanced, but not modified. Enriched in **Ni** and **Si** as well as **Mo** and **Cr** during thermal aging. Essentially the same composition develops during neutron irradiation.

(d) **$M_{23}C_6$ phase**: neither enhanced or modified. Enriched in **Mo** and **Cr**. Approximately the same compositions occurred in both thermal and irradiation environments.

(e) **Laves phase**: radiation-enhanced and modified. Enriched in **Mo** and **Si** and rejects Ni during thermal aging. During neutron irradiation, **Ni** is accommodated, the proportion of Ni increasing as the irradiation temperature decreases.

(f) **MC phase**: enhanced but not modified. Enriched in **Ti** and **Mo** and rejects Ni in both thermal and radiation environments. May be suppressed under conditions favorable for G phase formation.

(g) **σ (sigma) and Fe_2P phases**: There are presently insufficient data to categorize these phases. There is some evidence that σ phase formation is enhanced by irradiation in HFIR and that Fe_2P phase formation is enhanced and modified by irradiation in EBR-II.

2.8 Summary

A modified-SUS316 cladding tube with 20 % cold work, PNC316 were irradiated by neutron in the experimental reactor JOYO up to 16.0–103 dpa at 502–734 ℃, then investigated mechanical properties and microstructures by means of tensile tests, hardness measurements and transmission electron microscopy (TEM). Through the comparison of the yield strength change, $\Delta\sigma_y$, between experimentally obtained one and estimated one from microstructural observation, followings are summarized:

1. Irradiation softening of yield strength more than 100 MPa measured at irradiation temperature were obtained. On the other hand, for the hardness test, both irradiation hardening and softening were observed after irradiation. Hardening was for irradiation at 502°C, while softening was for irradiation at 709–734°C.

2. Microstructure after irradiation can be specified in the temperature range of –500°C, 550–650°C and 700°C–. The recovery of dislocations and large precipitates like Laves phase, M_6C and/or $M_{23}C_6$ were observed, especially in high temperature irradiation condition.

3. Experimentally-obtained change in mechanical properties and estimated one derived from Orowan's equation were compared. Estimation was in good agreement with hardness data, but not with yield strength data.

4. A possible dependence of the barrier strength of dislocation, α_d, on temperature was suggested through the discussion of the difference between tensile test and hardness test. Further, a possible change of α_d before/after irradiation was suggested. The carbon concentration in matrix may be low after irradiation due to a formation of carbides. The effects of carbon on α_d value in high temperature need to be investigated.

References

[1] G. Lucas, J. Nucl. Mater. 206 (1993) 287.

[2] I. Shibahara, S. Ukai, S. Onose, S. Shikakura, J. Nucl. Mater. 204 (1993) 131.

[3] S. Yamashita, Y. Tachi, N. Akasaka, K. Nishinoiri, H. Takahashi, J. Nucl. Mater. 417 (2011) 953.

[4] E. Lee, P. Maziasz, A. Rowcliffe, *Phase Stability During Irradiation*, The Metallurgical Society of AIME, 1980, pp. 191–218.

[5] E.O. Hall, Proc. Phys. Soc. Sect. B 64 (1951) 747.

[6] N. Petch, J. Iron Steel Inst. 174 (1953) 25.

[7] G.D. Johnson, F.A. Garner, H.R. Brager, R.L. Fish, *Effects of Radiation on Materials*, ASTM STP 725, 1981, pp. 393–412.

[8] G.R. Odette, D. Frey, J. Nucl. Mater. 85-86 (1979) 817.

[9] J.E. Bailey, P.B. Hirsch, Philos. Mag. 5 (1960) 485.

[10] R.. Varin, K.. Kurzydlowski, Mater. Sci. Eng. A 101 (1988) 221.

[11] M.L. Grossbeck, P.J. Maziasz, A.F. Rowcliffe, J. Nucl. Mater. 191-194 (1992) 808.

[12] Stainless Steel Handbook, 3rd ed., Stainless Institute, Nikkankogyo Shinbunsha, 1995, pp. 1432.

[13] G.I. Taylor, J. Inst. Met. 62 (1938) 307.

[14] R. Stoller, S. Zinkle, J. Nucl. Mater. 287 (2000) 349.

[15] J.J. Holmes, R.E. Robbins, J.L. Brimhall, B. Mastel, Acta Metall. 16 (1968) 955.

[16] G.L. Kulcinski, J.L. Brimhall, G.E. Kissinger, Acta Metall. (1972).

[17] F. Garner, M. Hamilton, N.F. Panayotou, G.D. Johnson, J. Nucl. Mater. 104 (1981) 803.

[18] N. Yoshida, J. Nucl. Mater. 174 (1990) 220.

[19] A.L. Bement, Rev. Roum Phys. 17 (1972) 361.

[20] G.I. Taylor, Proc. R. Soc. A Math. Phys. Eng. Sci. 145 (1934) 362.

[21] S. Bruemmer, D. Edwards, E. Simonen, Characterization of Neutron-Irradiated 300-Series Stainless Steels to Assess Mechanisms of Irradiation-Assisted Stress Corrosion Cracking, Final Report, EPRI Project WO4068-20, 2000.

[22] M. Toloczko, G. Lucas, G. Odette, R. Stoller, M. Hamilton, *Effects of Radiation on Materials*, ASTM STP 1270, 1996, pp. 902–918.

[23] H.R. Brager, F.A. Garner, *Effects of Radiation on Structural Materials*, ASTM STP 683, 1979, pp. 207–232.

Chapter 3

Contribution of line dislocation and residual carbon

3.1 Introduction

As described in the previous chapter, the comparison between experimentally-obtained $\Delta\sigma_y$ and estimated $\Delta\sigma_y$ by Orowan's equation in the modified-SUS316 stainless steel after neutron irradiation suggested that the barrier strength of line dislocations, α_d, could depend on temperature and change before/after irradiation as a result of the reduction of carbon content in the matrix due to precipitation of carbides. The effects of carbon on α_d value need to be investigated. In this chapter, model alloys (Fe–16Cr–14Ni–2.5Mo) with two different carbon concentration level were cold-worked to various levels, then the measurement of dislocation density and tensile test at 25 and 700°C were performed understand details of temperature effect and a role of carbon atoms on the barrier strength of line dislocations, α_d.

3.2 Objective of this chapter

1. Detailed investigation of temperature dependence of the barrier strength of line dislocations, α_d
2. Effects of residual carbon content on the barrier strength of line dislocations, α_d

3.3 Experimental

3.3.1 Fabrication of model alloy

Fe–16Cr–14Ni–2.5Mo model alloys used in this study were produced by arc-melting from the stating material; Pure iron provided by Johnson Matthey Chemicals; Pure chromium (4N5) provided by Japan Metals & Chemicals Co., Ltd.; Pure nickel (4N7) provided by Johnson Matthey Chemicals; Pure molybdenum (3N) provided by RARE METALLIC Co., Ltd. The chemical compositions of the starting materials are provided in Tables 1–2. To provide the difference of carbon concentration, cementite

powder was added for one alloy. In the following, high carbon alloy denotes the alloy with cementite while low carbon alloy denotes the one without cementite.

Table 1

Chemical composition (wppm) of pure Fe used in this study provided by Johnson Matthey Chemicals.

Mg	Ca	Cr	Cu	Mn	Si	C	H	O	N
7	1	1	1	1	1	35	1.6	34	190

Table 2

Chemical composition (wppm) of 4N5 Cr used in this study provided by Japan Metals & Chemicals Co., Ltd.

Fe	Si	Al	O	N	C	S	Cu	P	Pb
<0.05	0.02	0.01	630	10	<10	23	<0.05	0.03	0.29

Accurately-weighed starting materials were arc-melted into 15g button ingots under 5.2×10^{-2} Pa vacuum condition. For the high carbon alloy, the cementite powder were wrapped in cold-rolled pure-Fe plate to prevent an expected fly-off during arc-melting. The alloy buttons were first forged at 1073 K into a rod shape (Fig. 1) then homogenized at 1173 K for 24 h. Oxide layer was removed completely by a flat file after forging or homogenizing. The buttons were then cold rolled and cut into 70-mm-length, 5-mm-width, and 0.3-mm-thick sheets, like “ribbons” (Fig. 2). Eventually eleven of ribbons for each alloys were prepared. The ribbons were capsulated into quarts tubes (2 ribbons / tube) at about 4.0×10^{-4} Pa, and then solution-annealed at 1353 K for 20 min following air cooling.

In order to introduce dislocation structure, uniaxial pre-straining for the ribbon samples were carried out by using tensile test machine (Instron Series 5560 Load Frames) with wedge grips. Strain-controlled operation at room temperature were conducted with a strain rate of 1×10^{-3} s^{-1}, which corresponds to the crosshead speed of 0.055 $mm\cdot s^{-1}$ (a gauge length of ribbon sample: 55mm). The pre-straining was conducted up to the

resultant plastic strain of 0, 2.5, 5.0, 7.5 and 10%, then unloaded immediately (Fig. 3). Then sub-sized sheet tensile specimens with a 5mm long by 1.2mm wide gauge section and disk-shaped specimens with a diameter of 3 mm were precision punched from the ribbons (Fig. 4). The punched-out sheet tensile samples were then mechanically ground with lastly ♯1000 polish paper to remove shear burrs. Schematics of above preparation flow was shown in Fig. 5.

Quantitative analysis of chemical composition of the fabricated model alloy were done for the punch-outed alloy scrap, conducted by Nikko Inspection service Co., LTD. An infrared absorption method after combustion in a high-frequency induction furnace for carbon measurement, an absorption spectrophotometry for silicon measurement, an inductively coupled plasma atomic emission spectrometry for nickel, chromium and molybdenum measurement and an inert gas transportation fusion-thermal conductivity method for nitrogen measurement were used. The resultant chemical composition was shown in Table 3.

Fig. 1 Rod-shaped alloy button after forging at 1073K.

Fig. 2 Ribbons with 70-mm-length, 5-mm-width and 0.3-mm-thick.

Fig. 3 Pre-strained ribbon up to 10 % engineering strain.

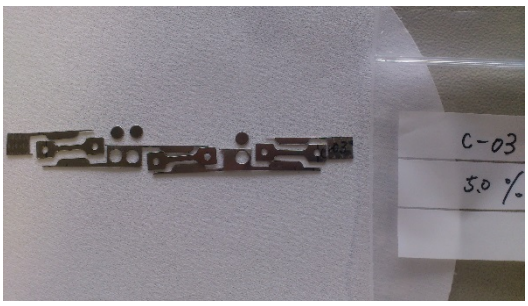

Fig. 4 Sub-sized sheet tensile specimens and TEM disks punched out from ribbon.

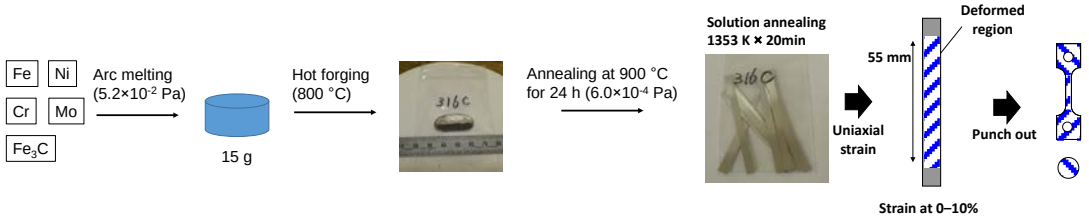

Fig. 5 Schematics of preparation flow of model alloy.

Table 3
Chemical composition (wt%) of model alloys.

Material	Fe	Cr	Ni	Mo	Si	C (wppm)	N (wppm)
High carbon alloy	Bal.	15.93	13.86	2.52	0.01	225	106
Low carbon alloy	Bal.	15.92	13.85	2.51	0.01	19	132

3.3.2 Tensile test

Tensile tests with the sheet tensile samples at room temperature were carried out in the Instron machine, while elevated temperature tests at 973K were carried out in the Shimadzu Servopulser, equipped with a high-temperature furnace capable of maintaining the temperature constant within ±3K, in an Argon gas flow. The applied strain rate was in all cases 1×10^{-3} s^{-1}. Since the yield points cannot apparently be obtained, tensile yield strengths were read at 0.2% strain offset. Two or more tests were carried out for each alloy-strain-temperature condition.

3.3.3 Measurement of dislocation density in TEM

Thin foils for transmission electron microscopy observation were prepared using a standard twin-jet electro-polishing technique (TENUPOL device) in an electrolyte (95 vol.% acetic acid, 5 vol.% perchloric acid) at 14 °C and 60 V. TEM observations were conducted on a JEOL2010, LaB6, high tilt lens, operated at 200 kV. The observation

conditions are those typical for austenitic stainless steels, with **g** = {200} as diffraction vector, **B** = <110> as beam direction and **g**(5**g**) as diffraction condition for weak-beam observations.

Measurement of dislocation density was done in the manner of Keh's formula [1] [2];

$$\rho = \left(\frac{n_1}{L_1} + \frac{n_2}{L_2} \right) \frac{1}{t} \qquad (1)$$

where ρ, n_1, n_2, L_1, L_2, and t are dislocation density (m^{-2}), number of cross point with vertical line, number of cross point with horizontal line, total length of vertical line (m), total length of horizontal line (m), and thickness of thin foil (m). Fig 6 shows the schematics of measurement procedure of dislocation density. First strain contrasts derived from dislocation in WBDF images were picked by eye and hand on the screen monitor into monochrome image (see Fig. 6) then dislocation density was measured.

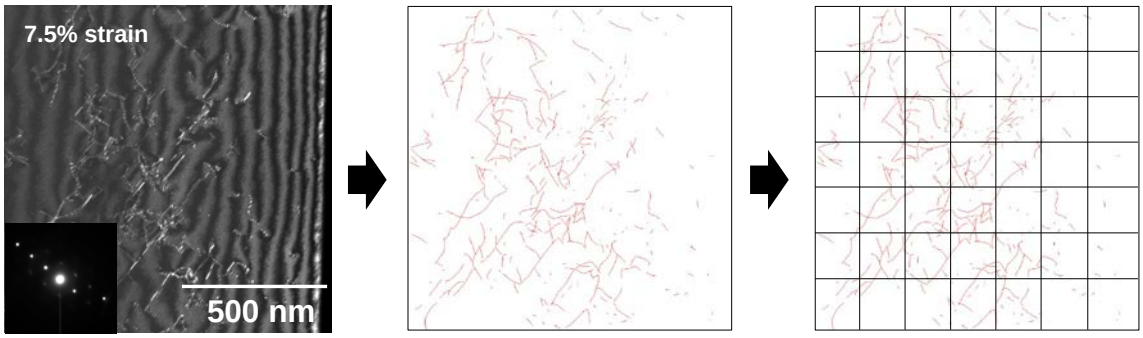

Fig. 6 Schematics of measurement procedure of dislocation density.

3.3.4 Uncertainty of slope and intercept

Uncertainty of slope and intercept is considered in the manner of least-square regression and error propagation according to ref [3]. Details are summarized in Appendix B.

3.4 Results

3.4.1 Stress-strain curves during pre-straining

Fig. 8 shows the typical engineering stress-strain curve of model alloys during pre-straining. The strength of high carbon alloy was higher than that of low carbon alloy over the entire range of strain. Although the stress-strain curves of all samples are not shown in Fig. 8, the deviation of the tensile behavior in stress-strain curves was relatively small. Of interest is that for high carbon alloy the yield drop and dragging motion around yield point were observed.

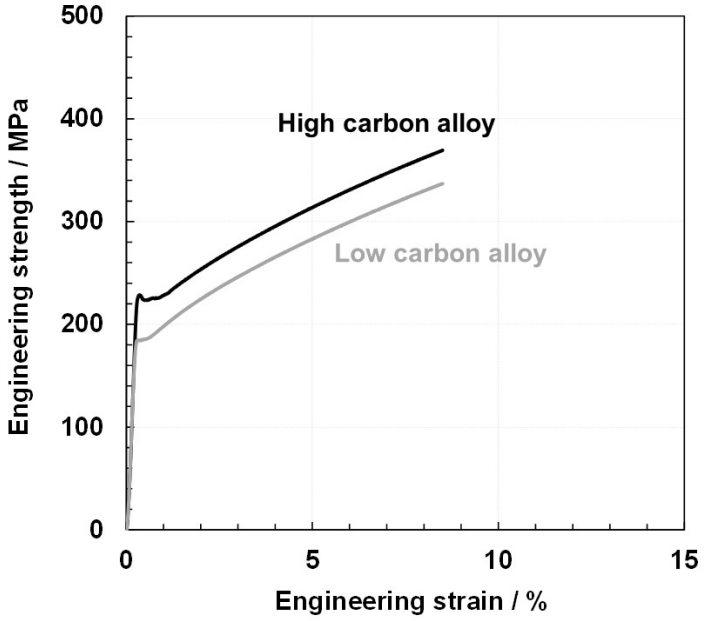

Fig. 8 Typical engineering stress-strain curve of model alloys during pre-straining at room temperature.

3.4.2 Dislocation structure

When the dislocation is introduced by cold rolling, the distribution of dislocations is considered to be non-uniform perpendicular to the rolling direction of the sample. In this study, since the pre-straining was done by uniaxial straining, the introduced dislocation structure should be uniform in the sample. Figs. 9 shows the typical dislocation structures of high carbon alloy deformed to 0, 2.5, 5.0, and 7.5 % strain. It is clearly seen that the dislocation density increase with increasing specimen thickness. Dislocation density were measured from these weak-beam dark-field images. Fig. 10 shows the measured dislocation density as a function of deformation ratio. The error bar shown in fig. 10 denotes standard deviation. It is clearly seen in Fig. 10 that dislocation density in both low carbon alloy and high carbon alloy is similar.

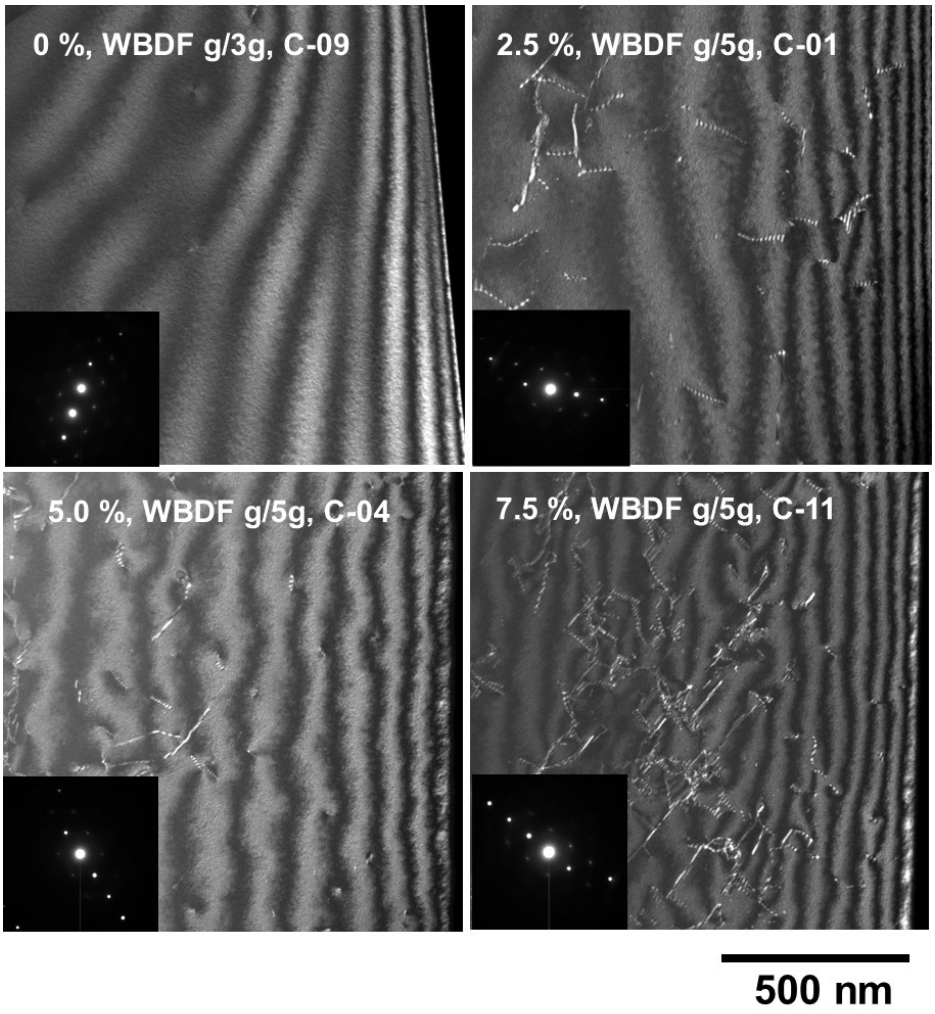

Fig. 9 Weak-beam dark-field images of high carbon alloy deformed to 0, 2.5, 5.0, and 7.5 % engineering strain.

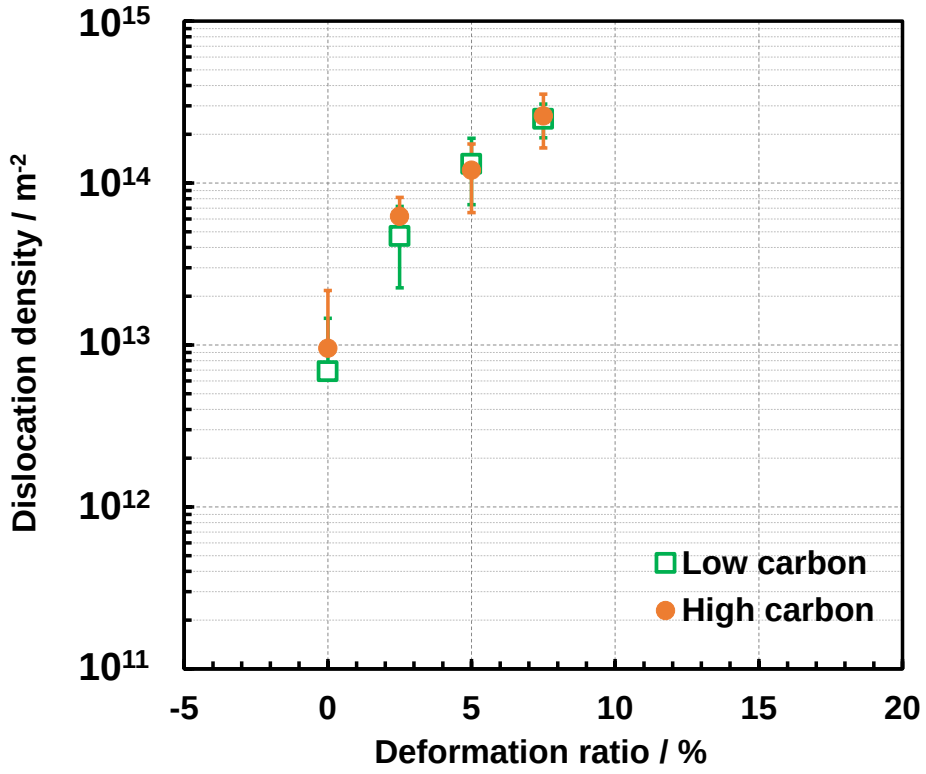

Fig. 10 Measured dislocation density as a function of pre-deformation ratio.

3.4.3 Yield strength

Fig. 11 shows yield strength of both low carbon alloy and high carbon alloy tested at 25 and 700°C as a function of square root of dislocation density. In the test temperature at 25°C, the high carbon alloy is stronger than the low carbon alloy in any density of dislocation. At 700°C, the alloys showed a similar tendency in the strength. For both alloy, the relationship between the total dislocation density ρ_d and yield strength σ_y is in accordance with the Bailey-Hirsch relationship, described as

$$\sigma_y = \sigma_0 + M\alpha_d \mu b(\rho_d)^{1/2}, \quad (2)$$

where σ_0, M, α_d, μ, and b are a constant, the Taylor factor, the barrier strength of forest dislocations, the shear modulus of the matrix, and the Burger's vector of moving dislocation, respectively. Here, the strength factor, α_d, for forest dislocation can be derived from the slope in Fig. 11.

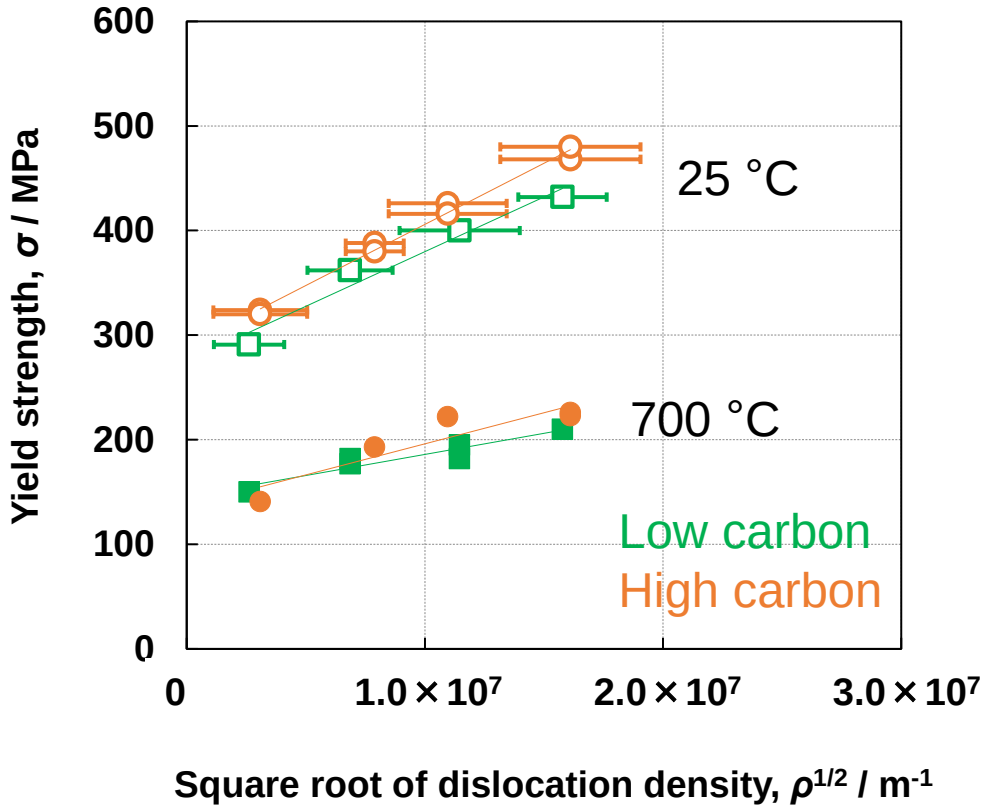

Fig. 11 Yield strength of both low carbon alloy and high carbon alloy tested at 25 and 700°C as a function of square root of dislocation density.

3.5 Discussion

3.5.1 Effect of carbon concentration and test temperature on strength factor of line dislocations, α_d

Fig 12 shows a temperature dependence of α_d value in low carbon alloy (19wppm C), high carbon alloy (225wppm C) and PNC316SA (500wppm C). In PNC316SA (500wppm C) sample, no temperature dependence of α_d value was found while α_d value decrease with increasing temperature in low carbon alloy (19wppm C), to the value of about 0.1, which is almost half of that in PNC316SA (500wppm C) sample. From Fig. 12, following things can be stated as a summary that; “strength of the forest dislocation” in high carbon alloy is bigger than that in low carbon alloy at 700°C.

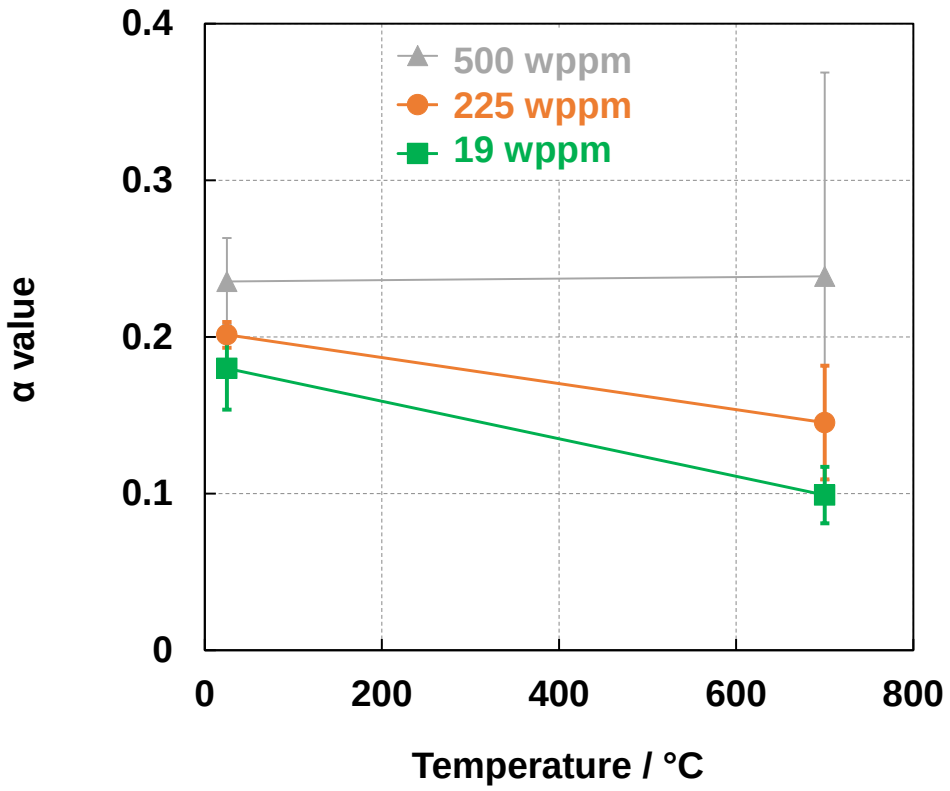

Fig. 12 Temperature dependence of strength factor of forest dislocation, α_d as a function of temperature.

3.5.2 Discussion of the effect of carbon concentration and test temperature on strength factor of forest dislocation, α_d

The following mechanism of temperature dependence of strength factor, α_d, can be suggested. Dislocation in this FCC model alloy are mostly considered to be extended (Fig. 13). Considering the cutting of extended dislocation to extended dislocation, constriction of extended dislocation is necessary (Fig. 14). The energy which is necessary for constriction can be explain as:

$$U\mathrm{c} = \frac{\mu b^2 w_\mathrm{s}}{15}\left(\ln\frac{w_\mathrm{s}}{b}\right)^{1/2}$$

where w_s is the distance of extended dislocation [4]. As a forest dislocation, edge component of the partial dislocation was locked by carbon atmosphere (Fig.15) due to the stress relaxation by interstitial type carbon atoms, similar to Cottrell effect [5]. Much more stress need to be apply to be able to constrict. Thermally-activated process can assist the constriction in high temperature test.

Extended dislocation

$$\underset{\mathbf{b}_1}{\frac{a}{2}[\bar{1}01]} \rightarrow \underset{\mathbf{b}_2}{\frac{a}{6}[\bar{1}\,\bar{1}2]} + \underset{\mathbf{b}_3}{\frac{a}{6}[\bar{2}11]}$$

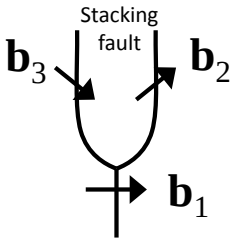

Fig. 13 Schematics of extended dislocation in FCC material.

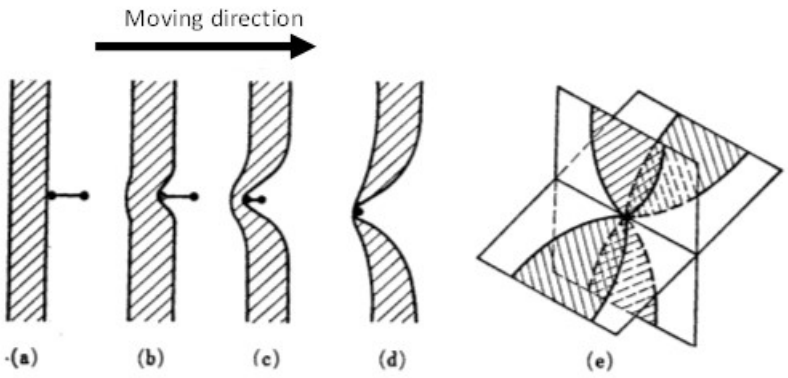

Fig. 14 Schematics of Crosscutting of extended dislocation (Schoeck and Seeger, 1955 [11]).

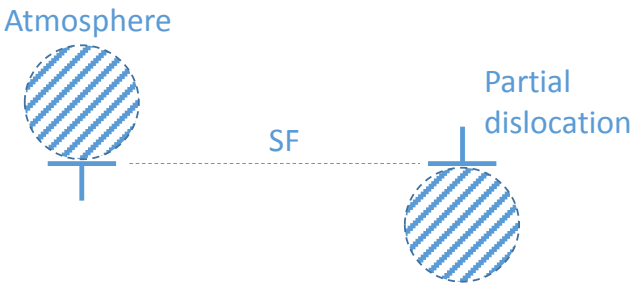

Fig. 15 Schematic showing atmosphere around extended dislocation.

Another possible mechanism to explain could be the one similar to chemical interaction or Suzuki effect [6] [7]. When dislocation is extended, chemical potential of solute atoms locating in stacking fault is different from that in the matrix. Thus the concentration of solute atoms locating in stacking fault is different from that in the matrix, as well. Stacking fault energy (SFE) γ_s can vary depending on solute atom concentration. Here the empirical equations predicting SFE from the concentration of solute atoms (wt%) are presented [8] [9] [10]:

$$\text{SFE } (\text{mJ/m}^2) = 25.7 + 2(\text{Ni}) + 410(\text{C}) - 0.9(\text{Cr}) - 77(\text{N}) - 13(\text{Si}) - 1.2(\text{Mn}) \quad [8],$$

$$\text{SFE } (\text{mJ/m}^2) = -53 + 6.2(\text{Ni}) + 0.7(\text{Cr}) + 3.2(\text{Mn}) + 9.3(\text{Mo}) \quad [9], \text{ and}$$

$$\text{SFE } (\text{mJ/m}^2) = 1.2 + 1.4(\text{Ni}) + 0.6(\text{Cr}) + 17.7(\text{Mn}) - 44.7(\text{Si}) \quad [10].$$

The first one shows the dependence of carbon atom concentration on SFE, while the other two do not show. If the extended dislocation move across the area with different solute atom concentration, change of SFE could be a resisting force. When the solute atom concentration in the matrix and the stacking fault is expressed in c_0 and c_1, respectively, the resisting force would be

$$\tau = \{\gamma_s(c_0) - \gamma_s(c_1)\} / b$$

where b is the Burger's vector of perfect dislocation. Fig. 16 is the schematic of procedure showing extended dislocation depinning from atmosphere derived from chemical interaction. This mechanism can explain the lock of moving extended-dislocations. However, this may also apply to when considering the constriction of forest extended-dislocations.

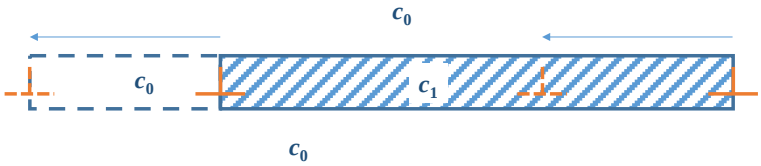

Fig. 16 Schematic of procedure showing extended dislocation depinning from atmosphere, which is derived from chemical interaction. Solute atom concentration in the matrix and the stacking fault is expressed in c_0 and c_1, respectively.

3.6 Summary

The barrier strength of line dislocations, α_d, was investigated for model austenitic alloys with different carbon concentration at elevated temperature, leading to the conclusion below.

1. α_d in a low carbon content alloy depended on test temperature, while that in 500wppmC alloy do not. This means that, at high temperature, the “strength” of forest dislocations in the low carbon alloy was weak compared with that in high carbon alloy. Due to the locking of partial dislocation by carbon atoms, the constriction of extended dislocation is hard to occur.

2. This fact, i.e. dependence of α_d on test temperature in low carbon alloy, suggested that α_d may decrease in type 316 stainless steel after long-term irradiation at high temperature due to the depletion of carbon atoms in the matrix.

References

[1] A.S. Keh, Direct observations of Imperfections in Crystals, Interscience (1961) 213

[2] L.I. Van Torne, G. Thomas, Acta Met., 11(1963) 881.

[3] John R. Taylor, *An Introduction to Error Analysis*, 2nd Ed., University Science Books.

[4] A.N. Stroh, Proceedings of the Physical Society, Section B 67 (1954) 427.

[5] A.H. Cottrell, B.A. Bilby, Proc. Phys. Soc. (London), A62 (1949) 49.

[6] H. Suzuki, Sci. Rep. RITU, A4 (1952) 455.

[7] H. Suzuki, J. Phys. Soc. Japan, 17 (1962) 322.

[8] F.B. Pickering, Proceedings of the Conference on Stainless Steels 84, Gothenberg, Sweden, 1984, The Institute of Metals, London, 1985, p.2–28.

[9] R.E. Schramm, R.P. Reed, Metall. Trans. 6A (1975) 1345.

[10] C.G. Rhodes, A.W. Thompson, Metal. Trans. 8A (1977) 1901.

[11] A. Seeger, Phil. Mag. 46 (1955) 1194.

Chapter 4

Contribution of irradiation-induced dislocation loops

4.1 Introduction

In this chapter, dislocation loop induced by irradiation were considered as obstacles to dislocation glide. The contribution of the dislocation loops to mechanical properties, i.e. the barrier strength of dislocation loops, α_l, was investigated by using ion-irradiation and nano-indentation technique.

Nano-indentation technique has been used to evaluate the irradiation hardening in ion-irradiated materials for simulating the change of mechanical properties under fission and fusion reactor conditions. The available irradiated volume by ion irradiation, however, is small and limited from the specimen surface. Additionally there is a damage gradient in the ion-irradiated volume. These features provide many scientific and technical challenges such as a hardness depth profile, a softer substrate effect and an indentation size effect [1]. To utilize the hardness data of ion-irradiated material obtained by nano-indentation for engineering aspect, an analyzing method needs to be developed further.

In the past studies, nano-indentation technique for irradiated materials have been performed to evaluate the irradiation-induced hardening, not softening. Irradiation-induced hardening is the result of evolution of a damage microstructure, namely dislocation loops. In austenitic stainless steel, the dislocation loops are formed by irradiation at around 300°C. Ion irradiation is one of the method to introduce the dislocation loops into materials.

4.2 Objective of this chapter

To evaluate the barrier strength of dislocation loops, α_l, an attempt to obtain the depth dependence of the hardness in ion-irradiated material was done by means of nano-indentation combined with sectioning. The framework of this chapter is as below.

1. Investigation of the relationship between the penetration depth of an indent and the range of deformed zone induced by means of transmission electron microscopy

(TEM).

2. Evaluation of “local hardness” in the ion-irradiated region based on the “multi-layer model”, which is the combination of nano-indentation technique and sectioning.

3. Determination of the barrier strength of dislocation loops, α_l, by comparing the local hardness and the neutron-irradiation data.

4.3 Experimental

A 316 stainless steel solution-annealed at 1473 K for 15 min was used in this study. The size of the specimen was 1 mm thickness, 6 mm length and 3 mm width. Prior to irradiation, the specimen was mechanically polished using alumina suspension with a grain size of 0.3 mm. To remove any deformation layer produced during mechanical polishing, the sample surface was also electro-polished.

Ion irradiation was carried out at the TIARA facility of JAEA with 10.5 MeV Fe^{3+} ions at the temperature of 523 K. The nominal displacement damage was up to 0.1–10 dpa at the depth of 1 μm from the specimen surface. The displacement damage reached to 2.5 μm depth and a peak of damage was at 2.1 μm depth based on SRIM calculation [2].

Nano-indentation test was carried out by using an Elionix ENT-1100a with a triangular pyramidal diamond indentor (Berkovich type tip). To gain the hardness depth profile of the sample, depth control measurements was performed with a penetration depth of 50–800 nm with 10 nm interval. Average hardness from 3 indentations were obtained at each penetration depth. Therefore, one hardness depth profile in this study consist information of more than 225 indents. To avoid overlapping of the plastically deformed zones, the indents were performed at intervals of 30 μm.

TEM investigations were performed to evaluate the range of the plastically deformed zone. For this purpose, cross-sectional TEM samples through an indent were prepared by using focused ion beam (FIB) machine (JEOL JIB-4600F). To protect the

imprints against Ga^+ ion damage, the indentations were covered by carbon deposition layer. Before depositing the protection layer, the center of the indentation was marked to get the cross section right through the middle of the indent.

The damage layer was sectioned to the depth of 0.6, 1.2, and 1.8 μm from the specimen surface by using FIB machine. Ga^+ beam of FIB was bombarded parallel to the specimen surface. The size of the sectioned area was about 40 × 100 μm^2. Nano-indentation was carried out to "new surface" produced by the sectioning. Because of the size of the sectioned area, the distances between each of the imprint was 10 times penetration depth for each indentation.

4.4 Hardness depth profile and deformation zone in ion-irradiated region

Fig. 1 shows the plots of inverse depth versus square of hardness obtained from nano-indentation tests. The inverse depth versus square of hardness relationship showed an inflection for the irradiated materials. Note that the hardness determined in the manner outlined by Oliver and Pharr [3] in Fig. 1 and 5. The possible effect of softer substrate region beyond the irradiated region was discussed within the framework of the studies by Nix and Gao [4] and Kasada et al. [1]. Kasada et al. [1] showed that the Nix-Gao plots of ion-irradiated material has an inflection at a critical indentation depth, h_c, and a contribution of bottom softer substrate region in the sample beneath the indent reflects to the hardness when the penetrate depth is deeper than h_c. In the Fig. 1, h_c appeared to depend on the irradiation dose, and were obtained to be 330 μm for 0.1 dpa sample, and 440 μm for 1.0 and 10 dpa sample.

Cross-sectional TEM were performed to observe the plastically deformed zone which was induced by an indent. Figs. 2a–d show the experimentally observed deformation zone of the unirradiated sample and the irradiated sample up to 10 dpa with indentation depth of h_c. For unirradiated sample (Fig. 2a), the plastic deformation (mainly the dislocation structure), introduced by the indent with penetration depth of 400 nm,

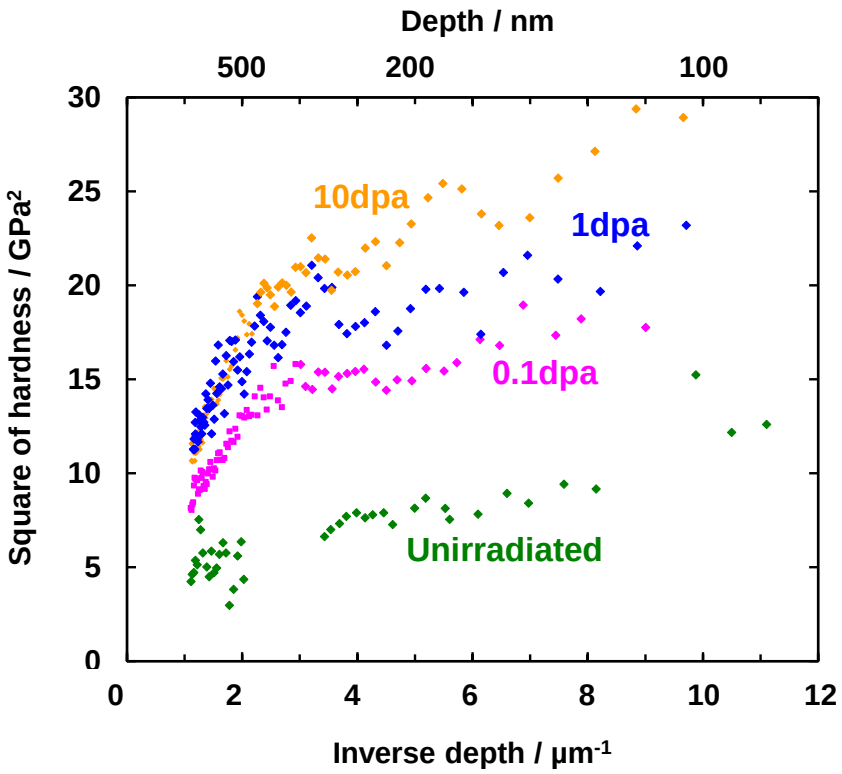

Fig. 1 Inverse depth-square of hardness plot of the samples irradiated up to 0, 0.1, 1, and 10 dpa at 523 K.

reached to 3.0 μm from the specimen surface. Note that the observed black dots in Fig. 2 are artifacts induced by Ga^{+} ion beam. For figs 2b–d, prior to mention about the deformation zone, the distribution of defect cluster introduced by Fe^{3+} ion irradiation must be mentioned. As seen in Figs. 2b–d, the defect cluster were distributed in the region from the surface to 2.5 μm depth. Especially the 10 dpa sample clearly exhibited the defect cluster distribution and the area with the maximum number density of the defect cluster appeared to be at 2.3 μm depth. The plastically deformed zone produced by the indent where the indentation depth is h_c was examined with respect to its range in irradiated samples. In Fig. 2b–d, the deformed zone appeared to be reached to the peak damage region in each sample, especially in the left hand side of the deformed region (cross-section through the face of the indentation). On the other hand, the deformation zone was not exhibited in the region deeper than the peak damage region. This means that, in the irradiated sample, the deformation zone introduced by the indent where the penetration depth is h_c spreads right from the surface to the damage region. This important results were taken into account in the sectioning experiment as mentioned below.

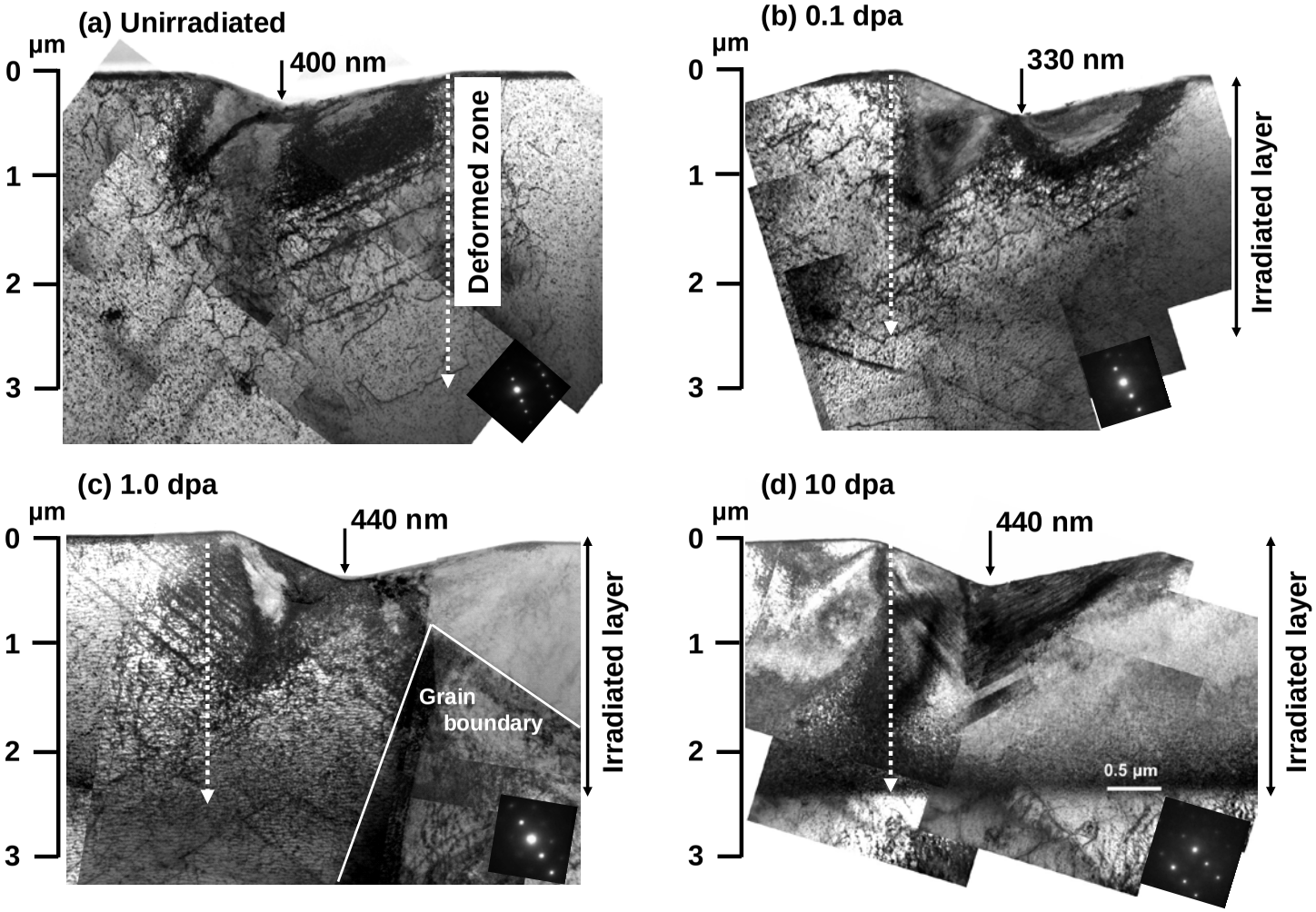

Fig. 2 Deformation zone of (a) the unirradiated sample and the irradiated sample up to (b) 0.1, (c) 1.0, and (d) 10 dpa with indentation depth of h_c.

4.5 Multi-layer model and the results of sectioning experiment

Here, the concept of multi-layer model is as follows:

The irradiated layer, which is the region from the specimen surface to 2.5 μm depth in this study, can be divided into sub-layers. Additionally, each sub-layer has their own local hardness, H_L, according to the damage distribution. Fig. 3 shows the schematic of the sub-layer and the H_L. It also shows the displacement damage profile, which was obtained by using SRIM code [2]. In this study, four sub-layers were considered. Here the hardness of whole irradiated layer, H, measured by one indent was assumed to be the product of volume fraction of a deformation zone, f, and local hardness, H_L in each sub-layer, respectively. Namely, H can be described as

$$H = \Sigma f_i H_{Li} \qquad (1)$$

with the assumption of a deformed zone to be a hemisphere. According to eq.1, each of H can be described as

$$H_0 = f_1 \cdot H_{L1} + f_2 \cdot H_{L2} + f_3 \cdot H_{L3} + f_4 \cdot H_{L4}, \qquad (2)$$

$$H_{0.6} = f_2' \cdot H_{L2} + f_3' \cdot H_{L3} + f_4' \cdot H_{L4}, \qquad (3)$$

$$H_{1.2} = f_3'' \cdot H_{L3} + f_4'' \cdot H_{L4}, \qquad (4)$$

$$H_{1.8} = H_{L4} \qquad (5)$$

where the index of H is the sectioning depth from the specimen surface. Fig. 4 is the schematics showing the sectioning procedure and the measurement of H in each sectioning distance. Note that f_3 and f_3', for instance, was different because the radius of the deformation zone can be different in every single H measurement. After measuring H by nano-indentation technique, we experimentally evaluated the local hardness H_L of each layer by solving the equations (2)–(5).

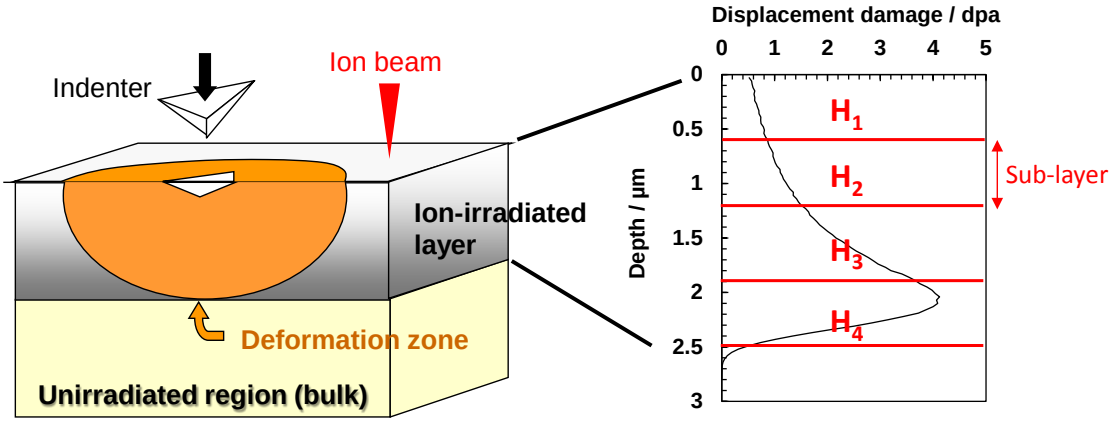

Fig. 3 Schematic of the deformation zone by nano-indentation in ion-irradiated sample. The irradiated layer can be divided into sub-layers which have their own hardness H_L. In the right-hand side, the damage distribution and corresponding sub-layers are shown.

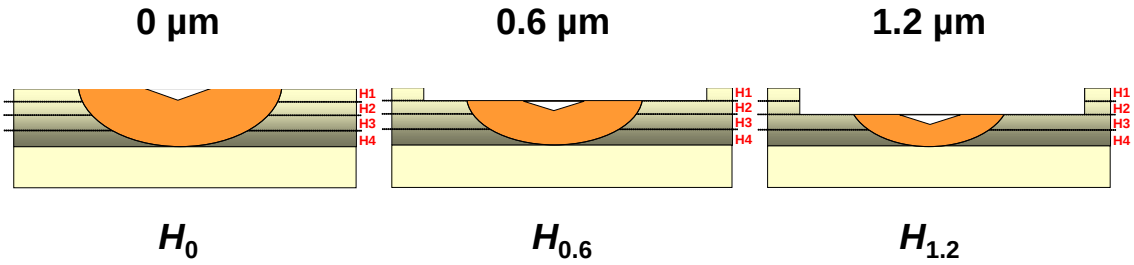

Fig. 4 Schematics showing the sectioning procedure and the measurement of H in each sectioning distance.

The sectioning was carried out to the sample with the nominal displacement damage of 1 dpa. Nano-indentation were carried out to the “new surface” produced by sectioning in order to obtain the Nix-Gao plot and h_c. It resulted that h_c for the sectioning distance of 0.6, 1.2, and 1.8 μm was 210, 230, and 190 nm, respectively, as-shown in Fig.5. Here the values of h_c was rounded off to one digit as considering the errors of h_c. As mentioned in section 3.1, the deformation zone where the penetration depth is h_c reaches to the bottom of the damage region. So the radius of deformation zone was assumed to be the distance from the new surface to the bottom of damage region.

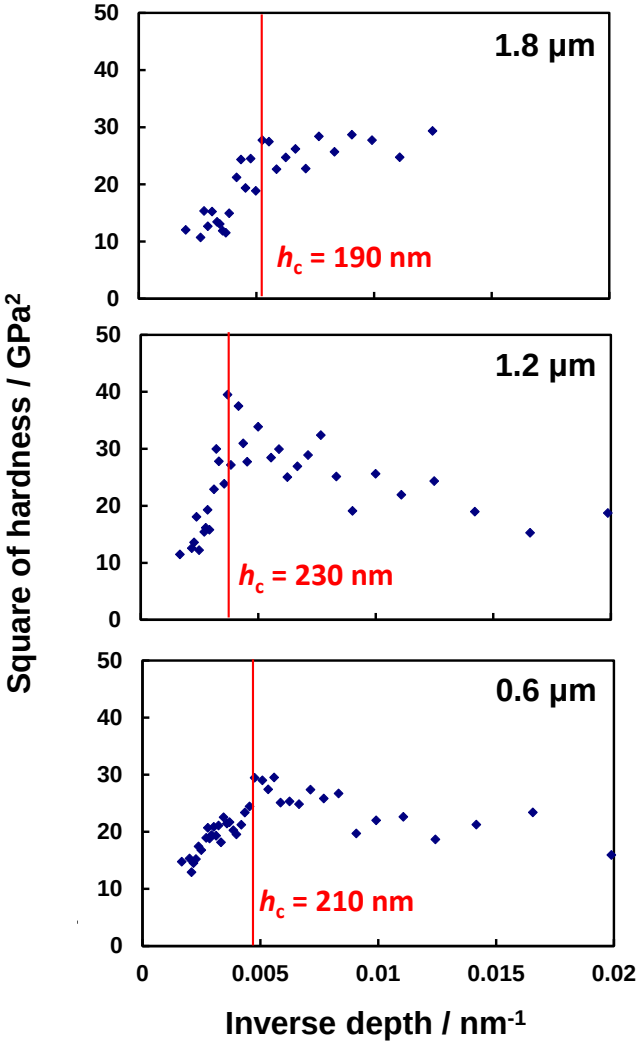

Fig. 5 Nix-Gao-plots and corresponding h_c for the sectioning distance of 0.6, 1.2, and 1.8 μm.

H was obtained as bellow. According to the work of Inamura and Suzuki [5], the obtained load-displacement profile by nano-indentation technique can be assumed to be

$$F \approx Ah + Bh^2 \qquad (6)$$

where F is the indentation load, h is the indentation depth and A and B are constant. The term of Ah represents the elastic deformation in the very early stage of an indentation due to the roundness of the tip, where F is proportional to h. The term of Bh^2 represents the plastic deformation where F is proportional to the contact area of the tip. Because the contact area is proportional to h^2, F is proportional to h^2. Furthermore, they revealed that the slope of *F/h-h* plot, B, was good correlation with Vichers hardness as;

$$B \approx 0.287\ Hv \qquad (7)$$

where B in GPa and Hv in kg mm^{-2}. In this study, the load-displacement profile where the indentation depth is h_c for each sectioning distance was analyzed to obtain B. Then H was evaluated using eq. (7). Fig. 6 shows the *F/h-h* profile where the indentation depth is h_c for the sectioning distance of 0, 0.6, 1.2, and 1.8 μm. The evaluated B and H were summarized in Table 1. Eventually, by solving eq. (2)–(5), the local hardness, H_L, was experimentally evaluated such that H_{L1}, H_{L2}, H_{L3}, and H_{L4} are 178, 288, 353, and 408, respectively. Fig. 7 shows the resulted H_L and the displacement damage profile as a function of depth. H_L increased with increasing depth, and it appeared to be good correlation to the damage profile.

Table 1

B parameter derived from the *F/h-h* profile (Fig. 6) and corresponding *H*.

Sectioning distance / μm	Critical indentation depth, h_c / nm	Number of an indent	B / GPa	H / kg mm^{-2}
0	440	5	79.8	H_0 = 278
0.6	210	3	95.6	$H_{0.6}$ = 333
1.2	230	2	106.8	$H_{1.2}$ = 372
1.8	190	2	117.1	$H_{1.8}$ = 408

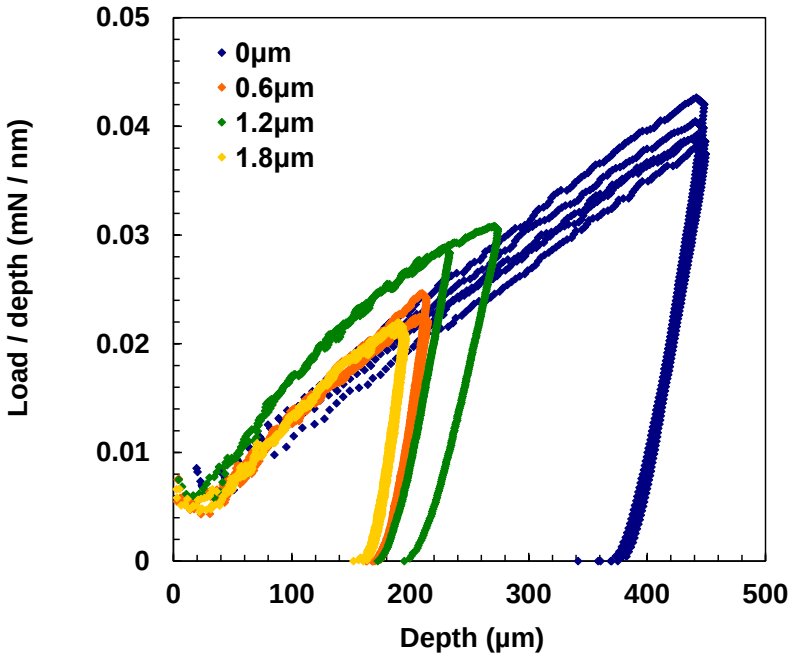

Fig. 6 *F/h-h* profile where the indentation depth is h_c for the sectioning distance of 0, 0.6, 1.2, and 1.8 μm.

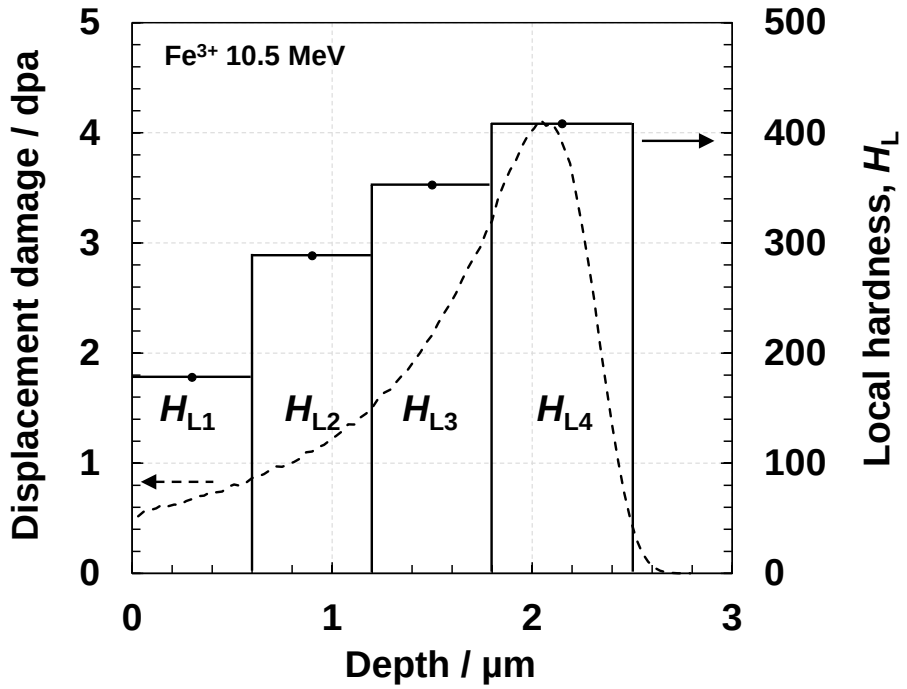

Fig. 7 Resulted H_L and the displacement damage profile as a function of depth.

4.6 Validity of multi-layer model

To confirm the validity of the obtained H_L, the irradiation hardening, $\Delta H = H_L - H_{unirr.}$, was plotted as a function of dose in Fig. 8. Note that $H_{unirr.}$ is the hardness of unirradiated material obtained through eq. (6) and (7), to be 184 in this study. The value of $H_{L1}-H_{unirr.}$ became minus so it was neglected in Fig. 8. The irradiation hardening in this study showed power law as a function of dose with n of 0.6. On the other hand, compared to the work of Okada et al. in 1996 [6], they showed the power law with n = 0.20 in irradiation hardening of an austenitic stainless steel (Fe-15Cr-16Ni) irradiated in RTNS-II and JMTR at 473 K. Here it should be noted that horizontal axis of Fig. 1 in the work of Okada et al. [6] indicated DEPA eV·atom^{-1}. Even so, the power index obtained in this study was large compared to that obtained in neutron irradiation experiment. This difference might be due to the overestimation of hardness at peak damage area. As seen in Fig. 6, the loading profile corresponding to the sectioning distance of 1.2 μm showed a concave downward. This might be due to the steep increase of the displacement damage between 1.2 and 1.8 μm of the original depth (Fig. 3), which leads to the damage gradient effect on the hardness. This damage gradient effect might cause an overestimation of hardness.

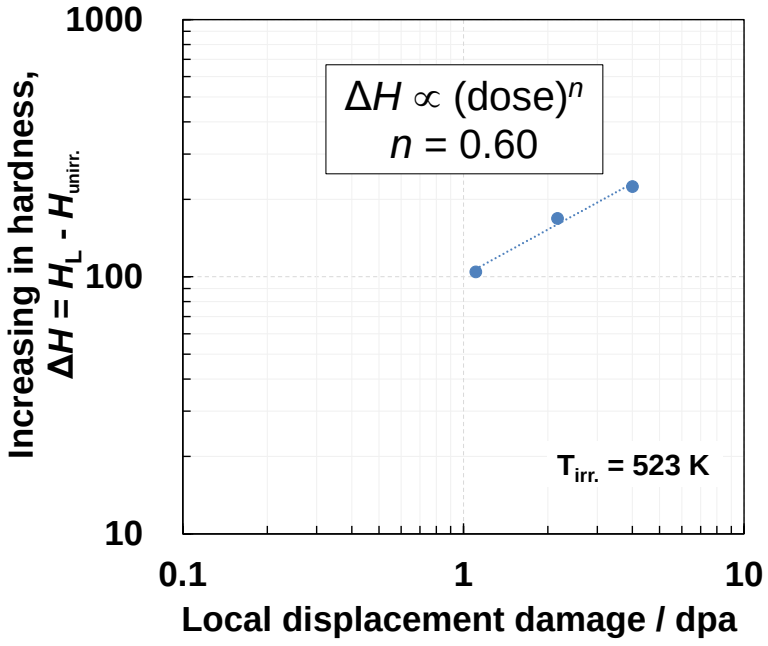

Fig. 8 Log-log plot of irradiation hardening, $\Delta H = H_L - H_{unirr.}$ as a function of dose.

On the other hand, the validity of the multi-layer model should be discussed. In this study, the hardness was simply assumed to be the product of volume fraction of a deformation zone and the local hardness. Furthermore, the deformation zone was assumed to be a simple hemisphere. Although H_L obtained reasonably as a function of depth, the multi-layer model should be improved further.

The difference in the power index between this study and neutron irradiation should be also discussed in terms of microstructural aspect. In the case that number density of the defect clusters produced by ion-irradiation increase linearly and its size is constant as a function of dose, the power index should be close to 0.5 which is explained by Orowan's equation. Furthermore, an appropriateness of the power-law discussion should be considered. In type 316 stainless steel, irradiation hardening achieves the saturation level by neutron irradiation up to almost 1dpa [7]. Most of the case for the power-law discussion on irradiation hardening is about the dose ranging from 0.001 to 1dpa [8-12]. This range of dose is narrow compared with that in this study. Besides, these work was based on tensile test measurement, especially yield strength [13] tested at irradiation temperature, not on hardness test measurement. These two method detect completely different properties of material. While yield stresses are measured at approximately 0.2% strain, hardness measurements represent material properties at much higher strains, 8% as estimated by Tabor [14]. One assesses the starting of plastic deformation and the other do the highly deformed state.

Here, Kodama et al. [15] investigated a series of Type 304, 304L, and 21 heats of Type 316 and 347 stainless steels irradiated in a boiling water reactor to $1.7–2.2\times10^{25}$ n/m^2 (E > 1MeV) and $3.3–4.0\times10^{25}$ n/m^2 (E > 1MeV), corresponding to 2.9 and 5.0dpa. The data set of hardness which performed at room temperature is listed in ref. [15], so we can obtain a change in hardness, shown in Fig. 9. The irradiation temperature done by Kodama et al. is at 288℃ (561K) which relevant to LWR core materials, so it is comparable to the data of this study. As shown in Fig. 9, though the data set exhibits significant scatter which could be the result of the large number of alloys (23) studied, the data trend of this study is very much close to that of Kodama et al.

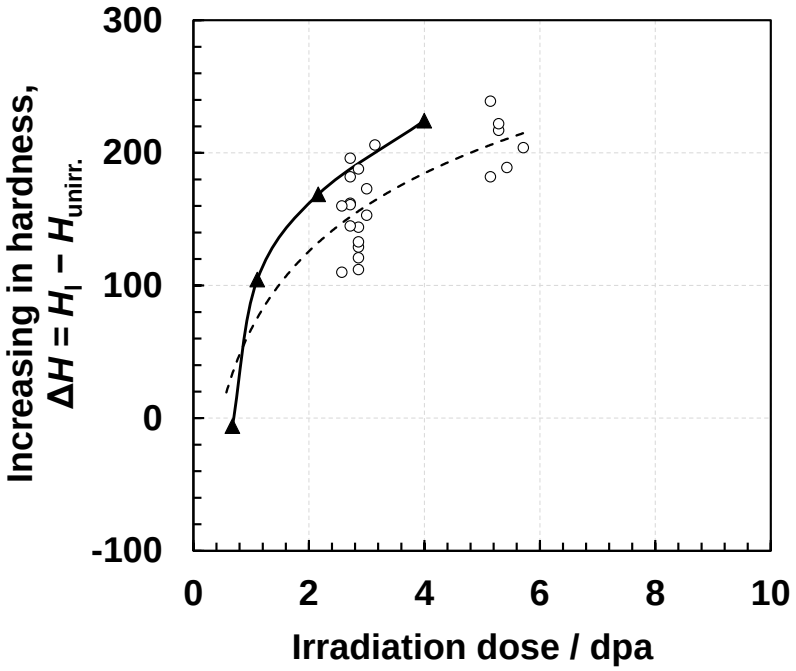

Fig. 9 Irradiation hardening, $\Delta H = H_L - H_{unirr.}$ as a function of dose. The data set from ref. [15] is also plotted.

4.7 Evaluation of strength factor of dislocation loop, α_l

Edward et al. [16] examined 3 heats of type 316 stainless steels neutron-irradiated at 275°C (548K) from 0.6 to 13.3dpa by using TEM and hardness test. The results of TEM observation and hardness are summarized in Table 2 here. They revealed that the microstructure is dominated by a very high density of small Frank loops. Based on the microstructural data listed in Table 2, change in yield strength due to the presence of Frank loop, $\Delta\sigma_y$, is estimated by using following equation,

$$\Delta\sigma_{y,l} = M\alpha_l \mu b(N_l d_l)^{1/2} \qquad (8)$$

where M, α_l, μ, b, N_l, and d_l are the Taylor factor, the barrier strength of dislocation loop (here it is Frank loop), the shear modulus of the matrix, the Burger's vector of moving dislocation, the number density of obstacles, and the mean size of obstacles, respectively. The changes in yield strength are plotted in Fig. 10. In Fig. 10, four series of plots are shown. First one is the plot of $\Delta\sigma_{y,l}$ derived from eq. (8). Second one and third one are

"converted $\Delta\sigma_y$" form change in hardness, as $\Delta\sigma_y = 2.6\Delta Hv$, which was presented in chapter 2. Second one is the data obtained by Edward et al. [16], while third one obtained by the "multi-layer model" in this chapter. Last one is the work of Kodama et al., $\Delta\sigma_y$ at 288°C obtained by tensile test, described in ref. [15]. Kodama et al. performed both hardness at room temperature and tensile test at irradiation temperature, 288°C, so we are able to evaluate the change in both hardness and yield strength. Summarizing, the estimated $\Delta\sigma_y$ is for the first one, while the others are experimentally-obtained $\Delta\sigma_y$. In Fig. 10, the trend of estimated $\Delta\sigma_{y,l}$ is consistent with that derived from the "multi-layer model" in this chapter. Here, the barrier strength of dislocation loop,

$\alpha_l = 0.2$,

was obtained. This means that Frank loops here act as a weak obstacle. On the other hand, Lucas [17] summarized that the strength of Frank loop is intermediate, where α_l is equal to 0.33–0.45. In this study, the size of Frank loop is very small, 6–10nm. These facts allow the conclusion that small Frank loops act as a weak obstacle, where α_l is 0.2.

Table 2

Average size and density of Frank loops in the irradiated 316SS heats and summary of hardness results.

ABB heat	Dose / dpa	Loop density / 10^{23} m^{-3}	Mean size / nm	$(Nd)1/2$ / 10^{7} m^{-2}	Hv at RT / kg·mm^{-2}	ΔHv / kg·mm^{-2}	$2.6\Delta Hv$ / MPa	Est.$\Delta\sigma y$ / MPa
316-F	0	–	–	–	161	–	–	–
	1.1	1.8	7.2	3.6	219	58	151	415
	4.7	1.7	11.2	4.4	282	121	315	503
316-P	0	–	–	–	161	–	–	–
	1.1	1.3	6.4	2.9	277	116	302	332
	1.6	1.6	7.5	3.5	297	136	354	399
	2.9	1.1	9.7	3.3	–			376
	4.9	2	9.6	4.4	331	170	442	505
316-K	0	–	–	–	161	–	–	–
	1	3.2	6.3	4.5	307	146	380	517
	1.6	1.6	7.4	3.4	282	121	315	396
	3.7	3.4	8.5	5.4	342	181	471	619
	5.7	1.9	9.1	4.2	419	258	671	479
	13.3	1.9	9.4	4.2	–	–	–	487

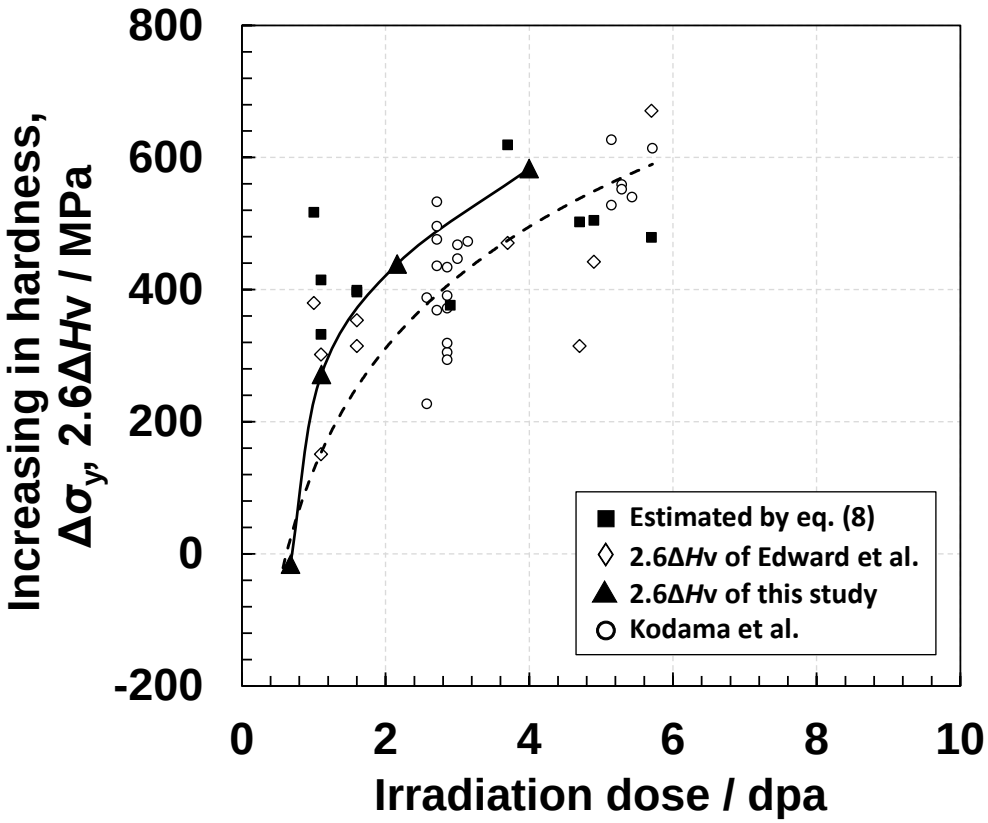

Fig. 10 Irradiation hardening as a function of dose.

4.8 Summary

The barrier strength of dislocation loop, α_l, was investigated for ion-irradiated 316 stainless steel by using nano-indentation technique. The followings are summary:

1. The range of plastic deformation zone and the depth dependence of nano-indentation hardness were investigated. When the indentation depth was critical depth, h_c, obtained from Nix-Gao plot, the deformation zone reaches to the bottom of the irradiated layer. This means that h_c can be a reasonable parameter to assume the range of deformed zone in ion-irradiated materials.

2. The multi-layer model was suggested with the assumption of the hardness as the product of volume fraction of a deformation zone and local hardness. The obtained local hardness H_L was reasonable for the evaluating the radiation hardening as a function of depth. Comparing with neutron-irradiation data, the local hardness obtained by multi-layer model here is reasonable. The power index on the power law of irradiation hardening in this study was large compared to neutron irradiation, however, the power-law discussion is not appropriate in this case because irradiation hardening is thought to reach to the saturation level (around 1dpa).

3. The barrier strength of dislocation loops obtained here is equal to 0.2. Although this value is small compared with the one shown in ref [17], $\alpha_l = 0.2$ would be appropriate because the size of loops considered here is relatively small so act as a weak obstacle.

References

[1] R. Kasada, Y. Takayama, K. Yabuuchi, A. Kimura, Fusion Eng. Des. 86 (2011) 2658.

[2] http://www.srim.org/.

[3] W.C.Oliver, G.M.Pharr, J. Mater. Res. 7 (1992) 1564.

[4] W.D.Nix, H.Gao, J. Mech. Phys. Solids 46 (1998) 411.

[5] M. Inamura, T. Suzuki, Seisan Kenkyu 42 (1990) 257 (in Japanese).

[6] A. Okada, K. Hamada, I. Ishida, E. Hirota, M. Kiritani, T. Yoshiie, J. Nucl. Mater. 233-237 (1996) 1016.

[7] T.S. Byun, K. Farrell, E.H. Lee, J.D. Hunn, L.K. Mansur, J. Nucl. Mater. 298 (2001) 269.

[8] K. Farrell, T.S. Byun, N. Hashimoto, "Mapping Flow Localization Processes in Deformation of Irradiated Reactor Structural Alloys-Final Report," Report No. ORNL/TM-2003/63.

[9] H.R. Higgy, F.H. Hammad, J. Nucl. Mater. 55 (1975) 177.

[10] S. Jitsukawa, Y. Abe, K. Suzuki, N. Ohkubo, *Effects of Radiation on Nuclear Materials*, ASTM-STP 1547 (2012) 1.

[11] N.F. Pamayotou, J. Nucl. Mater. 108-109 (1982) 456-462.

[12] K. Yabuuchi, H. Yano, R. Kasada, H. Kishimoto, A. Kimura, J. Nucl. Mater. 417 (2011) 988.

[13] J.D. Elen, P. Fenici, J. Nucl. Mater. 191-194 (1992) 766.

[14] D. Tabor, Br. J. Appl. Phys 7 (1956) 159.

[15] M. Kodama, S. Suzuki, K. Nakata, S. Nishimura, K. Fukuya, T. Kato, Y. Tanaka, S. Shima, in: Proceedings of the 8th International Symposium on Environmental Degradation of Materials in Nuclear Power Systems - Water Reactors, 1997 August, p. 833.

[16] D.J. Edwards, E.P. Simonen, S.M. Bruemmer, J. Nucl. Mater. 317 (2003) 13.

[17] G. Lucas, J. Nucl. Mater. 206 (1993) 287

Chapter 5

Contribution of finely-dispersed oxide particles

5.1 Introduction

In this chapter, oxide particles presented in oxide dispersion strengthened (ODS) austenitic stainless steel were considered as obstacles to dislocation glide. The contribution of the oxide particles to mechanical properties, i.e. the barrier strength of oxide particle, α_{oxide}, was investigated.

5.2 Objective of this chapter

1. Development of ODS austenitic stainless steel and production of its bulk–prototype, named ODS316
2. Investigation of microstructure and mechanical properties of ODS316
3. Evaluation of the barrier strength of oxide particle, α_{oxide}

5.3 Development of ODS austenitic stainless steel and production of its bulk–prototype

5.3.1 Motivation for ODS austenitic stainless steel

Oxide dispersion strengthened (ODS) ferritic steels, which are candidates for structural materials of fusion reactors and core components of advanced fission reactors, show excellent properties in high-temperature strength, creep rupture life times, and irradiation resistance due to the presence of stable nano-sized oxide particles introduced by mechanical alloying (MA) and hot consolidation [1] [2] [3] [4]. In addition to these advantageous properties, ODS ferritic steels suffer from poorer corrosion resistance than commonly used austenitic stainless steels.

Austenitic stainless steel is an attractive materials as a structural components when compared to ferritic steel due to good corrosion resistance and the much experience

with actual use in industry. However, austenitic stainless steel has poor swelling resistance. For structural materials of fusion reactors and core components of advanced fission reactors, modified austenitic stainless steel [5] with better performance in the swelling characteristics, needs to be developed. One such candidates is ODS austenitic stainless steel because ODS steels have the potential to suppress void formation due to the slow recovery of initial dislocation structure immobilized by oxide particles [6].

5.3.2 Development of ODS austenitic stainless steel

According to the recent researches on ODS 9Cr ferritic steels with Y_2O_3, adding the group 4 elements, including titanium, zirconium, and hafnium, is effective to make finer particles dispersed, as shown in Fig. 1 [7], than that in an ordinary ODS steels that do not originally include such minor elements. Okuda et al. [8] reported that the addition of a small amount of Ti sufficiently reduces the size of the oxide particle from 10 to around 3 nm in ODS-12Cr ferritic steels. Figure 2 shows size distribution of oxide particles determined by TEM in 12Cr-ODS ferritic steels in various elements addition: Ti, Nb, V and Zr [8]. The formation mechanism of extremely fine oxide particles was explained that Y–Ti–O complex oxides would precipitate as more stable oxide particles than Y_2O_3. Additionally, in 16Cr-4Al ODS ferritic sttels, which aim to improve corrosion behavior, an addition of Ti and Hf increases the number density of oxide particles one order of magnitude and decreases the average diameter [9]. Further, the Ti-added-ODS ferritic steels shows improved creep rupture strength as the manufactured cladding tubes [10]. The development of finer oxide particle would be associated with the formation of complex oxides composed of Y and the group 4 element.

The initial study of ODS austenitic stainless steels was carried out by Watanabe [11]. The effect of mechanically alloying for dissolving Y_2O_3 in austenitic matrix was studied using X-ray diffraction for the mechanically milled powders. The austenitic stainless steel powder and 0.35 wt% Y_2O_3 powder were mechanically-alloyed (MA) using a planetary ball mill with steel balls for 3–96 h under an argon atmosphere. MA was performed with a rotation speed of 440 rpm and ball-to-powder ratio of 5.5:1. The results

of XRD are shown in fig. 3 [11]. 6 h mechanically milled powders do not give the specific diffraction peak of Y_2O_3. Therefore, it is considered that thermally stable Y_2O_3 decomposed into yttrium and oxygen atoms, and dissolved into the austenitic matrix at the process of MA during introduction of super-heavy energy. After annealing at elevated temperatures above 800 °C, oxide particles were observed in the matrix examined by TEM.

Watanabe also reported [11] the most effective content of Hf and Zr for making finer particles in ODS austenitic stainless steels based on the results of hardness test. Figure 4 shows the micro Vickers hardness (50 gf) of ODS austenitic stainless steels with the addition of $0.35Y_2O_3$–*x*Hf–0.1Ti or $0.35Y_2O_3$–*y*Zr–0.1Ti (*x* = 0.4–0.8, *y* = 0.1–0.5; wt%) mechanically alloyed for 48 h and annealed at 1150 °C for 2 h. It is indicated that the optimum condition of element and its content for hardness of ODS austenitic stainless steels was 0.6 wt% Hf.

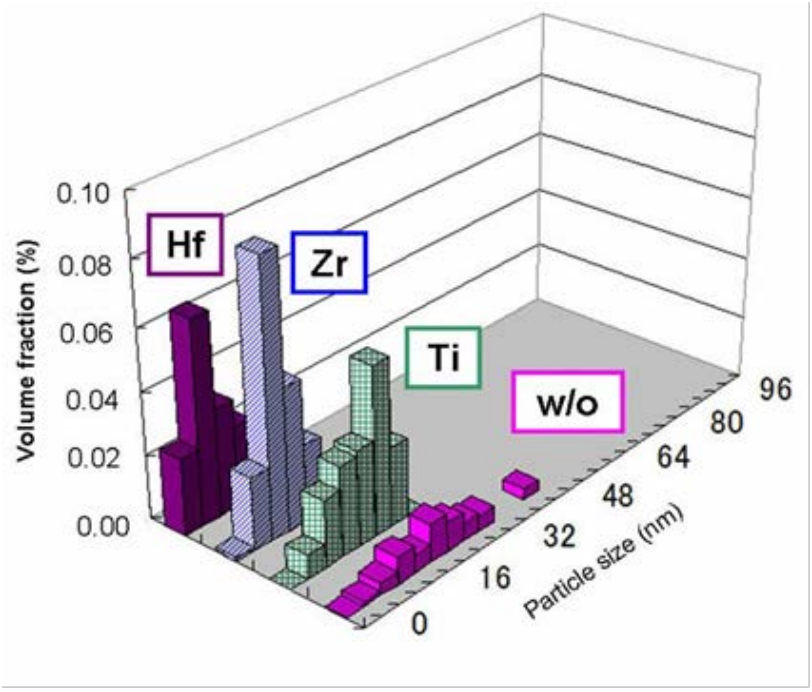

Fig. 1. Volume fraction and size of oxide particles in Fe–9Cr–0.1C–2W–$0.35Y_2O_3$–1.0X [7]. X represents the group 4 elements.

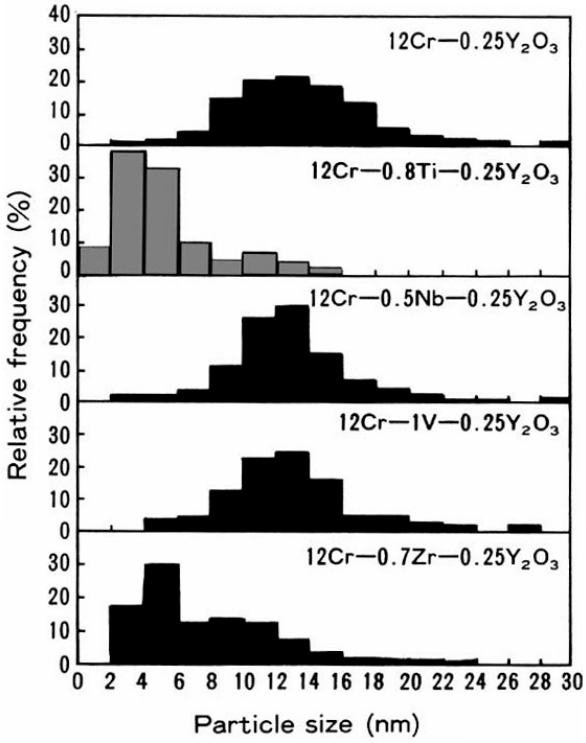

Fig. 2. Size distribution of oxide particles determined by TEM in 12Cr-ODS ferritic steels in various elements addition: Ti, Nb, V and Zr [8].

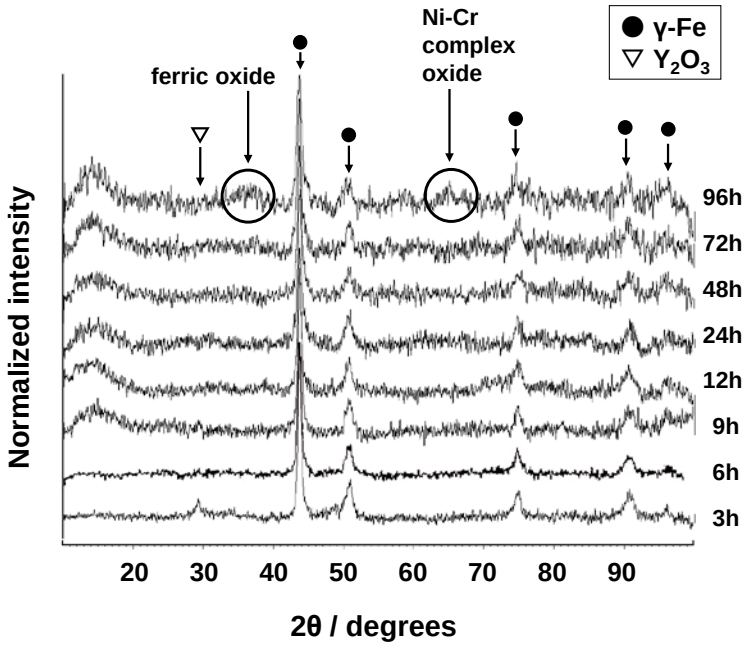

Fig. 3. X-ray diffraction patterns of MA powders milled for 3–96 h [11].

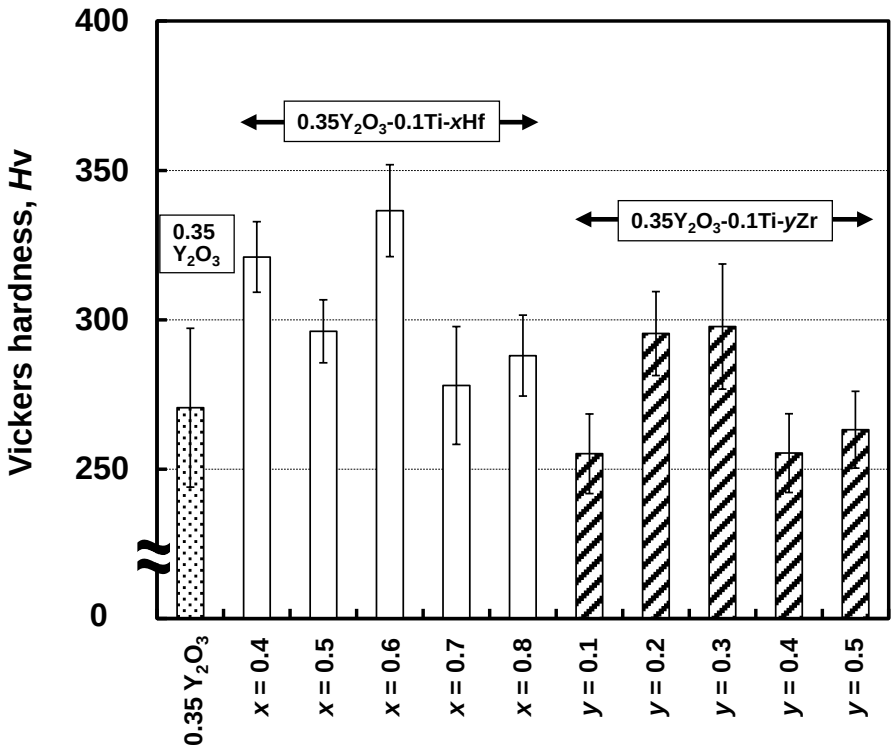

Fig. 4. Vickers hardness of samples with Hf and Zr added. Error bar shows 95 % confidence interval [11].

5.3.3 Fabrication of bulk–prototype ODS austenitic stainless steel

An advanced austenitic stainless steel, PNC316, was used as the starting material here. PNC316 is developed by the Power Reactor and Nuclear Fuel Development Corporation (presently the Japan Atomic Energy Agency: JAEA) [5]. The chemical composition of PNC316 is shown in Table 1.

Table 1
Chemical composition of PNC316 (wt%)

Material	Fe	Cr	Ni	Mo	Mn	Ti	Si	Nb	C
PNC316	Bal.	16.16	13.66	2.33	1.82	0.08	0.75	0.08	0.05

The production of the ODS austenitic stainless steel involved the following process. Pre-alloyed PNC316 powder with 150 μm in diameter was produced by argon gas atomization process. The pre-alloyed powder and 0.35 wt% Y_2O_3 powder with 0.1 wt% Ti and 0.6 wt% Hf were mechanically-alloyed (MA) using a planetary ball mill (Fritsch GmbH) with steel balls for 24 h under an argon atmosphere. MA was performed with a rotation speed of 440 rpm and ball-to-powder ratio of 1.9:1. Figure 5(a) and (b) show steel balls and mechanically-alloyed flakes after 24 h milling, respectively. As shown in fig. 5, austenitic stainless steel adhered to steel balls during ball mill due to its ductility. The mechanically-alloyed flakes have an average diameter of 1 mm, which is quite large comparing with that of ferritic ODS steels. The flakes were sealed in a steel can after degassing for 3 h at 400 ℃ in a vacuum of 10-3 torr, and then heat treated at 1150 ℃ for 2 h followed by hot extrusion into a bar with extrusion ratio of 6.4. And then the bar was hot-forged at 1150 ℃ to correct the bend then was solution- annealed at 1100 ℃ for 1 h with water-cooling. Figure 6 shows an overview of extruded bar, referenced in the following as ODS316. Weight of a bar was about 1 kg.

Componential analysis of gas atoms were carried out for the extruded ODS316 bar with the inert gas fusion method and inductively coupled plasma atomic emission spectrometry (ICP-AES). The results are summarized in Table 2. Content of Y_2O_3 estimated from the amount of Y was 0.34 wt%, which consists with initial content of Y_2O_3, 0.35 wt%. The content of excess oxygen was calculated to be 0.09 wt%, which is relatively low. The content of nitrogen, 0.05 wt%, is relatively high.

Figure 7 shows longitudinal-section microstructure of an ODS316 bar. Anisotropic microstructure was observed.

Fig. 5. Steel balls and mechanically-alloyed flakes after 24 h milling.

Fig. 6. An overview of extruded ODS316 bar.

Table 2

Amount of Y, O, and N in the extruded ODS316 (wt%).

Y	O	N
0.27	0.16	0.053

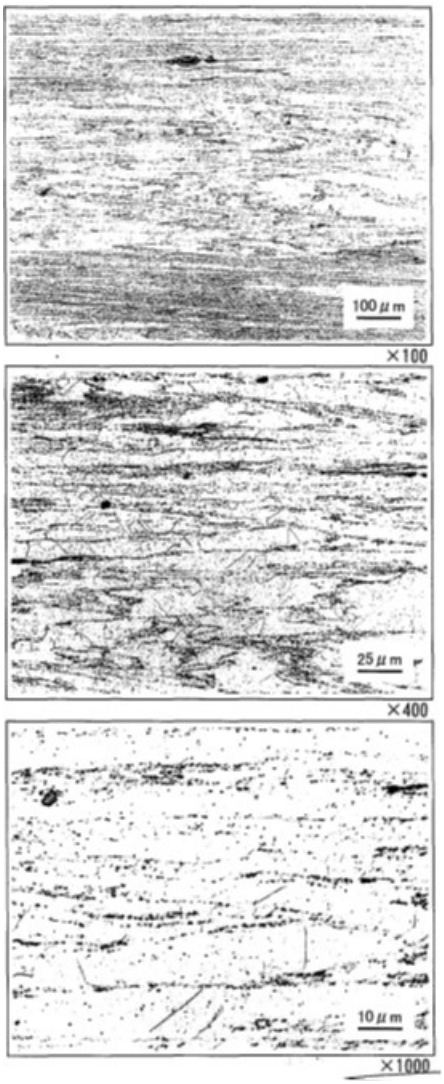

Fig. 7. Photomicrographs of longitudinal-section microstructure in ODS316 steels.

5.4 Investigation of microstructure and mechanical properties of ODS316

5.4.1 Microstructure

Samples for TEM observation were cut from the extruded alloy. Samples were thinned mechanically to ≤ 0.15 mm, and then punched to 3mm diameter disks followed by electrochemical-polishing. Final thinning of the foils was performed using a standard twin-jet electro-polishing technique (TENUPOL device) in an electrolyte (95 vol.% acetic acid, 5 vol.% perchloric acid) at 15 °C and 40 V. The thinned samples were investigated in a JEOL2010 TEM, which has a LaB_6 gun, operated at 200 kV.

Figure 8 shows typical microstructure of ODS316. We observed dispersed fine oxide particles and dislocations with low density. The austenitic grains were apt to be stretched along with extrusion direction. No pores on grain boundary were observed. As shown in fig. 9, oxide distribution was scattered especially in number density. The size distribution of oxide particles was measured from TEM micrograph, as shown in fig. 10. Microstructural parameters of ODS316 were summarized in Table 3.

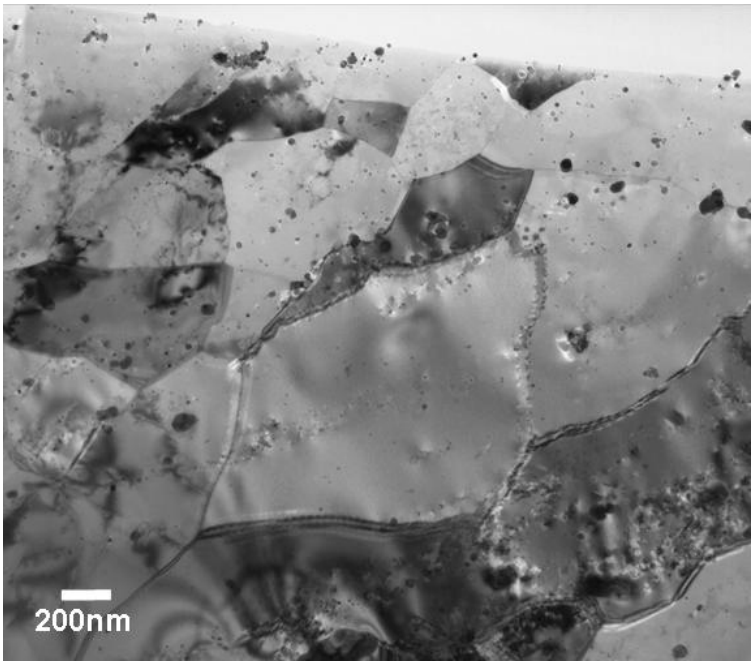

Fig. 8. Typical microstructure of ODS316.

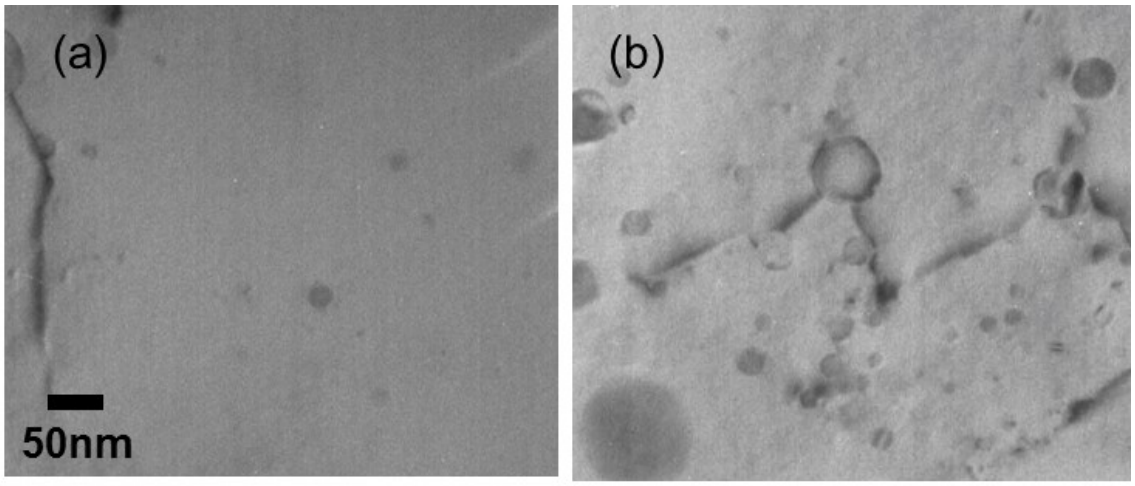

Fig. 9. Microstructure of ODS316 in (a) low density region and (b) high density region of the oxide particles.

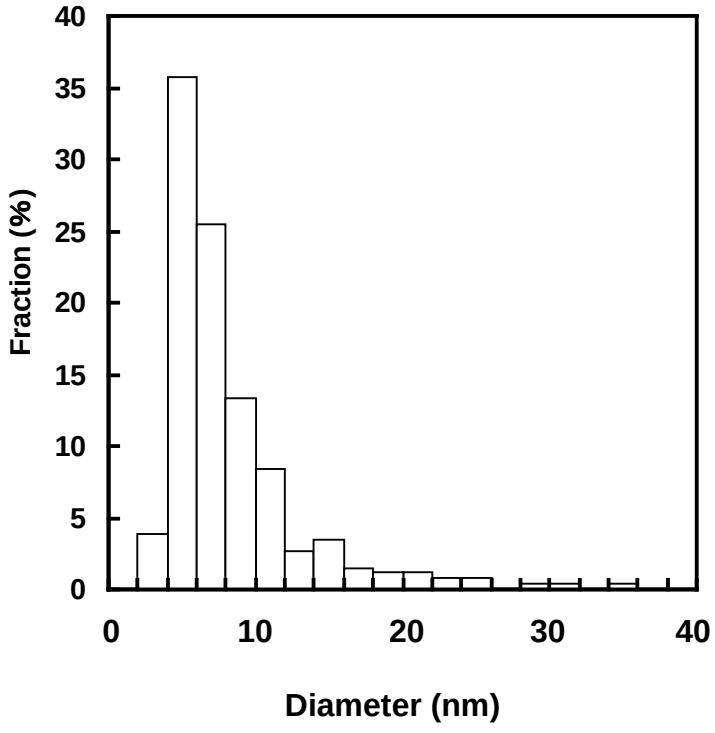

Fig. 10. Size distributions of oxide particles in ODS316 measured from TEM micrograph.

Table 3

Summary of microstructural parameters of ODS316.

Parameter	Value
Grain size / μm	0.6
Dislocation density / m^{-2}	1.4×10^{14}
Mean diameter of oxide particles / nm	8.1 ± 0.6
Number density of oxide particles / m^{-3}	6.6×10^{21}

5.4.2 Mechanical properties

The samples for tensile test are ODS316 and PNC316SA. To serve as a reference material for ODS316, specimens were also prepared from wrapper shaped PNC316, where the cold worked by 20%. PNC316 were solution annealed at 1150 °C for 2 h in a vacuum to decrease the dislocation density, referenced in the following as PNC316SA, which served as a model alloy for ODS316 without oxide dispersions and allowed quantification of the effect of oxide particles on mechanical properties. Table 4 shows the initial conditions of both specimens measured from TEM images.

Table 4

Microstructural parameters of ODS316 and PNC316SA measured from TEM images.

	ODS316	PNC316SA
Grain size / μm	1.0 ± 0.1	57 ± 3
Dislocation density / m^{-2}	1.4×10^{14}	1.0×10^{13}

The miniaturized tensile specimens were cut and machined by wire electric discharge cutting machining (EDM) from the extruded ODS316 bar. The tensile specimen was a small sheet-type tensile specimen (SS-J2), 0.3–0.8 mm thick, 1.2 mm wide and with a gauge length of 5.0 mm, illustrated in fig. 11. The holes of grip pin were made using drilling machine.

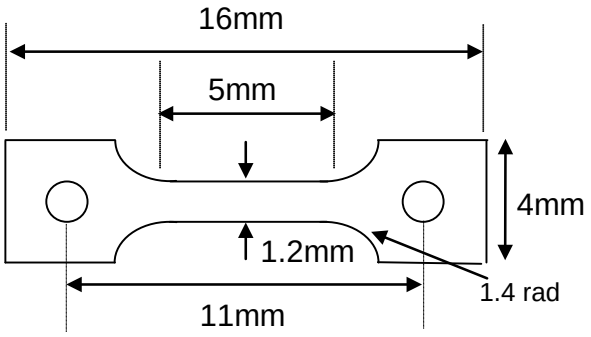

Fig. 11. Illustration of SS-J2 specimen.

Uni-axial tensile testing was performed on an instrumented Instron machine and The Shimadzu Servopulser, allowing testing temperatures from room temperature to 900 °C, in an Ar flow to avoid oxidation. The applied strain rate was in all cases 10^{-3} s^{-1}.

Yield strength, ultimate tensile strength, uniform elongation and total elongation were defined from result of tensile test as shown in Fig. 12.

Table 5

Conditions of tensile test.

Item	Condition
Temperature / °C	RT–900
Atmosphere	Argon gas flow
Strain rate / s^{-1}	10^{-3}

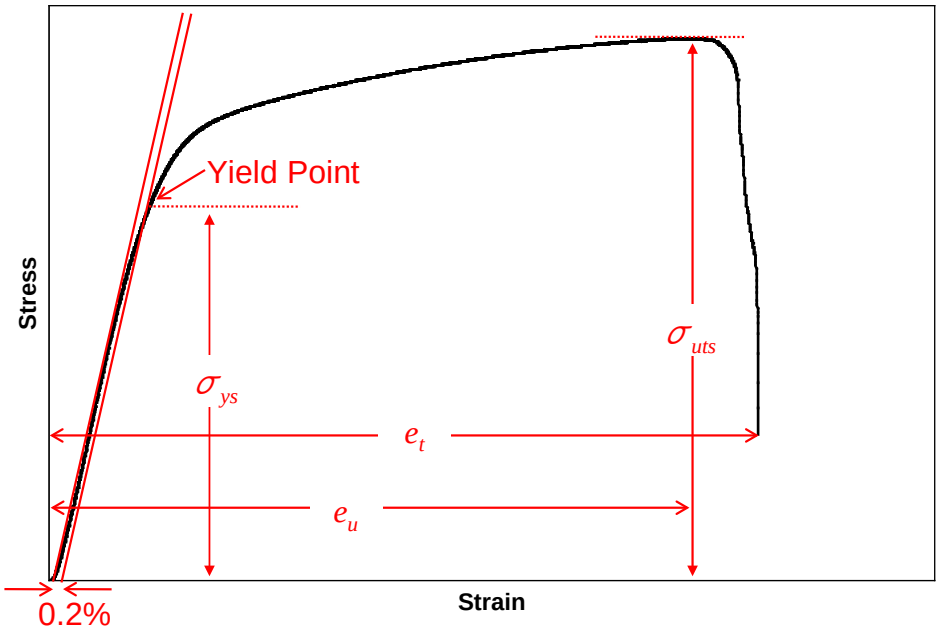

Fig. 12. Definition of yield strength, ultimate tensile strength, uniform elongation, and total elongation from the tensile test result.

Figure 13 presents the typical stress-strain curves of ODS316 steel as a function of temperature. Figuer 14 shows fractured specimen of ODS316 tested at 700 ℃. It indicates that ductile deformation and necking fracture occurred.

Figure 15 (a) presents their 0.2 % yield strength as a function of temperature. It appears that ODS316 has, as expected, a higher yield strength than the base material, PNC316SA. At room temperature, the yield strength of ODS316 is over 150% higher than that of PNC316SA. With increasing temperature the gap between the two materials decrease, that is, strength of ODS316 and PNC316SA at 700 ℃ is 242 MPa and 82 MPa, respectively. Figure 15 (b) shows ultimate tensile strength as a function of temperature. The ultimate tensile strength of both ODS316 and PNC316SA exhibits similar behavior to the yield strength. The value of ODS316 at room temperature and 700 ℃ are 40% and 27% higher than of PNC316SA.

The uniform elongation and the total elongation are presented in fig. 16 as a function of temperature. Both values of ODS316 present above 20% at room temperature, which is a practicable ductility. With increasing temperature below 500 ℃, the uniform elongation increases, however, decrease from 550 ℃. With increasing temperature the total elongation increases for ODS316, but not for PNC316SA. From the room temperature to 500 ℃, the values of uniform and total elongation in ODS316 are similar, while the gap between uniform elongation and total elongation increase above 500 ℃.

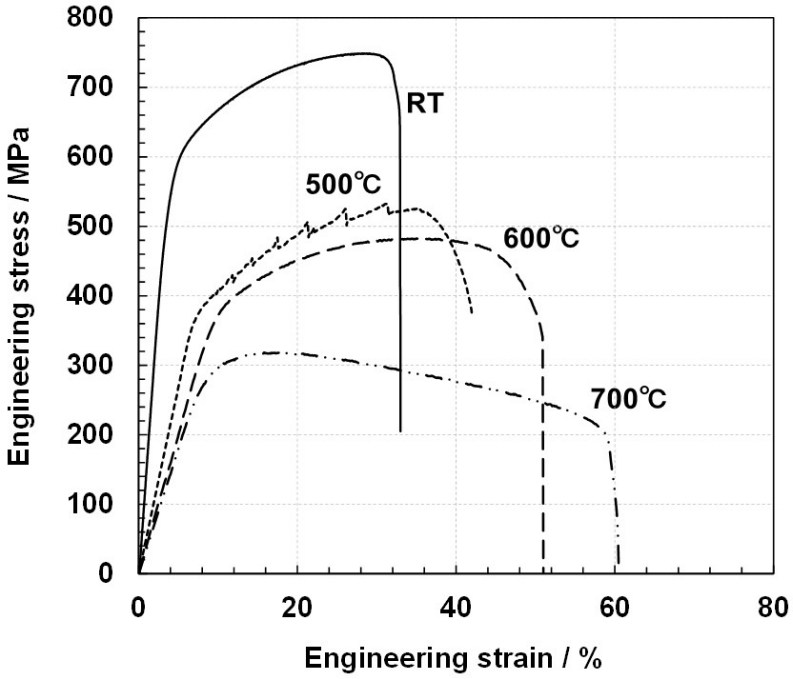

Fig. 13. Typical stress-strain curves of ODS316 steel as a function of temperature.

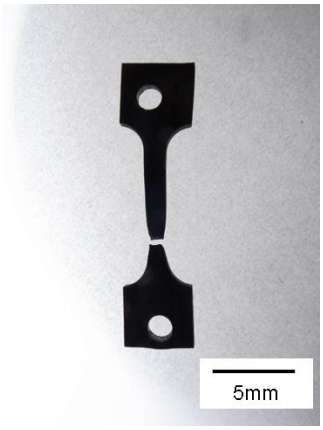

Fig. 14. A fractured specimen of ODS316 tested at 700 °C.

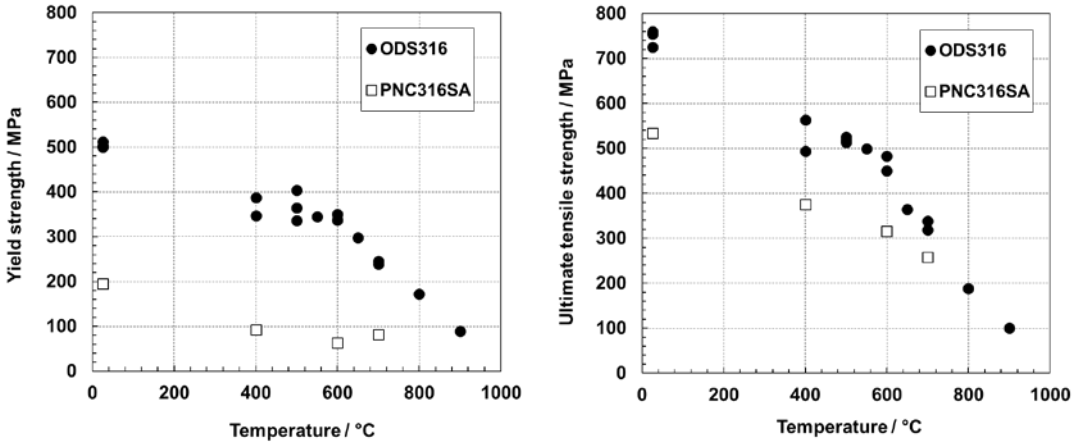

Fig. 15. Yield strength and ultimate tensile strength of ODS316 and PNC316SA as a function of temperature.

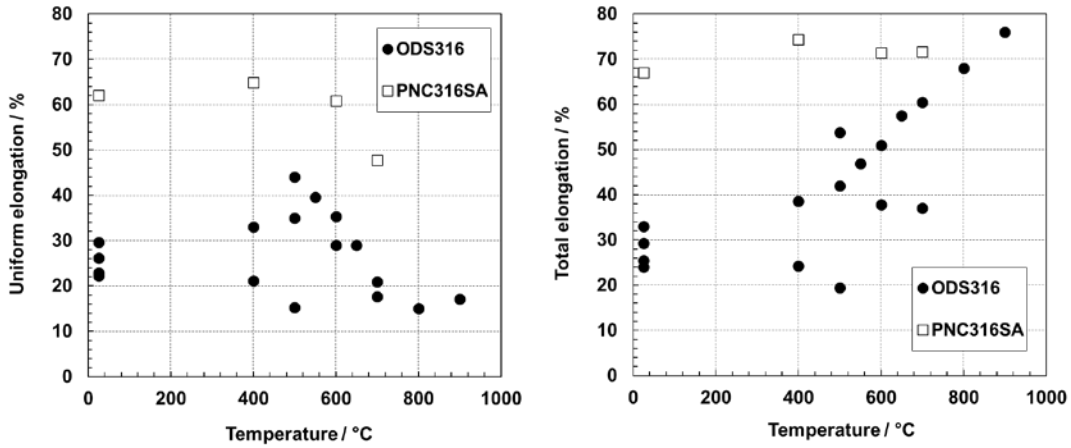

Fig. 16. (a) Uniform elongation and (b) total elongation of ODS316 and PNC316SA as a function of temperature.

5.5 Barrier strength of oxide particles, α_{oxide}, in an ODS austenitic stainless steel

As ODS steels, it is expected that the increment of yield strength for ODS316 was explained by the existence of fine oxide particles as obstacles to dislocation glide. According to the theory of dispersed barrier hardening [12][13], an increase in yield strengths, $\Delta\sigma_y$, is related to the increase in applied stress required to move a dislocation through obstacles with strength factor α_{oxide} such that

$$\Delta\sigma_{y,\,oxide} = M\alpha_{oxide}\,\mu b(N_{oxide}\,d_{oxide})^{1/2}, \quad (1)$$

where M, α_{oxide}, μ, b, N_{oxide}, and d_{oxide} are the Taylor [12] factor, barrier strength of obstacles, the shear modulus of the matrix, the Burger's vector of moving dislocation, the density of obstacles and the mean diameter of obstacles, respectively. In the present study, with the Taylor factor of 3.06 [14], the shear modulus of 74×10^3 MPa at room temperature, the Burger's vector of 0.2546 nm, and a value of $\alpha_{oxide} = 1$, $\Delta\sigma_{y,\,oxide} = 422$ (MPa) was obtained at room temperature. In Fig. 17, the comparison of the increase in yield strength is shown.

On the other hand, a significant Hall–Petch type contribution originated from the small grain size of ODS316 is also expected. As shown in Table 1, the grain size of ODS316 is quite small compared with that of PNC316SA. The increase in yield strength by grain size reduction, $\Delta\sigma_{y,\,D}$, is estimated thorough the equation as

$$\Delta\sigma_{y,\,D} = k\,(D_{ODS}^{-1/2} - D_{316SA}^{-1/2}), \quad (2)$$

where k, D_{ODS}, and D_{316SA} are the Hall–Petch parameter, the grain size of ODS316, and the grain size of PNC316SA, respectively. The Hall–Petch parameter here is 10.46 MPa·mm$^{1/2}$, which is the quoted value from the work of Varin and Kurzydlowski[15]. The result of the estimation is also shown in Fig. 17.

Looking at Fig. 17, a Hall–Petch type contribution for the increase in yield strength, $\Delta\sigma_{y,\,D}$, is 287 MPa, which is mostly the same as the actual change $\Delta\sigma_y$: 325MPa. This results here allow the conclusion that the difference in yield strength between

ODS316 and PNC316SA can be explained mostly by the reduction of grain size. Therefore, little contribution of fine oxide particles in the increment of yield strength can be considered at room temperature. In the room temperature test, the Hall–Petch mechanism may be dominant to determine the yield strength.

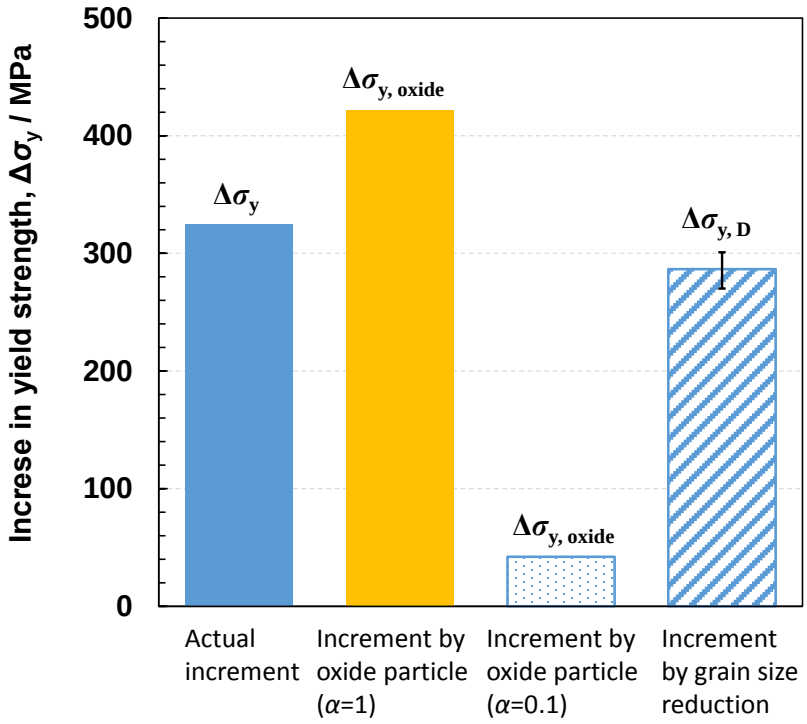

Fig. 17 Comparison of the increase in yield strength. (a) Actual difference in yield strength between ODS316 and PNC316SA. (b) Increase due to the presence of oxide particle, estimated by eq. (1) with α=1. (b) Increase due to the presence of oxide particle, estimated by eq. (1) with α=0.1. (d) Increase due to grain size reduction, estimated by eq. (2).

To fill the little difference between $\Delta\sigma_y$ and $\Delta\sigma_{y,\,D}$, the contribution of oxide particles can be estimated as decreasing the value of α_{oxide}. Use α_{oxide} = 0.1 in eq. (1), $\Delta\sigma_{y,oxide}$ results in 42 MPa. With considering the error in $\Delta\sigma_{y,\,D}$, α_{oxide} should result in the range of 0.08–0.1. This value is quite small compared with that discussed in the past study [16]. ODS316 has a heterogeneous distribution of oxide particles in the matrix, so the preferential dislocation gliding in low density region of oxide particles may occur. That's the reason why the apparent value of α_{oxide} was small.

One of the possible contribution of the presence of oxide particle is the suppression of grain growth in ODS316. During the processing of ODS316, annealing at 1150°C for 2h is performed. If there are no oxide particle in the stainless steel, 2h–annealing at 1150°C would be leading to grain growth. But the resultant grain size in ODS316 is about 0.6μm. Thus during annealing, pinning effect by the oxide particles against grain boundary migration could be expected [17].

In the present research, ODS316 is not cold–worked. So the values of yield strength or ultimate tensile strength were not so high and not satisfying the criteria of stainless steels for core component of fast breeder reactor. Basically ODS steels are hot– or cold–rolled and induced dislocations in the matrix during their fabrication process [18]. Indeed, in the past study, ODS steels have showed excellent properties in creep rupture life times due to the presence of stable and nano-sized oxide particles [4]. This is because the oxide particle allow to the slow recovery of initial dislocation structure by immobilizing them [6] during creep deformation at elevated temperature. In ODS316, an excellent creep strength due to the presence of oxide particles is also expected as well.

5.6 Summary

The barrier strength of oxide particle, α_{oxide}, was investigated for the ODS austenitic stainless steel (ODS316). The followings are summarized:

1. ODS316 had dispersed fine oxide particles with a low dislocation density. The mean diameter and number density of oxide particles were 8.1 nm and 6.6×10^{21} m^{-3}, respectively.

2. Yield strength and ultimate tensile strength of ODS316 were higher compared to those of PNC316SA in room temperature to 700 °C.

3. Little direct contribution of fine oxide particles as obstacles in the increment of yield strength of ODS316 was revealed at room temperature. The apparent value of α_{oxide} was in the range of 0.08–0.1. The role of oxide particle in ODS316 may be summarized as; oxide particles are effective for the suppression of grain growth in ODS316; oxide particles may immobilize an initial dislocation structure and impede its recovery in elevated temperature creep testing.

References

[1] S. Ukai, M. Harada, H. Okada, M. Inoue, S. Nomura, S. Shikakura, K. Asabe, T. Nishida, M. Fujiwara, J. Nucl. Mater. 204 (1993) 65.

[2] S. Ukai, M. Harada, H. Okada, M. Inoue, S. Nomura, S. Shikakura, T. Nishida, M. Fujiwara, K. Asabe, J. Nucl. Mater. 204 (1993) 74.

[3] S. UKAI, T. NISHIDA, H. OKADA, T. OKUDA, M. FUJIWARA, K. ASABE, J. Nucl. Sci. Technol. 34 (1997) 256.

[4] M.. Toloczko, D.. Gelles, F.. Garner, R.. Kurtz, K. Abe, J. Nucl. Mater. 329-333 (2004) 352.

[5] I. Shibahara, S. Ukai, S. Onose, S. Shikakura, J. Nucl. Mater. 204 (1993) 131.

[6] I. Kim, J. Hunn, N. Hashimoto, D.. Larson, P.. Maziasz, K. Miyahara, E.. Lee, J. Nucl. Mater. 280 (2000) 264.

[7] Y. Uchida, S. Ohnuki, N. Hashimoto, T. Suda, T. Nagai, T. Shibayama, K. Hamada, N. Akasaka, S. Yamashita, S. Ohstuka, T. Yoshitake, MRS Proc. 981 (2007).

[8] T. Okuda, S. Nomura, S. Shikakura, K. Asabe, S. Tanoue, M. Fujiwara, in:, Proc. a Symp. Spons. by TMS Powder Metall. Comm., 1989, p. 195.

[9] Y. Uchida, Thesis, Hokkaido University, 2008.

[10] S. Ukai, S. Mizuta, T. Yoshitake, T. Okuda, M. Fujiwara, S. Hagi, T. Kobayashi, J. Nucl. Mater. 283-287 (2000) 702.

[11] M. Watanabe, Fundamental Research for Development of Nano-Particle Dispersion Strengthened Austenitic Steels, Hokkaido University, 2009.

[12] U. Kocks, Metall. Mater. Trans. B 1 (1970) 1121.

[13] P.M. Kelly, Int. Met. Rev. 18 (1973) 31.

[14] H. Higgy, F. Hammad, J. Nucl. Mater. 55 (1975) 177.

[15] R.. Varin, K.. Kurzydlowski, Mater. Sci. Eng. A 101 (1988) 221.

[16] M. Alinger, G. Odette, D. Hoelzer, J. Nucl. Mater. 333 (2004) 382.

[17] M. Yamamoto, S. Ukai, S. Hayashi, T. Kaito, S. Ohtsuka, J. Nucl. Mater. 417 (2011) 237.

[18] D.A. McClintock, M.A. Sokolov, D.T. Hoelzer, R.K. Nanstad, J. Nucl. Mater. 392 (2009) 353.

Chapter 6

Integrative model for mechanical property changes under irradiation

To predict the material properties under irradiation, “microstructure–mechanical properties correlations” and “property–property correlations” are investigated.

6.1 Microstructure–mechanical properties correlations

Through the investigation on; neutron-irradiated stainless steel; solution-annealed model austenitic alloy with different carbon concentration; ion-irradiated stainless steel; oxide dispersion strengthened stainless steel; microstructure–mechanical properties correlations are established based on Orowan’s equation,

$$\Delta\sigma_y = M\alpha\mu b(Nd)^{1/2} \qquad (1).$$

The barrier strength of dislocation line, α_d, is investigated in neutron-irradiated PNC316 up to 16.0–103dpa at 502–734°C. Yield strength decreased after neutron irradiation mainly due to recovery of network dislocation structure. The changes in yield strength are not in agreement with that evaluated from Orowan’s equation. But the different tendency between the results of tensile test and hardness test is obtained and the formation of large-size carbide is observed. Thus a possible dependence of α_d on temperature and carbon concentration was suggested. Detailed examination on α_d in the model austenitic alloy revealed that α_d depend on test temperature when carbon concentration in matrix is low. This can apply to neutron-irradiated stainless steel such that the depletion of carbon atoms in the matrix due to precipitation of carbide leads to decrease of α_d.

The barrier strength of dislocation loop, α_l, is investigated in ion-irradiated stainless steel. Nano-indentation technique and the “multi-layer model” of hardness were applied to the investigation of α_l. The local hardness H_L in the irradiated region was obtained by means of sectioning and the suggested multi-layer model. Irradiation hardening, evaluated by $\Delta H = H_L - H_{unirr.}$, was comparable to the past research. The evaluated α_l is equal to 0.2, which would be appropriate because the size of loops considered here is relatively small so act as a weak obstacle.

The barrier strength of dislocation loop, α_{oxide}, is investigated in oxide dispersion

strengthened stainless steel. Investigation of mechanical properties and microstructure of the fabricated ODS316 bulk sample showed smal contribution of fine oxide particles as obstacles in the increment of yield strength of ODS316 at room temperature, leading to the conclusion that α_{oxide} is equal to 0.08–0.1. Little contribution to yield strength was found, however, the contribution to suppress the grain growth in ODS316 was suggested. Further, a strain field surrounding the oxide particle was found, which may have a role for pinning glide dislocations repulsively or attractively during creep deformation.

The strength factor α evaluated in this study is summarized in Table 1.

Table 1

Strength factors evaluated in this study.

Obstacle	Symbol	Value	Description
Dislocation loops	α_{loop}	0.2	This value is evaluated by comparing to the work of Edward et al., where dislocation loop is assumed to be small-size Frank loop.
Dislocation lines	α_{d}	0.24	This value is the one in PNC316SA at room temperature. When the concentration of carbon atoms in the matrix is low, α_{d} depends on temperature. For example, α_{d} is equal to 0.1 in the model alloy with 19 wppmC at 700°C.
Precipitates	α_{p}	–	Not discussed here due to its small number density.
Voids	α_{v}	–	Not discussed here due to its small number density.
Oxide particles	α_{oxide}	0.08–0.1	This value is evaluated in the tensile test at the strain rate of 10^{-3} s^{-1} at room temperature. Oxide particles may contribute to the suppression of grain growth and the pinning glide dislocations during creep deformation at elevated temperature.

6.2 Property–property correlations (scale bridging)

6.2.1 Nano-hardness – Vickers hardness

In the ion-irradiated sample, the multi-layer model was suggested with the assumption of the hardness as the product of volume fraction of a deformation zone and local hardness, where the deformation zone was assumed to be a simple hemisphere. The obtained local hardness H_L was reasonable for the evaluating the radiation hardening as a function of depth.

6.2.2 Vickers hardness – Yield strength

Linear relationship between Vickers hardness and yield strength was found in solution-annealed PNC316 at room temperature. The correlation was

$$\sigma_y = 2.6Hv - 61 \quad (1)$$

where the slope of the eq. (1) is consistent with the relevant study. The intercept in the correlation might depend on materials, heat treatment, and the way of cold working (rolling vs. uniaxial stretching).

6.3 Integrative model

As a summary, the following integrative model was suggested in this study.

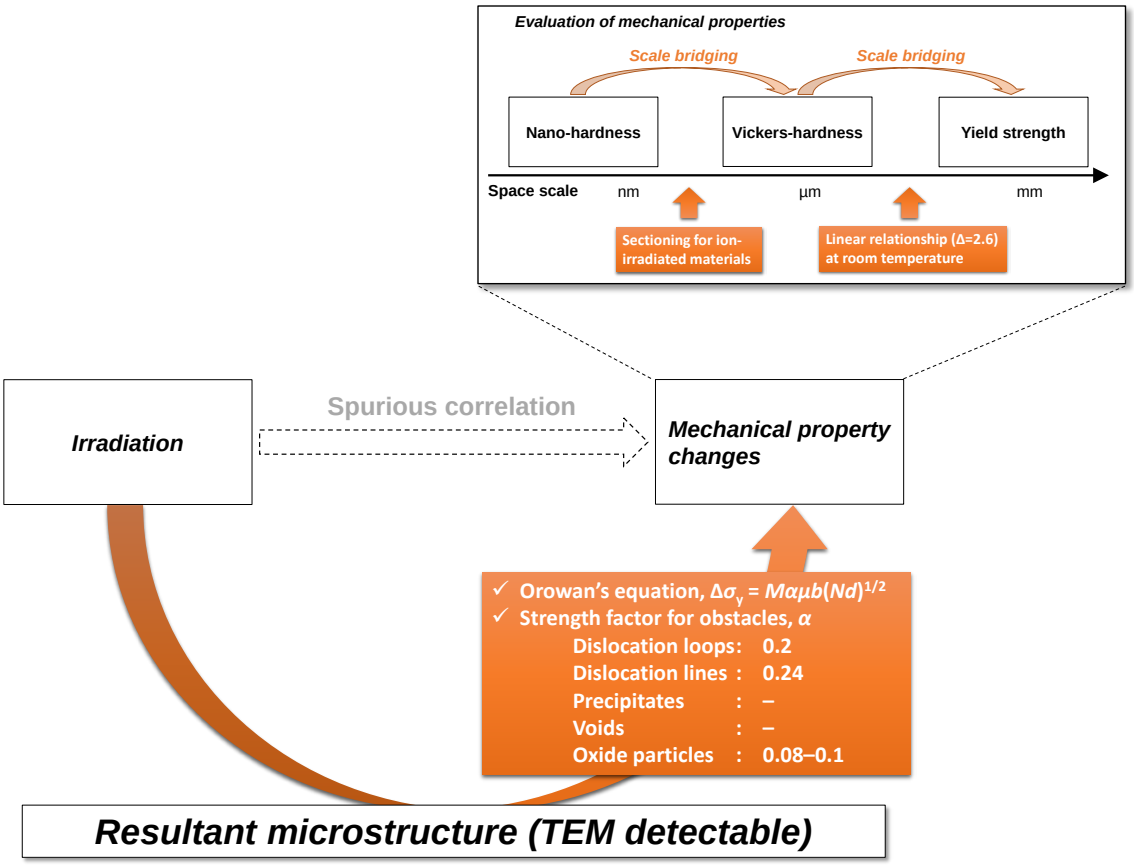

Fig. 1 Schematics describing integrative model suggested in this study.

Appendix A

Morphology of oxide particles in ODS austenitic stainless steel

1.1 Introduction

Oxide dispersion strengthened (ODS) steels, which are a candidate for structural materials for fusion reactors, have an excellent thermal creep resistance due to a high density of small oxide particles dispersed in the matrix. Although the ODS method has been applied to the development of ferritic steels, ODS steels still have poor corrosion resistance compared to austenitic steels. To improve the corrosion resistance of ODS steels, an ODS austenitic stainless steel, based on an advanced SUS316 steel, has been developed by mechanically alloying (MA) and hot extrusion with an addition of minor alloying elements.

Knowledge about oxide particles and their relation with the matrix would help to improve the base austenitic steels. One study shows that the lattice coherency of the particles with the surrounding matrix is important for strengthening mechanisms [1]. On the other hand, the observed trapping of helium at the interfaces of Y_2O_3 particles in ferritic ODS alloy PM2000 in Ref. [2] suggests that these particles may be able to reduce high-temperature helium embrittlement, similar to the effect of coherent Ti carbides in austenitic steels [3]. Small oxide particles dispersed with a high density are also expected to be effective traps for vacancies and interstitials [4][5]. Therefore, microstructural analysis on oxide particles would provide valuable knowledge to improve the irradiation resistance of ODS austenitic steels.

The main focus of this section is to understand the structure and the orientation relationship of the dispersed oxide particles with respect to the matrix by using transmission electron microscopy (TEM).

1.2 Experimental

ODS316 was prepared as described in chapter 5. Samples were investigated in JEOL JEM-2010 and JEM-2010F microscopes. High resolution transmission electron microscopy (HRTEM) images were evaluated using fast Fourier transformation (FFT).

X-ray energy dispersive spectroscopy (EDS) equipped with TEM was used to identify the chemical composition of the oxide particles.

1.3 Results

1.3.1 Crystal structure and composition of complex oxide

The high magnification observation revealed that the particles basically have a faceted shape, as shown in Fig. 1. From the results of EDS, it was found that most of particles were mainly complex oxides, where the atomic ratio of metallic elements is roughly Y:Hf = 1:1. Fig. 2a and b show a HRTEM image and an electron diffraction pattern from an oxide particle, respectively. The oxide particle is clearly faceted. The lattice spacing obtained from Fig. 2b is consistent with the database table for defected fluorite $Y_2Hf_2O_7$ [6] based on powder diffraction pattern (Table 1). Moreover, the HRTEM image and its inverse fast Fourier transformation (IFFT) image indicated that the atomic plane spacing of the lattice fringes from {200} and {111} is also consistent with the database table, respectively (see Fig. 2d and e).

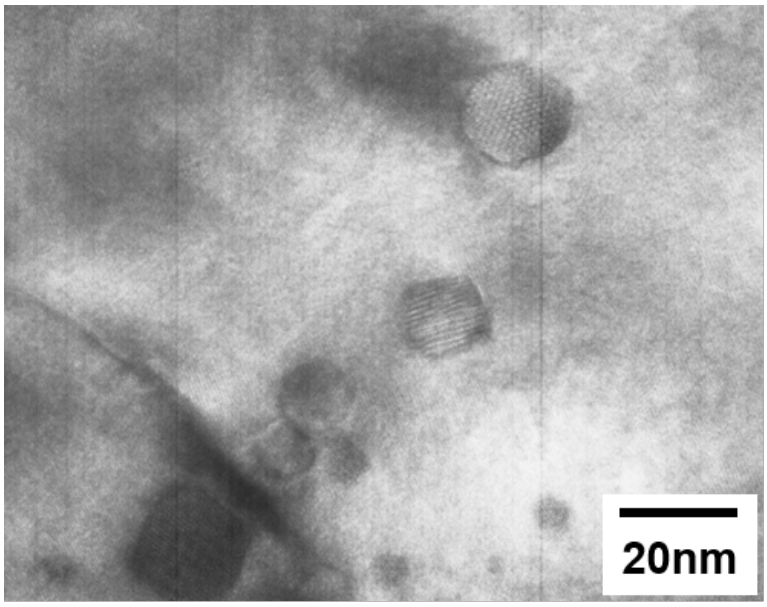

Fig. 1 TEM micrograph showing faceted particles having a diameter of around 10 nm in the ODS austenitic stainless steel.

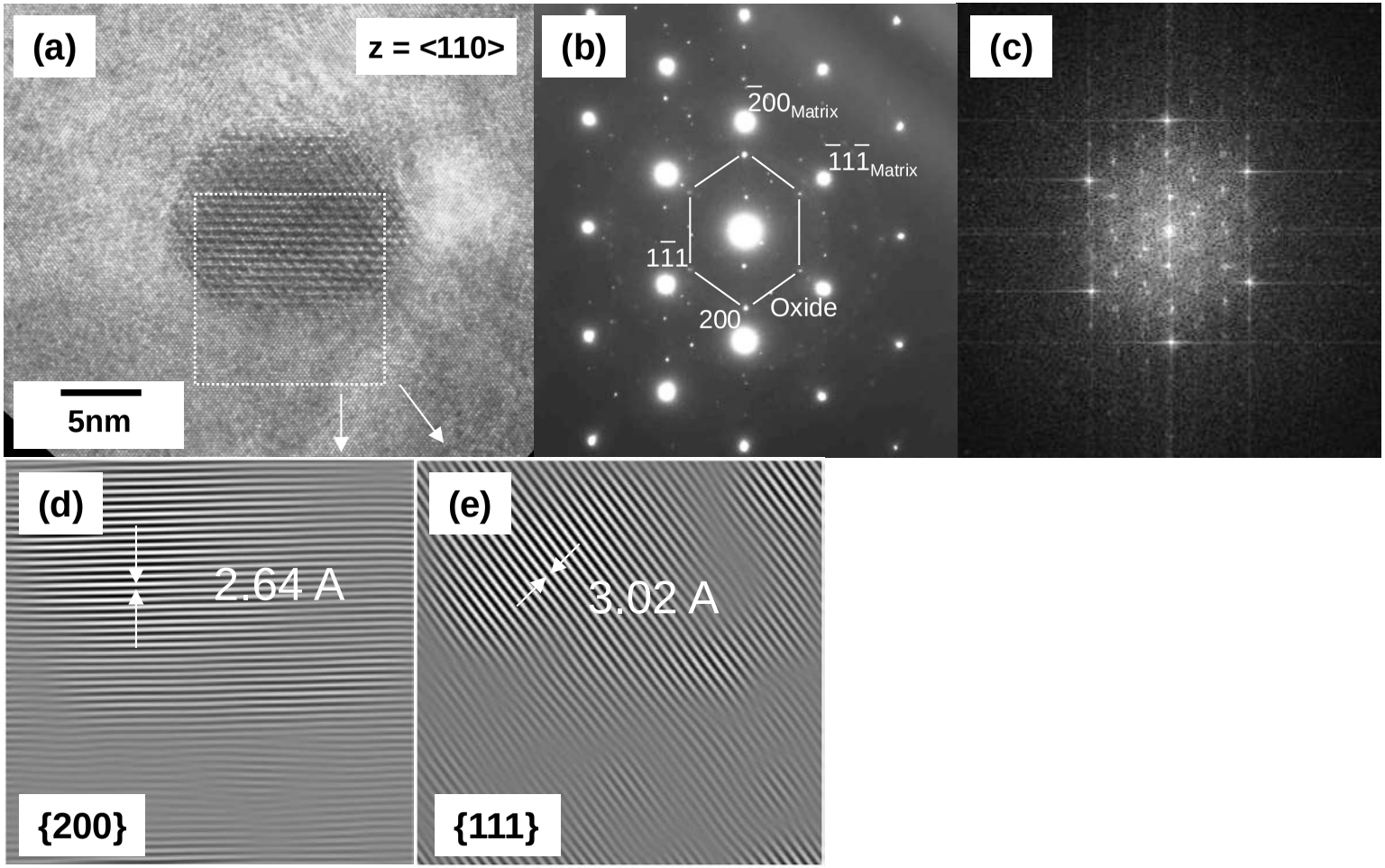

Fig. 2 (a) HRTEM image and (b) electron diffraction pattern from oxide particle. (c) FFT image obtained from (a). IFFT images corresponding to (d) {200} and (e) {111} of the oxide particle.

Table 1

Crystallographic data of defect fluorite Y2Hf2O7 based on powder diffraction pattern [6].

hkl	d (Å)
111	3.001
200	2.601
220	1.839
311	1.563
222	1.5012

The details of the crystal structure of $Y_2Hf_2O_7$ can be discussed. The crystal structure written as a general formula of $A_2B_2O_6O'$ is known as an oxide pyrochlore with a space group symmetry of $Fd\overline{3}m$ [7][8]. The pyrochlore structure is a derivative of the fluorite structure (AX_2), e.g., cubic ZrO_2, except that there are two cation sites and one-eighth of the anions are absent [9]. There are three distinct anion sites, i.e., O: 48f (*x* 1/8 1/8), O′: 8b (3/8 3/8 3/8) and the 8a (1/8 1/8 1/8) anion site is generally vacant, while the A- and B-site cations are located on 16d (1/2 1/2 1/2) and 16c (0 0 0), respectively, using Wyckoff notation with the origin on B site (cell choice 2). The 48f oxygen is described with the positional parameter *x*. In the case where $x = 0.3125$ (= 5/16), the crystal structure is the ideal pyrochlore, with the coordination polyhedron of the A- and B-site as a trigonal scalenohedron (distorted cubic) and a regular octahedron, respectively. On the other hand, the A-site is a regular cube and B-site is a trigonal antiprism (distorted octahedral) where *x* is 0.375 (3/8). The A- and B-site cations are ordered parallel to the <110> directions. The unit cell edge of pyrochlore is doubled ($2 \times 2 \times 2$) by ordering of the A- and B-site cations on the fluorite lattice [6][7][8]. A characteristic feature of pyrochlore in selected area diffraction (SAD) patterns is the presence of 1/2 $\{111\}_F$ type satellite reflections, which arise from the correlated {111} ordering of metal ion and oxygen vacancies [8][10]. The “F” subscript represents the parent fluorite reflection.

The fluorite-related structure, including pyrochlore, depends on the ionic radius ratio of A- and B-site cations, r_A/r_B. When the ratio is less than 1.46, which means A- and

B-site cations are similar in size, the anion-deficient fluorite structure is favored (e.g., $Y_2Zr_2O_7$, r_A/r_B = 1.42 [11]) by disordering of A- and B-site cations. When the ratio lies in the range 1.46–1.78, the material is the ordered pyrochlore structure (e.g., $La_2Zr_2O_7$, r_A/r_B = 1.61 [11][12]). If the radius ratio is higher than 1.78, a monoclinic layered perovskite type structure is formed (e.g., $La_2Ti_2O_7$, r_A/r_B = 1.92) [11][13].

In the SAD patterns obtained from $Y_2Hf_2O_7$ in this study, the 1/2 $\{111\}_F$ superlattice reflection was absent. Additionally, using the ionic radius of Y^{3+} in eight-fold coordination (r_Y = 1.019 Å) and Hf^{4+} in six-fold coordination (r_{Hf} = 0.71 Å) [14], the ionic radius ratio, r_Y/r_{Hf}, was calculated to be 1.44, which is slightly lower than the threshold value of 1.46. Based on these results, most of the oxide particles were identified as the anion-deficient fluorite structure $Y_2Hf_2O_7$ (cubic) with a lattice constant of 5.201 Å. The determination of the precise crystal structure of this particle, such as cationic disorder or the 48f oxygen positional parameter *x*, requires additional investigations, for instance, neutron diffractometry.

1.3.2 Nano-scale shape and orientation relationship of oxide particle

As mentioned above, the oxide particles basically have a faceted shape. When discussing the interface structure of an oxide particle, revealing its shape could be a key because the character of the interface is expected to depend on its face, i.e., the plane index.

Fig. 3 presents HRTEM and FFT images of a faceted oxide particle observed along (a) *z* = <110> and (b) *z* = <100>. The shape of an actual projection view of the particle can be deduced, as shown by the white line in Fig. 3, as a distorted octagon along the *z* = <110> projection and a near regular octagon for the *z* = <100> projection, respectively. These observations suggest a model of oxide particle as a polyhedron surrounded with {100}, {110} and {111} planes, as shown in Fig. 4a. Fig. 4b and c show the projected view of the model from the <110> and <100> directions corresponding to the experimental image of the oxide particle, as shown in Fig. 3.

Additionally, from Fig. 3c and d, an orderly orientation relationship between the faceted particle and the surrounding matrix can be expressed as follows:

$\langle 110 \rangle_{Matrix}$ // $\langle 110 \rangle_{Oxide}$ and $\{200\}_{Matrix}$ // $\{200\}_{Oxide}$,

$\langle 110 \rangle_{Matrix}$ // $\langle 110 \rangle_{Oxide}$ and $\{111\}_{Matrix}$ // $\{111\}_{Oxide}$

$\langle 100 \rangle_{Matrix}$ // $\langle 100 \rangle_{Oxide}$ and $\{220\}_{Matrix}$ // $\{220\}_{Oxide}$

$\langle 100 \rangle_{Matrix}$ // $\langle 100 \rangle_{Oxide}$ and $\{200\}_{Matrix}$ // $\{200\}_{Oxide}$

Thus, the oxide particle with a face-centered cubic (FCC) base crystalline structure, defected fluorite structure, is embedded in the FCC matrix without any rotation.

A well-oriented relationship between the particle and the surrounding matrix exhibits extra spots originating from double diffraction in SAD patterns as per the details shown in Fig. 5. In the SAD image, there are double-diffraction spots occurring when the matrix-diffracted beam is rediffracted by the oxide (black filled circles), and then occurring when the above reflection is rediffracted, again, by the oxide (gray filled circles). The double-diffraction spots were also seen in Fig. 6, located between the direct beam and the oxide particle reflection.

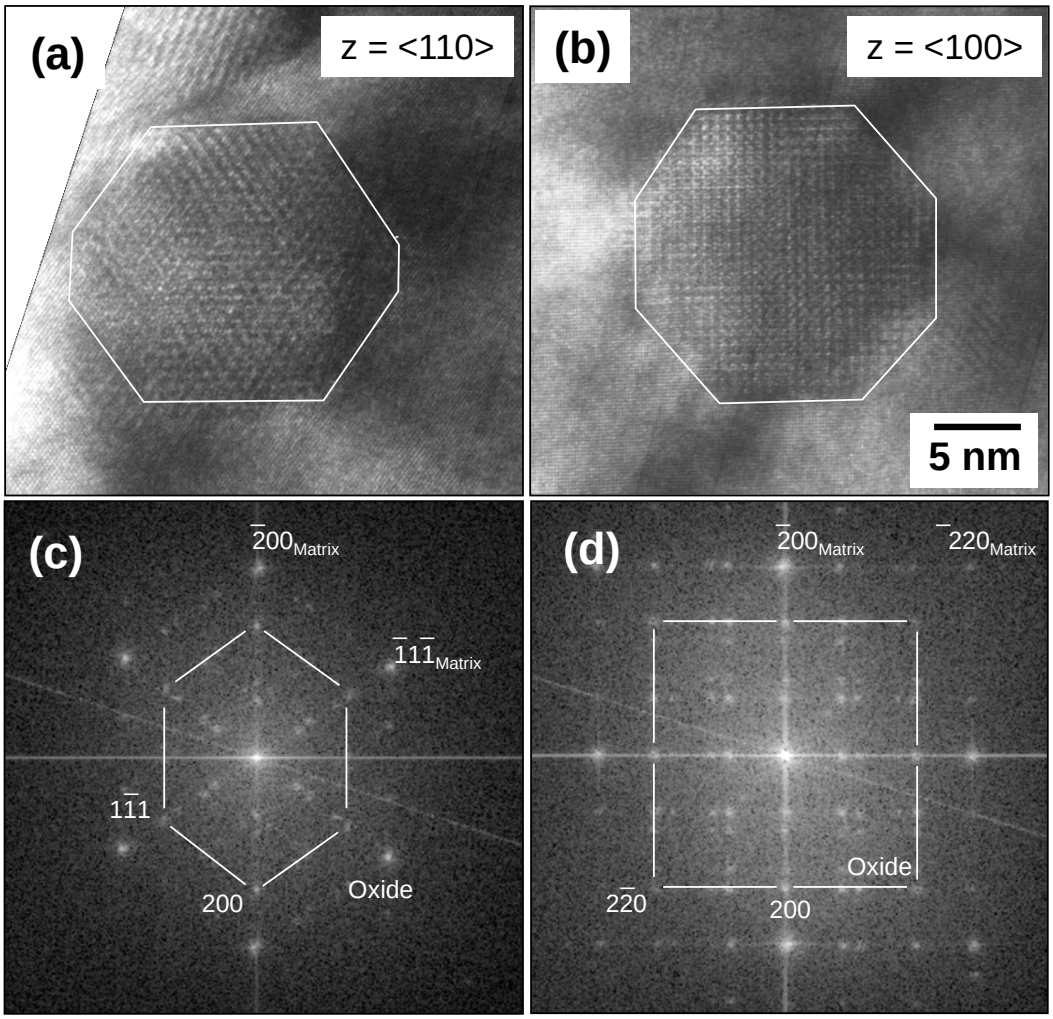

Fig. 3 HRTEM images of an oxide particle viewed along the zone axis of (a) *z* = <110> and (b) *z* = <100>, and corresponding FFT images for (c) *z* = <110> and (d) *z* = <100>.

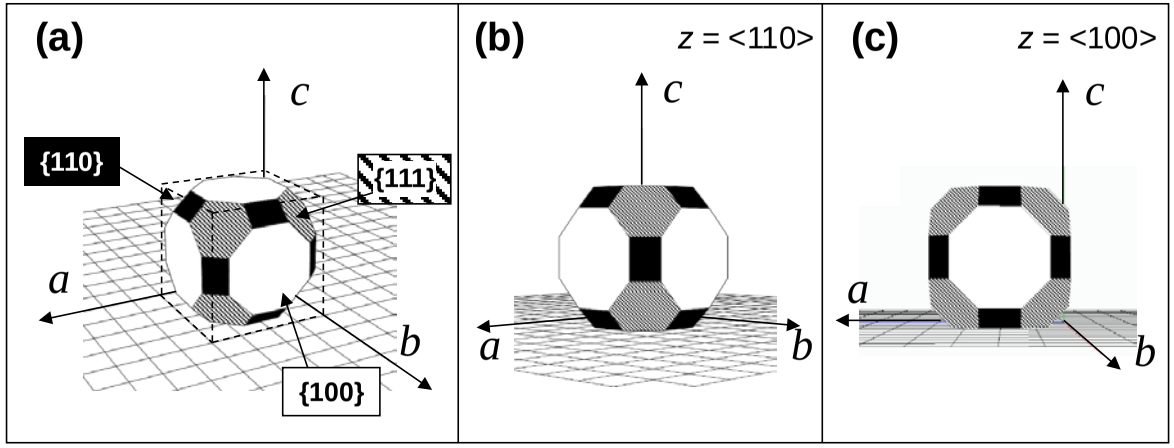

Fig. 4 A schematic of a model of an oxide particle (a) of overview, viewed along (b) z = <110> and (c) z = <100>.

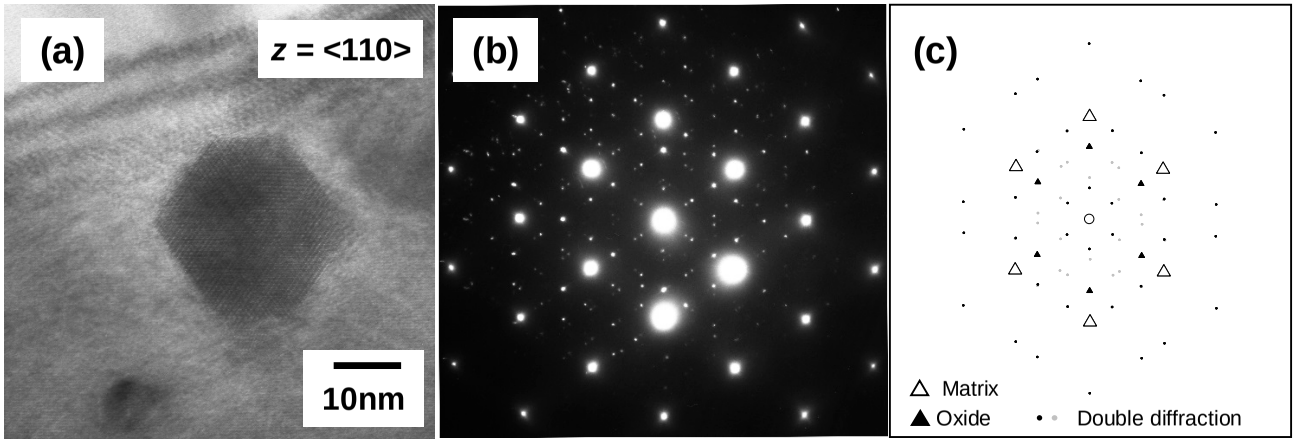

Fig. 5 (a) HRTEM image of an oxide particle along z = <110> and (b) corresponding SADP including double diffraction spots. (c) Detail schematic of the SADP (not fully described). White and Black triangles represent primary reflections from matrix and oxide, respectively. Black filled circles represent the double-diffraction spots occurring when the matrix-diffracted beam is rediffracted by the oxide. Gray filled circles represent the spots occurring when the above reflection is rediffracted, again, by the oxide.

1.4 Discussion

The confirmed orientation relationship of the embedded particle in the surrounding matrix indicates that the crystalline structure of the matrix would strongly affect nucleation and growth of the particle, especially when it is an embryo. This is because the orderly orientation relationship between the particle and the matrix still remains when the oxide particle is relatively large, as reflected in Fig. 3. Furthermore, this orderly orientation could imply a coherent particle/matrix interface. If the particle/matrix interface is coherent, an elastic strain field would be introduced. The presumed elastic strain field can be expected to have a significant role in pinning glide dislocations in the ODS steel and should have important strengthening effects. Besides, as for the displacement damage induced by irradiation, the elastic strain field can also affect the migration and segregation of point defects.

Fig. 6 is a TEM micrograph indicating the strain field that appeared around a faceted oxide particle for each **g** vector condition. The black and white contrast deriving from the strain field can be confirmed in the bright field and the weak beam dark field images in Fig. 6, respectively. Note that the existence of another oxide particle located just near the faceted oxide particle in Fig. 6 should be carefully taken into account when analyzing the contrast. A significant point to be emphasized in Fig. 6 is that the contrast of the strain field is extended along the **g** vector direction in each case. This implies that the strain field completely surrounds the faceted particle.

Generally, a spherical particle with a spherically symmetrical strain field, where the particle is coherent with a matrix, derives a double lobed contrast that extends in the direction of the **g** vector [15][16]. In the present study, the fully surrounding strain field, as stated previously, is similar to a double lobed contrast in that it depends on the **g** vector. However, it is not intuitively understood that the strain fields observed in Fig. 6 originate from a perfect coherent particle/matrix interface, because the lattice misfit between the oxide particle and the matrix, which is calculated experimentally to be 31.4 % for {200} and 27.9 % for {111}, is quite large to consider forming a perfectly coherent particle/matrix interface. On the other hand, since the strain field is observed it suggests

that the particle/matrix interface cannot be completely incoherent.

One possibility is that an introduction of misfit dislocations on the interface could potentially be expected to relax the misfit strain. The possible existence of misfit dislocations was pointed out by Ribis et al. [17] in a ferritic ODS material. Additionally, the anion deficits in a defect fluorite structure of the oxide particles could be attributed to the introduction of a localized atomic disarray or non-stoichiometric vacancies in the interface. That could also relax the misfit strain. Although the interface needs to be investigated further, the observed strain field in Fig. 6 can be considered to have a significant role for pinning glide dislocations or migration of point defects.

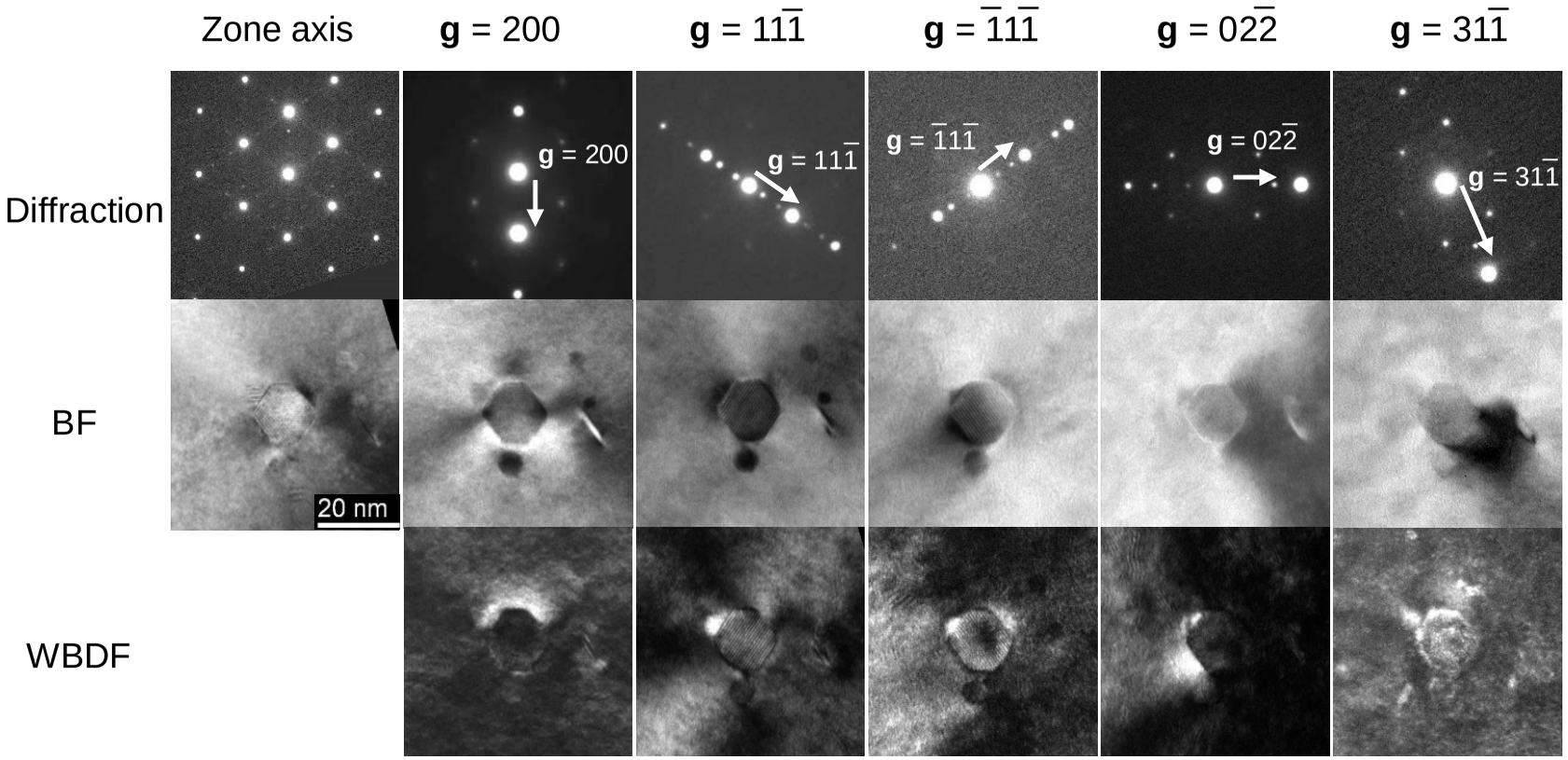

Fig. 6 TEM micrograph indicating the strain field appeared around a faceted oxide particle for each reflection condition.

1.5 Summary

The crystal structure and the orientation relationship of oxide particles with the matrix in ODS316 were investigated.

- Most of the oxide particles were complex oxides, the anion-deficient fluorite structure $Y_2Hf_2O_7$. The oxide particles basically had a faceted shape, and a model of the oxide particle that is a polyhedron surrounded with {100}, {110} and {111} planes was suggested. The faceted $Y_2Hf_2O_7$ particles presented a cube-on-cube orientation relationship to the surrounding FCC matrix without any rotation.

- The strain contrast analysis confirmed a strain field around a faceted oxide particle for given **g** vector conditions, suggesting that the strain field completely surrounds the faceted particle. The strain field may have some role for pinning glide dislocations during creep testing, and also have some role for migration of point defects induced by irradiation.

References

[1] S.S. Campos, H.-J. Kestenbach, E. V. Morales, Metall. Mater. Trans. A 32 (2001) 1245.

[2] J. Chen, P. Jung, W. Hoffelner, H. Ullmaier, Acta Mater. 56 (2008) 250.

[3] W. Kesternich, J. Nucl. Mater. 127 (1985) 153.

[4] K. Yutani, H. Kishimoto, R. Kasada, a. Kimura, J. Nucl. Mater. 367-370 (2007) 423.

[5] H. Oka, M. Watanabe, H. Kinoshita, T. Shibayama, N. Hashimoto, S. Ohnuki, S. Yamashita, S. Ohtsuka, J. Nucl. Mater. 417 (2011) 279.

[6] McIvried, McCarthy, JCPDS Card, No. 24-1406, Penn State University, 1972.

[7] M.A. Subramanian, G. Aravamudan, G.V. Subba Rao, Prog. Solid State Chem. 15 (1983) 55.

[8] C. Karthik, T.J. Anderson, D. Gout, R. Ubic, J. Solid State Chem. 194 (2012) 168.

[9] R.C. Ewing, J. Appl. Phys. 95 (2004) 5949.

[10] D.P. Reid, M.C. Stennett, N.C. Hyatt, J. Solid State Chem. 191 (2012) 2.

[11] K.R. Whittle, L.M.D. Cranswick, S.A.T. Redfern, I.P. Swainson, G.R. Lumpkin, J. Solid State Chem. 182 (2009) 442.

[12] J. Lian, X. Zu, K. Kutty, J. Chen, L. Wang, R. Ewing, Phys. Rev. B 66 (2002) 054108.

[13] H.W. Schmalle, T. Williams, A. Reller, A. Linden, J.G. Bednorz, Acta Crystallogr. Sect. B Struct. Sci. 49 (1993) 235.

[14] R.D. Shannon, Acta Crystallogr. Sect. A 32 (1976) 751.

[15] M.F. Ashby, L.M. Brown, Philos. Mag. 8 (1963) 1083.

[16] M.F. Ashby, L.M. Brown, Philos. Mag. 8 (1963) 1649.

[17] J. Ribis, Y. de Carlan, Acta Mater. 60 (2012) 238.

Appendix B

Least-square regression and error propagation

1. Least-square regression [1]

A straight line, $y = A + Bx$; Equal weights

If y is expected to lie on a straight line $y = A + Bx$, and if the measurements of y all have the same uncertainties, then the best estimates for the constants A and B are:

$$A = \frac{\sum x^2 \sum y - \sum x \sum xy}{\Delta}$$

and

$$B = \frac{N\sum xy - \sum x \sum y}{\Delta},$$

where the denominator, Δ, is

$$\Delta = N\sum x^2 - \left(\sum x\right)^2.$$

Based on the observed points, the best estimate for the uncertainty in the measurements of y is

$$\sigma_y = \sqrt{\frac{1}{N-2}\sum_{i=1}^{N}\left(y_i - A - Bx_i\right)^2}.$$

The uncertainties in A and B are:

$$\sigma_A = \sigma_y \sqrt{\frac{\sum x^2}{\Delta}}$$

and

$$\sigma_B = \sigma_y \sqrt{\frac{N}{\Delta}}.$$

Weighted fit for a straight line, $y = A + Bx$

If y is expected to lie on a straight line $y = A + Bx$, and if the measured values y_i have different, known uncertainties σ_i, then we introduce the weights $w_i = 1/\sigma_i^2$, and the best estimates for the constants A and B are:

$$A = \frac{\sum wx^2 \sum wy - \sum wx \sum wxy}{\Delta}$$

and

$$B = \frac{\sum w \sum wxy - \sum wx \sum wy}{\Delta},$$

where the denominator, Δ, is

$$\Delta = \sum w \sum wx^2 - \left(\sum wx\right)^2.$$

The uncertainties in A and B are:

$$\sigma_A = \sqrt{\frac{\sum wx^2}{\Delta}}$$

and

$$\sigma_B = \sqrt{\frac{\sum w}{\Delta}}.$$

2. Error propagation [1]

Uncertainty in Sums and Differences

Suppose that x, …, w are measured with uncertainties δx, …, δw, and the measured values are used to compute

$$q = x + \ldots + z - (u + \ldots + w).$$

If the uncertainties in x, …, w are known to be *independent and random*, then the uncertainty in q is the quadratic sum

$$\delta q = \sqrt{(\delta x)^2 + \cdots + (\delta z)^2 + (\delta u)^2 + \cdots + (\delta w)^2}$$

of the original uncertainties. In any case, δq is never larger than their ordinary sum,

$$\delta q \leq \delta x + \ldots + \delta z + \delta u + \ldots + \delta w.$$

Uncertainty in Products and Quotients

Suppose that x, …, w are measured with uncertainties δx, …, δw, and the measured values are used to compute

$$q = \frac{x \times \ldots \times z}{u \times \ldots \times w}.$$

If the uncertainties in x, …, w are *independent and random*, then the fractional uncertainty in q is the sum in quadrature of the original uncertainties,

$$\frac{\delta q}{|q|} = \sqrt{\left(\frac{\delta x}{x}\right)^2 + \cdots + \left(\frac{\delta z}{z}\right)^2 + \left(\frac{\delta u}{u}\right)^2 + \cdots + \left(\frac{\delta w}{w}\right)^2}.$$

In any case, it is never larger than their ordinary sum,

$$\frac{\delta q}{|q|} \le \frac{\delta x}{|x|} + \cdots + \frac{\delta z}{|z|} + \frac{\delta u}{|u|} + \cdots + \frac{\delta w}{|w|}.$$

Uncertainty in a Function of Several Variables

Suppose that x, …, z are measured with uncertainties δx, …, δz and the measured values are used to compute the function $q(x, \ldots, z)$. If the uncertainties in x, …, z are independent and random, then the uncertainty in q is

$$\delta q = \sqrt{\left(\frac{\partial q}{\partial x}\delta x\right)^2 + \cdots + \left(\frac{\partial q}{\partial z}\delta z\right)^2}.$$

In any case, it is never larger than the ordinary sum

$$\delta q \le \left|\frac{\partial q}{\partial x}\right|\delta x + \cdots + \left|\frac{\partial q}{\partial z}\right|\delta z.$$

References

[1] John R. Taylor, *An Introduction to Error Analysis*, 2nd Ed., University Science Books.

Research achievement

Research article related to this work

1) **H. Oka**, M. Watanabe, N. Hashimoto, S. Ohnuki, T. Shibayama, H. Kinoshita, S. Yamashita and S. Ohtsuka, In situ observation of damage structure in ODS austenitic steel during electron irradiation, Journal of Nuclear Materials, 417 (2011) 279–282.

2) **Hiroshi Oka**, Masashi Watanabe, Naoyuki Hashimoto, Somei Ohnuki, Shinichiro Yamashita, Satoshi Ohtsuka, Morphology of oxide particles in ODS austenitic stainless steel, Journal of Nuclear Materials, 442 (2013) 164–168.

3) **Hiroshi Oka**, Masashi Watanabe, Somei Ohnuki, Naoyuki Hashimoto, Shinichiro Yamashita, Satoshi Ohtsuka, Effect of minor alloying element on oxide dispersion in austenitic stainless steel, Journal of Nuclear Materials, 447 (2014) 248–253.

Other article

1) C.Z. Yu, **H. Oka**, N. Hashimoto and S. Ohnuki, Development of damage structure in 16Cr–4Al ODS steels duringelectron-irradiation, Journal of Nuclear Materials, 417 (2011) 286–288.

2) **H. Oka**, Y. Yamazaki, H. Kinoshita, N. Hashimoto, S. Ohnuki, S. Yamashita and S. Ohtsuka : Characterization of oxide particles in ODS austenitic stainless steel after heavy ion irradiation up to high doses, Mater. Res. Soc. Symp. Proc. Vol. 1298.

3) Naoyuki Hashimoto, **Hiroshi Oka**, Takeo Muroga, Takuya Nagasaka, Akihiko Kimura, Shigeharu Ukai, Takuya Yamamoto, Michail A. Sokolov,: Irradiation Effect on Tensile Property of F82H IEA and Its Joint in TITAN Project, Materials Transactions, Vol. 54 (2013) No. 4 p. 442-445.

4) **Hiroshi Oka**, Naoyuki Hashimoto, Takeo Muroga, Akihiko Kimura, Mikhail A Sokolov, Takuya Yamamoto, Somei Ohnuki, Hardness distribution and tensile properties in an electron beam weldment of F82H irradiated in HFIR, Journal of Nuclear Materials, Submitting.

International conference (Oral and poster)

1) H. Oka, M. Watanabe, N. Hashimoto, S. Ohnuki, T. Shibayama, H. Kinoshita, S. Yamashita and S. Ohtsuka : Electron irradiation properties of ODS austenitic stainless steel modified by third element addition, 14th International Conference on Fusion Reactor Materials, Sapporo, 2009/9/6-9/12

2) M. Watanabe, H. Oka, N. Hashimoto, S. Ohnuki, T. Shibayama, S. Yamashita and S. Ohtsuka : Fabrication and mechanical properties of nano-particle dispersed austenitic stainless steels, 14th International Conference on Fusion Reactor Materials, Sapporo, 2009/9/6-9/12

3) H. Oka : Electron Irradiation Properties of Oxide Dispersion Strengthened Austenitic Steel Modified by Third Element Addition, Asian CORE Winter School Technical Progaram, Sapporo, 2010/2/21-2/24

4) N. Hashimoto, H. Oka, H. Kinoshita and S. Ohnuki : Multiple-beam Irradiation Effects in Reduced Activation Ferritic Steels, 7th Pacific Rim International Conference on Advanced Materials and Processing, Cairns, 2010/8/1-8/5

5) C. Z. Yu, H. Oka, N. Hashimoto and S. Ohnuki : Stability of Y-Hf-O complex oxides in Fe-16Cr-4Al-0.6Hf ODS ferritic steel under electron-irradiation, Tenth Japan-China Symposium (JCS-10) on Materials for Advanced Energy Systems and Fission & Fusion Engineering, Kyoyo, 2010/10/19-10/22

6) H. Oka, Y. Yamazaki, H. Kinoshita, N. Hashimoto, S. Ohnuki, S. Yamashita and S. Ohtsuka : Characterization of oxide particles in ODS austenitic stainless steel after heavy ion irradiation up to high dose, 2010 MRS Fall Meeting, Boston, 2010/11/29-12/3

7) H.Oka, M.Watanabe, N.Hashimoto, S.Ohnuki, S.Yamashita, S.Ohtsuka, Interface structure of oxide particle and its influence for helium in an ODS austenitic stainless steel, 15th International Conference on Fusion Reactor Materials, Charleston, 2011/10/16-10/22

8) H.Oka, C. Liu, N.Hashimoto, S.Ohnuki, S.Yamashita, Relationship between microstructure and mechanical properties in austenitic stainless steel, 15th International Conference on Fusion Reactor Materials, Charleston, 2011/10/16-10/22

9) H.Oka, M.Watanabe, N.Hashimoto, S.Ohnuki, S.Yamashita, S.Ohtsuka, Interface structure of oxide particle in an ODS austenitic stainless steel, Asian-Core University Program on Advanced Energy Science, International Symposium on Advanced Energy Systems and Materials, Beijing, 2012/1/16-1/17

10) H. Oka, N. Hashimoto, S. Ohnuki, S. Yamashita、“Relationship between strength and microstructure of 316 steel at elevated temperature”、Asian-Core University Program on Advanced Energy Science, International Symposium on Advanced Energy Systems and Materials, Aomori, 2012/8/19-8/22

11) H. Oka, T. Kubota, N. Hashimoto, S. Ohnuki, S. Yamashita : Hardening and Softening Caused by Long Term Neutron Irradiation in Modified -SUS316 Stainless Steel, 2012 MRS Fall Meeting, Boston, 2012/11/25-11/30

12) Hiroshi Oka, Yutaka Sato, Naoyuki Hashimoto, Somei Ohnuki, : Evaluation of multi-layered hardness in ion-irradiated stainless steel by nano-indentation technique, 11th International Symposium on Fusion Nuclear Technology, Barcelona, 2013/9/16-20

13) H. Oka, N. Hashimoto, T. Muroga, A. Kimura, M.A. Sokolov and T. Yamamoto, Hardness distribution and tensile properties in an electron beam weldment of F82H irradiated in HFIR, 16th International Conference on Fusion Reactor Materials, Beijing, 2013/10/20-10/26

14) H. Oka, N. Hashimoto, S. Ohnuki, S. Yamashita, Strength factor of dislocations in neutron irradiated austenitic stainless steel at high temperature, 16th International Conference on Fusion Reactor Materials, Beijing, 2013/10/20-10/26

Domestic conference (Oral and poster)

1) 岡　弘, 渡部　雅, 橋本　直幸, 木下　博嗣, 柴山　環樹, 大貫　惣明 : オーステナイト系 ODS 鋼の電子線照射欠陥形成に及ぼすヘリウムの影響, 日本鉄鋼協会・日本金属学会両北海道支部合同サマーセッション, 室蘭, 2009/7/24

2) C. X. LIU, H. Oka, N. Hashimoto, S. Ohnuki, S. Yamashita, S. Ohtsuka, M. Ando and S. Jitsukawa : Evaluation of micro-hardness and microstructure of ion-irradiated ODS steels, 日本鉄鋼協会・日本金属学会両北海道支部合同冬季講演大会, 北海道大学, 2010/1/21-1/22

3) 岡　弘, 橋本　直幸, 木下　博嗣, 柴山　環樹, 大貫　惣明, 山下　真一郎, 大塚　智史, オーステナイト系 ODS 鋼の微細組織と機械的特性, 日本金属学会 2010 年春期(第 146 回)講演大会, 筑波大学, 2010/3/28-3/30

4) 岡　弘, 渡部　雅, 橋本　直幸, 柴山　環樹, 大貫　惣明, 山下　真一郎, 大塚　智史 : オーステナイト系 ODS 鋼の酸化物粒子の形成挙動, 日本金属学会 2010 年秋期 (第 147 回)講演大会, 北海道大学, 2010/9/25-9/27

5) Liu Chuanxin, H. Oka, N. Hashimoto, S. Ohnuki, N. Okubo, I. Ioka, M. Ando, K. Shiba and S. Jitsukawa : Radiation-hardening and Microstructural Change in Ferritic Steels ion-irradiated by TIARA Facility to Low Doses, 日本金属学会 2010 年秋期 (第 147 回)講演大会, 北海道大学, 2010/9/25-9/27

6) 山﨑　洋介, 岡　弘, Liu Chuanxin, 木下　博嗣, 橋本　直幸, 大貫　惣明, 鵜飼　重治, Fe+イオン照射したオーステナイト系 ODS 鋼の酸化物粒子の安定性, 日本金属学会 2010 年秋期 (第 147 回)講演大会, 北海道大学, 2010/9/25-

9/27

7) 岡　弘, 橋本　直幸, 木下　博嗣, 柴山　環樹, 大貫　惣明 : オーステナイト系 ODS 鋼の機械的特性および電子線照射下挙動, 日本鉄鋼協会・日本金属学会両北海道支部合同冬季講演大会, 室蘭工業大学, 2011/1/27-1/28

8) 岡 弘　C. X. Liu　橋本 直幸　大貫 惣明　N. Su　S. N. Jiang　山下 真一郎、”オーステナイトステンレス鋼における微細組織と機械的特性の相関”平成 23 年度日本金属学会日本鉄鋼協会両支部合同サマーセッション、室蘭工業大学、2011/7/22

9) 岡　弘, 劉　伝歆, 橋本　直幸, 大貫　惣明, N. Su, S. Jiang, 山下　真一郎, オーステナイトステンレス鋼における微細組織と機械的特性の相関, 東北大学金属材料研究所ワークショップ・「鉄鋼材料照射影響機構研究の最近の進展 ～ナノ組織から機械的特性へいかにつなげるか」, 仙台, 2011/9/29-9/30

10) 大貫　惣明, 岡　弘, 橋本　直幸, ナノ組織から照射硬化まで, 東北大学金属材料研究所ワークショップ・「鉄鋼材料照射影響機構研究の最近の進展 ～ナノ組織から機械的特性へいかにつなげるか」, 仙台, 2011/9/29-9/30

11) 山下 真一郎　窪田 知宜　岡 弘　橋本 直幸　大貫 惣明、”中性子照射した改良 SUS316 鋼における組織と機械強度のミクローマクロ相関”日本金属学会 2011 年秋期（第 149 回）講演大会, 沖縄, 2011/11/7-11/9

12) B. Zhou, C.X. Liu, H. Oka, N. Hashimoto, S. Ohnuki, Microstructure-hardness correlation in ion-irradiated iron, 日本金属学会 2011 年秋期（第 149 回）講演大会, 沖縄, 2011/11/7-11/9

13) 岡 弘　窪田 知宜　橋本 直幸　大貫 惣明　山下 真一郎、“中性子照射した改良 SUS316 鋼における組織と機械強度のミクローマクロ相関 (2)”日本金属学会 2012 年春期（第 150 回）講演大会, 横浜国立大学, 2012/3/28-3/30

14) 山下 真一郎　窪田 知宜　岡 弘　橋本 直幸　大貫 惣明、“中性子照射した改良 SUS316 鋼における組織と機械強度のミクローマクロ相関 (3)”日本金属学会 2012 年春期（第 150 回）講演大会, 横浜国立大学, 2012/3/28-3/30

15) 岡　弘, 橋本 直幸, 室賀 健夫, 長坂琢也, 木村晃彦, 鵜飼重治, M.A. Sokolov, T. Yamamoto、“F82H の接合・被覆部におけるはじき出し損傷と強度特性（日米協力 TITAN 計画）”、第 9 回核融合エネルギー連合講演会 -地球を救うエネルギー 核融合の未来-, 神戸, 2012/6/28-6/29

16) 岡 弘　窪田 知宜　橋本 直幸　大貫 惣明　山下 真一郎、“重照射した改良 SUS316 鋼における微細組織と機械強度の相関”、九州大学・応用力学研究所・炉内構造物の経年変化に関する研究集会, 九州大学, 2012/7/24-7/25

17) 岡 弘　窪田 知宜　橋本 直幸　大貫 惣明　山下 真一郎、“中性子照射した改良 SUS316 鋼における組織と機械強度のミクローマクロ相関 (4)”日本金属学会 2012 年秋期（第 151 回）講演大会, 愛媛大学, 2012/9/17-9/19

18) 佐藤 豊　岡 弘　大貫 惣明　橋本 直幸、“イオン照射したステンレス鋼のナノ硬さ評価法”、日本鉄鋼協会・日本金属学会両北海道支部合同冬季講演大会、室蘭工業大学、2013/1/24-1/25

19) 岡 弘　佐藤 豊、“FIB セクショニングによるナノ硬度分布の測定”、第 1 回北海道大学微小部・表面分析研究ユーザーズミーティング、北海道大学、2013/3/18

20) 岡 弘　佐藤 豊　橋本 直幸　大貫 惣明、“イオン照射したステンレス鋼のナノインデンテーション (セクショニング法の有用性)”、日本金属学会 2013 年秋期講演大会（第 153 回）, 金沢大学, 2013/9/17-9/19

Others

1) 劉　伝歆, 岡　弘, 橋本　直幸, 大貫　惣明, 大久保　成彰, 井岡　郁夫, 安堂　正己, 芝　清之, 実川　資朗 : Relation between Nano-Hardness and Microstructure in Fe-8Cr and F82H Irradiated by Dual Beam Ions, 日本金属学会 201 1 年春期 (第 148 回)講演大会概要集, pp.232（2011）

2) 岡　弘, 劉　伝歆, 橋本　直幸, 大貫　惣明, Su Na, 山下　真一郎 : オーステナイトステンレス鋼における微細組織と機械的特性の相関, 日本金属学会 201 1 年春期 (第 148 回)講演大会概要集, pp.232（2011）

Acknowledgments

本論文を書くにあたり、以下の方々にお世話になりました。ここに心より感謝の意を表します。

主査である大貫 惣明 教授には、本研究の全般にわたり終始懇切丁寧な御指導と貴重な御教示を賜りました。また、多くの国際学会、国内学会での発表など、研究者として多くの貴重な経験をする機会を与えて頂きました。大変お忙しい中であるにも関わらず、なんとか時間を見つけてはご指導下さいました。心より深く感謝申し上げます。

北海道大学大学院 工学研究院 鵜飼 重治 教授、三浦 誠司 教授、橋本 直幸 准教授には、本論文の審査を通して貴重な御助言を頂きました。心より感謝申し上げます。

北海道大学大学院 工学研究院 橋本 直幸 准教授ならびに礒部 繁人 助教には、日頃より私の研究に対して言い尽くせないほどの多大なる御助言・御指導を頂きました。ここに、心より深く、深く感謝申し上げます。

日本原子力開発機構 山下 真一郎 博士には、実験・解析に関し、様々な御指導・御助言を頂きました。研究活動全般の直接的な御指導をして頂いただけでなく、研究活動に対しての良き姿勢を学ばせて頂きました。心より感謝申し上げます。

日本学術振興会には、平成 24 年度同会特別研究員に採用して頂きました。同研究員の採用により、一層研究に邁進することができました。心より感謝申し上げます。

北海道大学大学院 工学研究院 坂口 紀史 准教授には、電子顕微鏡を用いた実験に多大なる御協力・ご指導を頂きました。心より感謝申し上げます。

北海道大学大学院 工学研究院 大野 直子 助教には、研究に関しご助言を頂きました。心より感謝申し上げます。

京都大学 エネルギー理工学研究所 笠田 竜太 准教授には、ナノインデンテーションの研究に関し、様々な御指導・御助言を頂きました。心より感謝申し上げます。

日本原子力開発機構 関根 学 氏には照射後材料の TEM 観察に関し多大なご協力を賜りました。心より感謝申し上げます。

現 JFE の窪田 知宜 君には照射後材料の TEM 観察に関し多大なご協力を賜りました。ここに感謝申し上げるとともに、貴君の今後の御発展を心より御祈り申し上げます。

現札幌市消防局の佐藤 豊 君にはナノインデンテーション法による研究の一切について取り組んで頂きました。貴君の多大なるご協力に謝意を表し、今後の御発展を心より御祈り申し上げる次第です。

機能材料学研究室の学生および卒業生諸氏には、研究室生活において、言い尽くせないほどの様々な思い出、影響を与えて頂きました。心より感謝し、各位のより一層の御発展を心より御祈り申し上げます。

最後に、どんな時も私の判断に理解を示し支えてくれた亡き父、そして母と姉に感謝申し上げます。

2014 年 2 月　　岡　　弘